Controlling structural and magnetic properties of epitaxial NiMnSb for application in spin torque devices

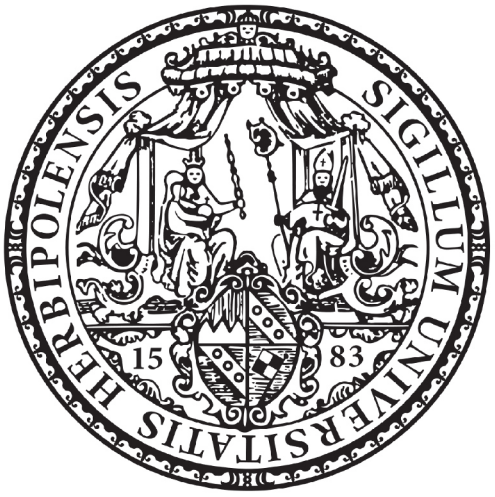

Dissertation zur Erlangung des naturwissenschaftlichen Doktorgrades der Julius-Maximilians-Universität Würzburg

vorgelegt von
Felicitas Irene Veronika Gerhard
aus Stuttgart

Würzburg 2014

Eingereicht am: ...

bei der Fakultät für Physik und Astronomie

1. Gutachter: PD. Dr. C. Gould

2. Gutachter: Prof. Dr. V. Dyakonov

3. Gutachter: ...

der Dissertation.

Vorsitzender ...

1. Prüfer: PD. Dr. C. Gould

2. Prüfer: Prof. Dr. V. Dyakonov

3. Prüfer: Prof. Dr. B. Trauzettel

im Promotionskolloquium.

Tag des Promotionskolloquiums: 26.03.2015

Doktorurkunde ausgehändigt am: ...

Contents

Zusammenfassung

Diese Arbeit beschäftigt sich mit dem epitaxialen Wachstum von NiMnSb und seinen strukturellen und magnetischen Eigenschaften. NiMnSb gehört zu der Gruppe der sogenannten Halb-Heusler Legierungen. Diese sind wiederum eine Untergruppe der Heusler Legierungen, die sich durch eine bestimmte Kristallstruktur auszeichnen. NiMnSb ist ein Ferromagnet und zudem ein Halbmetall, was sich durch eine 100%ige Spinpolarisierung im Volumenmaterial auszeichnet. Wegen seiner ausserdem schwachen magnetischen Dämpfung sowie einer hohen Curie-Temperatur ist NiMnSb ein vielversprechendes Material für die Anwendung in der Spintronik, insbesondere in Spin-Drehmoment Bauteilen. Kapitel 1 gibt einen Einblick in NiMnSb und seine speziellen Eigenschaften sowie eine Übersicht über die Veröffentlichungen über dieses Material.
Kapitel 2 beschäftigt sich mit dem epitaxialen Wachstum von Heterostrukturen, basierend auf einzelnen NiMnSb Schichten. Beim Wachstum von NiMnSb mittels Molekular Strahl Epitaxy (molecular beam epitaxy, MBE) sind die exakten Flussverhältnisse und die Stabilität der Flüsse essentiell. Durch in-situ RHEED Beobachtungen kann schon beim Wachstum kontrolliert werden, ob die verwendeten Flüsse vom optimalen Wert abweichen. Verschiedene RHEED Rekonstruktionsmuster, die bei jeweils zu hohem oder zu niedrigem Fluss eines der drei Materialien Ni, Mn, Sb auftauchen, werden beobachtet und beschrieben. Diese dienen einerseits zur Findung der optimalen Parameter für stöchiometrisches Wachstum, auf der anderen Seite hängen sie mit den magnetischen Eigenschaften zusammen.
Die strukturelle Charakterisierung erfolgt durch Hochauflösende Röntgen Diffraktometrie (HRXRD). Hierbei wird die Kristallqualität sowie die Gitterkonstante der NiMnSb Schicht bestimmt. Die Kristallqualität ist extrem hoch, übliche ω-Breiten liegen im Bereich unter 20 Bogensekunden. Es wird festgestellt, dass die Gitterkonstante von NiMnSb von seiner Zusammensetzung (varriert durch erhöhte oder abgeschwächte Flüsse beim Wachstum) abhängt. Die vertikale Gitterkonstante wird später als Maß für die Mn-Konzentration benutzt. Neben der strukturellen Charakterisierung wird die Sättigungsmagnetisierung mittels SQUID Messungen bestimmt, die ebenfalls von der genauen Zusammensetzung abhängig ist. In Proben mit einer von stöchiometrischen Verhältnissen stark abweichenden Zusammensetzung weicht der Wert der Sättigungsmagnetisierung vom theoretisch erwarteten Wert $4.0\mu_B$ ab. Diese strukturelle und magnetische Charakterisierung, zusammen mit einer Beschreibung von möglichen Defekten und deren Auswirkung auf das Material sind Inhalt von Kapitel 3.

Das folgende Kapitel 4 präsentiert eine detaillierte Studie der magnetischen Anisotropie von NiMnSb, welche mittels ferromagnetischer Resonanz (FMR) gemessen wird. Diese magnetische Anisotropie ist eine der wichtigsten Eigenschaften eines Ferromagneten, sowohl in Hinsicht auf Anwendung als auch in Hinsicht auf das grundlegende Verständnis des Materials. Bisher wurde angenommen, dass die Anisotropie in NiMnSb von der Dicke abhängt, wobei die uniaxiale Anisotropie in dünnen (10 nm) Schichten 90° gedreht ist im Vergleich zu dicken (40 nm) Schichten. Es wird festgestellt, dass die Anisotropie auch stark von der Zusammensetzung der Schichten abhängt - das alte Bild der Anisotropie wird erweitert von einer einfachen Dickenabhängigkeit zu einer Abhängigkeit von Zusammensetzung und je nach Zusammensetzung (d.h. Mn Konzentration) auch von Dicke. Untersuchungen an Schichten unterschiedlicher Dicke lassen vermuten, dass die Rotation der uniaxialen Anisotropie von der [110] zur $[1\bar{1}0]$ Kristallrichtung durch eine Erhöhung der Mn Konzentration oder durch Relaxation im Kristall in sehr dicken Schichten (80 nm) herbeigeführt wird. Durch diese neue Erkenntnis können nun NiMnSb Schichten mit gegebener Dicke und gegebener magnetischer Anisotropie gewachsen werden. Für das Design von Bauteilen wie z.B. Spin Drehmoment Oszillatoren ist dies sehr hilfreich.
Im letzten Kapitel 5 wird das Wachstum und die Charakterisierung von NiMnSb-ZnTe-NiMnSb Heterostrukturen beschrieben. Die ZnTe Schicht dient hier als Barrier und ist mit einer Bandlücke von 2.2 eV isolierend im Vergleich zum metallischen NiMnSb. Bei diesem Prozess ist vorallem das Wachstum einer dünnen Schicht ZnTe auf NiMnSb eine Herausforderung, wobei das ZnTe die NiMnSb Schicht nicht beeintrchtigen darf und zudem eine zweite NiMnSb Schicht auf das ZnTe gewachsen werden muss. Hier werden Parameter wie Schichtdicken und Anisotropien (Mn Konzentration) variiert und die resultierenden Heterostrukturen mittels HRXRD und SQUID charakterisiert. Individuelles Schalten der Magnetisierungen in den beiden NiMnSb Schichten wird durch verschiedene Mn Konzentration erreicht. Diese Strukturen sind eine vielversprechende Grundlage für Spin Drehmoment Oszillatoren, die auf dem TMR (Tunnel Magnetowiderstand) Effekt basieren. Für solche Spin Drehmoment Oszillatoren wird ein Spin-Ventil mit je einer festen und einer freien Magnetisierung benötigt - dies kann durch zwei zueinander senkrechten Anisotropien realisiert werden, wobei entlang einer Kristallrichtung eine Schicht eine weiche Achse, die andere Schicht eine harte Achse aufweist.

Summary

This thesis is about the epitaxial growth of NiMnSb and its structural and magnetic properties. NiMnSb is part of the so-called Half-Heusler alloy family, being a subgroup of the Heusler alloys that are characterized by a certain crystal structure. NiMnSb is a ferromagnet and, in addition, a half metal, meaning it exhibits a spin polarization of 100% in bulk. Other properties like a very small Gilbert-damping and a high Curie temperature make NiMnSb an attractive material for application in spintronics, especially for spin torque devices. In chapter 1, NiMnSb and its properties are introduced along with an overview on other reports on this material.
The epitaxial growth of heterostructures based on single layers of NiMnSb is presented in chapter 2. For the epitaxial growth of NiMnSb, the flux ratios, especially their stability, are essential since the growth is stoichiometric. In-situ RHEED observations allow to control and observe the correct flux ratio already during growth. Various RHEED reconstructions are observed, depending on the enhanced or suppressed flux of one of the three elements Ni, Mn and Sb. These RHEED reconstructions are on the one hand helpful to optimize growth and find stoichiomteric conditions, on the other hand they are correlated with the magnetic properties of NiMnSb, especially the anisotropy.
Using High Resolution X-Ray Diffraction (HRXRD), the structural properties of the samples are characterized, where both crystal quality and the lattice parameter are determined. The crystal quality is extremely high, where ω-scans with FWHM in the range below 20 arcsec are observed. Additionally, it is found that the composition of the material effects the lattice constant of NiMnSb and can thus be used as a measure for the Mn concentration. A second hint on the composition of the samples comes from SQUID measurements that are done to determine the saturation magnetization. For far off-stoichiometric samples, the saturation magnetization differs from the theoretical expected value of 4.0 μ_B. These structural and magnetic characterization measurements are shown in chapter 3, together with an evaluation of possible off-stoichiometric defects and their effect on the material.
A more detailed magnetic investigation will be the content of chapter 4: Ferromagnetic resonance (FMR) is used to determine the magnetic anisotropy of such NiMnSb layers. The magnetic anisotropy is one of the most important properties of a magnetic material in terms of application and fundamental properties. The state of the art so far was, that the anisotropy of NiMnSb is thickness-dependent, where the uniaxial anisotropy component rotates by 90° when going from thin (10 nm) to thicker (40 nm) layers. It is found that

the composition of the layer strongly effects the magnetic anisotropy as well - thus, the former picture is extended and it is seen that the thickness can influence the anisotropy, however depending on the Mn concentration. Investigations on layers of different thickness suggest that the rotation of the uniaxial anisotropy easy axis from the [110] to the [1$\bar{1}$0] direction is caused by either additional Mn or by relaxation in very thick (80 nm) layers. Using this knowledge, NiMnSb layers with given thickness and given magnetic anisotropy can be grown. This is extremely useful for the design of e.g. spin torque oscillators.
In the last chapter, the growth and characterization of NiMnSb-ZnTe-NiMnSb heterostructures is presented. Here, ZnTe serves as a barrier layer with an energy gap of (2.2 eV) and thus being insulating in comparison with NiMnSb which is a metal. For this process, the main challenge is to grow a thin ZnTe layer on top of a NiMnSb layer without effecting it, and allowing to grow a second NiMnSb on top of the ZnTe. Parameters like layer thicknesses and anisotropy (Mn concentration) are varied and the resulting layer stacks are characterized by HRXRD and SQUID hysteresis curves. By using different Mn concentration for the bottom and top NiMnSb layer, individual magnetic switching of the two NiMnSb layers can be achieved. Such samples are a very promising basis for spin torque oscillators, based on the TMR (tunneling magnetoresistance) effect. For such an STO, a spin valve with one fixed and one free magnetic layer is required - this can be realized by two layers with mutually orthogonal anisotropy (one layer having an easy, the other having a hard axis).

Chapter 1

The Half-Heusler alloy NiMnSb and its role in spintronics

Heusler and Half-Heusler alloys are a class of materials, first characterized by F. Heusler in 1903 who discovered ferromagnetic properties of an alloy - Cu_2MnAl - composed by non-ferromagnetic elements [1]. Later, it was found that Cu_2MnAl is only part of a larger group of alloys, all crystallizing in the same lattice structure, the $L2_1$ lattice. All alloys forming this lattice structure were from now on called Heusler-alloys, even when one or more elements of the ferromagnetic alloy are already ferromagnetic by themselves. Fig. 1.1 left shows a schematic of the $L2_1$ lattice structure: It consists of four fcc-lattices stacked together on the space diagonal and is occupied by the elements X1 $(\frac{1}{4}, \frac{1}{4}, \frac{1}{4})$, X2 $(\frac{3}{4}, \frac{3}{4}, \frac{3}{4})$, Y (0,0,0) and Z $(\frac{1}{2}, \frac{1}{2}, \frac{1}{2})$. In the case of (Full) Heusler alloys, the lattice site X1 is occupied by the same element as lattice site X2 $(\frac{3}{4}, \frac{3}{4}, \frac{3}{4})$. This lattice site can also be unoccupied, meaning the lattice exhibits a vacancy position and is then called a C1b structure. Heusler alloys with a vacancy position on this lattice site are called Half-Heusler alloys. The here presented material NiMnSb is such a Half-Heusler alloy with X2 = Ni, Y = Mn and Z = Sb, as shown in Fig. 1.1 right. The corresponding Full-Heusler would be Ni_2MnSb.
This unique lattice structure is also cause for the special bandstructre in NiMnSb [2], see Fig. 1.2: Due to the breaking of the conjugation symmetry of the Mn atom, the bandstructure for spin-up and spin-down electrons evolves differently: for the spin-up electrons (here majority spin direction), the bandstructure is metal-like with energy levels crossing the Fermi energy (Fig. 1.2 a). For the spin-down electrons (here minority spin direction), the energy levels are shifted such that the Fermi energy now lies in a bandgap and thus the

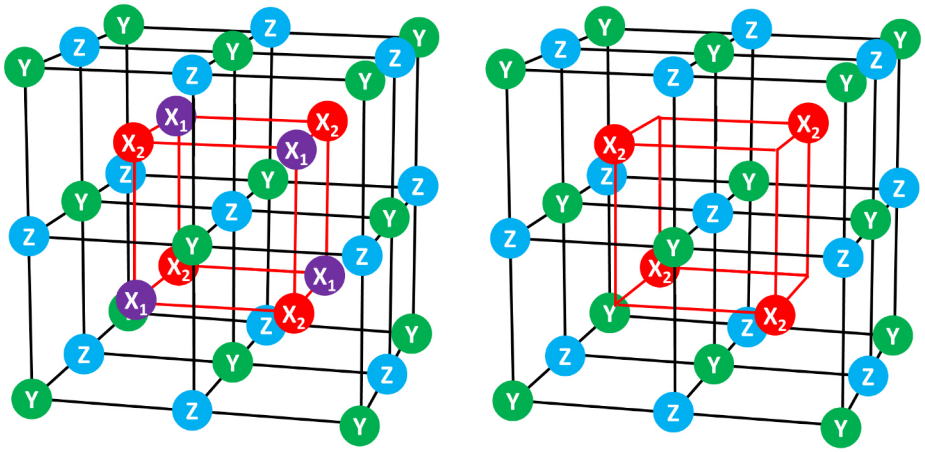

Figure 1.1: Left: $L2_1$ lattice structure of Heusler alloys. Four fcc-sublattices are occupied by three different elements X1/X2, Y and Z. Right: Half-Heusler alloy NiMnSb, where lattice site X1 is unoccupied and X2 = Ni, Y = Mn and Z = Sb.

bandstructure is semiconductor-like (Fig. 1.2 b). Theoretically, this results in a 100% spin polarization in bulk, making NiMnSb a perfect candidate for of spin injection application. In bulk, total spin polarization has been measured ([3], [4]), however at the surface, a reduction of the spin polarization was found. Spin polarizations of 40 - 60 % at the surface of NiMnSb are reported [5], [6], [7] making it a high spin polarized material compared to other materials used in spintronices such as Iron and Cobalt (40 - 45 % [8]) and Permalloy (40 - 60 % [9]). The reason for the decreased spin polarization at the surface is the breaking of the lattice symmetry and subsequently different binding conditions of the atoms, compared to bulk. Bandstructure calculations of such surfaces reveal a crossing of the minority spin band with the Fermi level and thus both majority and minority electrons contribute to the transport [10].

Despite this drawback, NiMnSb has been and still is of high interest. Both theoretical and experimental studies are reported, where most experimental studies are performed on NiMnSb, deposited by various sputtering techniques, see e.g. references [11], [12]. There are very few reports on MBE grown NiMnSb other than from the group here in Würzburg (see references [13] and [14], published in 2002, or [15], 2005), and no more recent publication. Nonetheless, many reports on structural, magnetic and electronic investigations can be found, as well as surface analysis (a very small selection would be e.g. references [16], [17], [18], [19]). Especially the spin polarization is of high interest, regarding NiMnSb as a

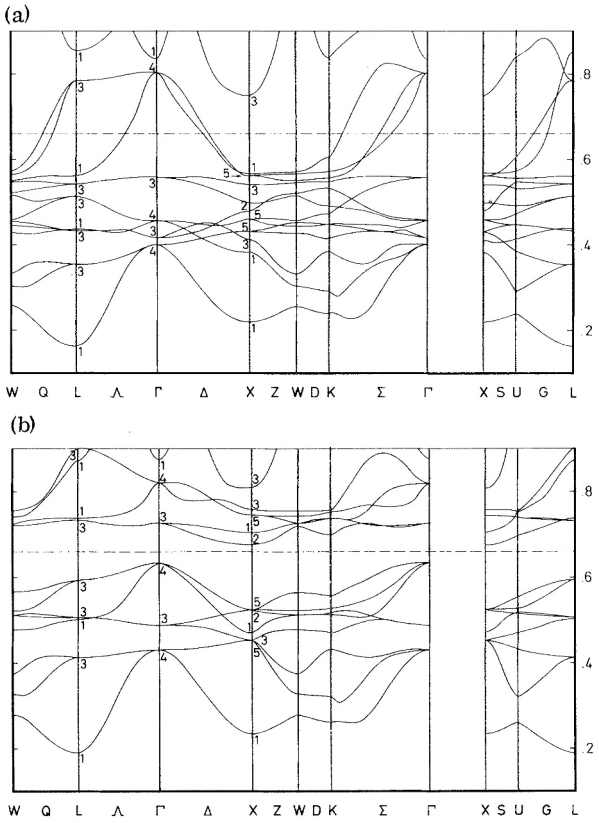

Figure 1.2: Bandstructure of NiMnSb for the majority spin direction (a, metal-like) and the minority spin direction (b, semiconductor-like) [2].

potential material for application in spin torque devices.
Novel spin torque devices such as spin torque oscillators (STOs) have been built and studied in a wide variety of configurations and materials and still draw more and more attention. Output power, linewidth and tunability of the frequency, and threshold current are three main properties that define the quality and functionality of an STO. Thus, e.g., the magnetic damping is an important parameter of potential device materials since it counteracts on the spin torque and determines the threshold current at which oscillations can occur. Additionally, it has been found that the mutual orientation of the magnetization of the two involved ferromagnetic layers plays an important role, where higher output powers and better linewidths could be achieved ([20], [21], [22]). While both linewidths and also tunability of the emitted microwave signals have been improved and optimized during the years, the output power remains below usability. It is directly related to the MR ratio

of the spin valve the STO is based on (the MR ratio corresponds to change in resistance between antiparallel and parallel state of a spin-valve). This lead to a modification of the spin valves from standard conducting spin valves to magnetic tunneling junctions (MTJs). Today, the highest output power recorded is 0.28 µW [23], emitted by a CoFeB-MgO spin valve based STO.

Regarding this, NiMnSb is an attractive candidate for application in spin torque devices. One very important property is its very low Gilbert damping factor [24], that lets expect low threshold currents. Besides that, the magnetic anisotropy - describing the energetically favored direction of the magnetization caused by either intrinsic (crystalline anisotropy) or extrinsic (caused by shaped or strain) properties - exhibits a unique character in NiMnSb. During this thesis, it has been found that the magnetic anisotropy - both orientation and strength - in this material can be controlled by small variation of the composition, as will be discussed in detail in chapter 4. This control of magnetic property allows to design devices such that the configuration of the two magnetizations of the two layers is optimal for the desired application. For example, spin valves with two NiMnSb layers with mutually orthogonal anisotropy, separated by a thin spacer layer have been designed and grown fully epitaxial, as will be described in chapter 5, together with their structural and magnetic characterization.

Chapter 2

Growth of NiMnSb by MBE

Molecular Beam Epitaxy (MBE) is a method to deposit ultra high quality, pseudomorphic materials. In the first section, the concepts of MBE including the in-situ method RHEED are introduced. In the subsequent sections, 2.3 and 2.4, the MBE processes for the buffer layer (In,Ga)As on InP and for NiMnSb on (In,Ga)As are presented. The samples investigated in this thesis are grown in (001) crystal direction on InP substrates.

2.1 MBE - general principle and setup

Ultra high crystal quality materials can be deposited by Molecular Beam Epitaxy, where ultra high vacuum conditions (UHV, pressures in the range smaller than 1×10^{-9} mbar) are required. Several MBE chambers with different materials connected to a cluster are available, among them a III-V chamber containing group III and group V elements like Ga, In, As, used to grow the (In,Ga)As buffer layer for the here presented samples. A second chamber contains Ni, Mn and Sb for the growth of the NiMnSb layer. A third chamber contains group II and group VI materials, used for the growth of NiMnSb-ZnTe-NiMnSb heterostructres described in chapter 5. Furthermore, a sputtering chamber is connected to the UHV cluster, allowing for the in-situ deposition of various metals as a cap layer (such capping layers are needed to avoid oxidation and relaxation of the NiMnSb layers [25]).
In an MBE chamber, the elements are evaporated in so-called effusion cells, where different materials can require different types of cells. Variations are made in the design of the heating filaments and in shapes and materials of the crucible. In case of Indium and Gallium, effusion cells with two heating filaments are used to achieve a temperature gradient between

the base and tip of the cell. These parameters can change the growth and resulting crystal quality significantly as described in section 2.3. For Arsenic, a valved cell is used, where the material is kept at constant temperature at all times and a valve controls the emitted flux. Another special high temperature cell is used for Nickel, allowing temperatures of well above 1000 °C (growth temperature for Nickel used here is in the range of 1390 °C). The material of the crucible is usually PBN, where special elements can require special crucible materials to avoid alloying of the element with the crucible and resulting damage.
The substrate holder contains a heating device to adjust the growth temperature and is rotatable to achieve homogeneous growth. Other components are flux gauges to measure the beam equivalent pressure (BEP) of the evaporated materials, and a reflective high energy electron diffraction setup (RHEED), described in more detail in the next section.

2.1.1 In-situ observation: RHEED

RHEED - reflective high energy electron diffraction - is used to monitor in-situ the surface of the sample, where information like surface roughness and surface reconstruction can be gained. The theoretical background is described shortly in the following paragraph, a detailed description can be found e.g. in reference [26].
In reciprocal space, the incident wavevector $\vec{k_i}$ spans the Ewald's sphere (with radius $\vec{k_i}$) that allows to construct the diffraction condition in reciprocal space (Fig. 2.1 shows a schematics of this Ewald's sphere construction): The difference between the incident wavevector $\vec{k_i}$ and the diffracted wavevector $\vec{k_d}$ equals the scattering vector $\Delta\vec{k}$. The diffraction condition is fulfilled for all points on the Ewald's sphere where this scattering vector equals a reciprocal lattice vector $\vec{G} : \vec{k_i} - \vec{k_d} = \vec{G}$. This is valid for 3D structures (transforming into 0D points in reciprocal space) - for 2D structures like the surface of a wafer, the corresponding structures in reciprocal space are so-called 1D truncation rods. Now, the diffraction condition is fulfilled for each point where the Ewald's sphere and the truncation rods intersect.
In the MBE chamber, a high-energy electron beam incidences the sample surface at a very small angle, is diffracted and then hits a luminescent screen where the diffraction pattern (in the following also called reconstruction) is observed - see Fig. 2.2. The RHEED reconstruction pattern gives several information on the properties of the sample surface: A streaky pattern as can be seen in Fig. 2.2 usually is a sign for a 2D growth and a smooth surface. In case of 3D elements on the surface, dots occur in the RHEED picture that are

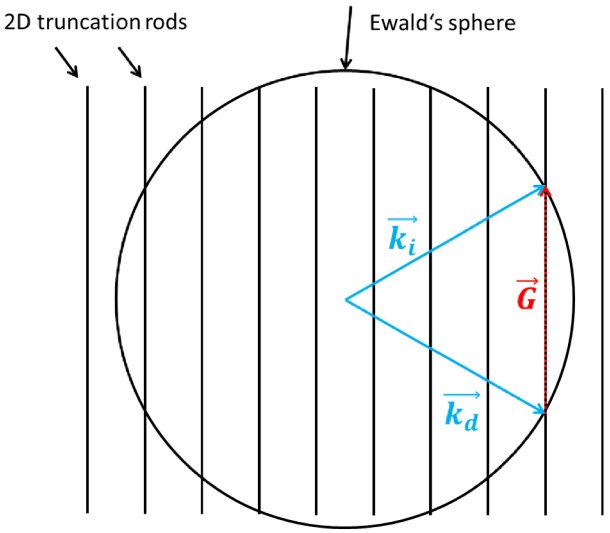

Figure 2.1: Ewald's sphere to construct diffraction condition for RHEED: The 2D surface of the sample transforms into a 1D truncation rod in reciprocal space. The diffraction condition is fulfilled for each point on the Ewald's sphere where one truncation rod intersects.

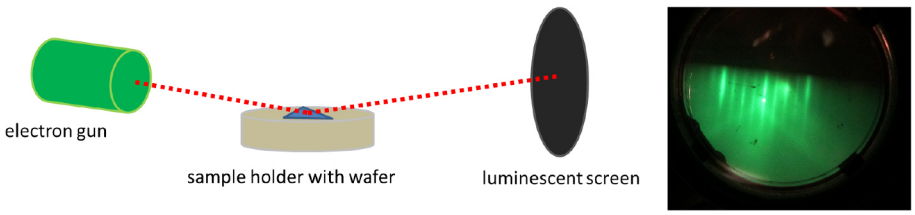

Figure 2.2: Left: schematics of RHEED setup, right: exemplary RHEED picture.

stationary under rotation of the wafer. However, in case of large 3D objects at the surface, the RHEED can still be streaky due to smooth parts of the surface next to the large 3D objects that cannot be seen in the diffraction pattern. The so-called specular spot (the bright spot in the middle of the RHEED screen in Fig 2.2) is a further indication for the crystal quality. This spot is the directly mirrored electron beam on the sample surface. A high intensity and sharp spot suggests a clean and smooth surface.
In NiMnSb, the crystal structure and thus also the RHEED pattern is highly sensitive to the composition of the layer and can be used to determine the ideal growth parameters. In section 2.4, the individual RHEED patterns associated with stoichiometric and off-stoichiometric growth are presented.
Since different notations are used to describe RHEED patterns, the notation used in this thesis is as follows: The RHEED reconstruction pattern is recorded and described for the two main crystal axes [110] and [1$\bar{1}$0] which are 90° to each other. The pattern for one direction is notated as "d/x" where x is the number by which the distance between the 00 reflex and the 01 reflection is divided. Fig. 2.3 shows the examples of d/1, d/2, d/3.

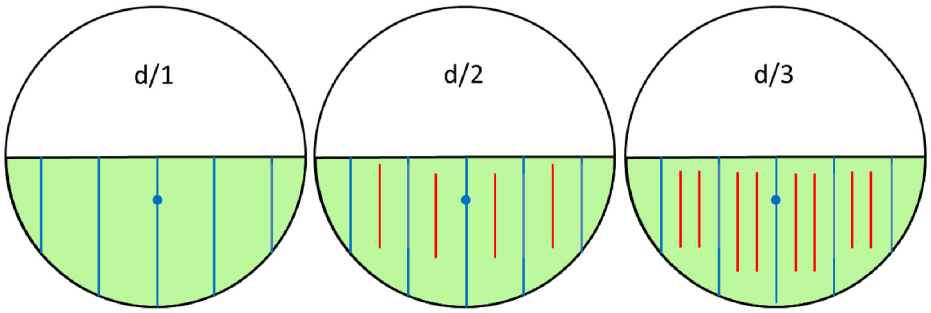

Figure 2.3: Notation of RHEED patterns used in this thesis.

2.2 Substrate

The substrate used for all samples is InP in (001) crystal orientation, coming with an oxide on top. The wafers are either doped with S or Fe and are chosen depending on application. In case of Fe, the dopants compensate remaining charge carriers of undoped InP - the resulting substrate InP:Fe has high resistivity and is used as insulating substrate. Such high resistivity substrates are useful for any kind of transport experiments since parallel conductance through the substrate can be suppressed/avoided - however, the crystal quality

of InP:Fe is worse compared to S-doped InP:S, which is conducting and has low resistivity. The wafers are glued onto sample holders made of Molybdenum (Molyblocks) with Indium-glue, inserted into the UHV system and then degassed at 250 °C for 10 minutes, mainly to remove water on the surface. After this degassing process, the sample is transferred into the GaAs chamber for the growth of the (In,Ga)As buffer layer, described in the next section. This buffer is serving as a Phosphor desorption prevention of the substrate and is grown lattice-matched to the InP.

2.3 Growth of (In,Ga)As on InP

In order to be able to grow the (In,Ga)As buffer, the oxide on the InP substrate has to be removed, requiring temperatures above 500 °C. However, above these temperatures, Phorphor from the substrate would be desorbing, which can be avoided by applying an As supporting pressure of about 1×10^{-5} mbar at all times where the substrate temperature exceeds 300 °C. The following process is also described in [27] and [28]. While heating up the substrate, in the range of 500-550 °C a clear d/2 RHEED reconstruction can be seen. While increasing the temperature, the desorption of the oxide is indicated by a change from the d/2 to a d/4 reconstruction. Then, the substrate is heated about 10 K above this desorption temperature, until the d/4 reconstruction is clear with high intensity streaks, to ensure a complete desorption of the oxide. The sample is then cooled down immediately to growth temperature, which is chosen depending on the desorption temperature and lies about 10-15 K below it. This is a very critical step in the process: RHEED observations show that the surface roughens significantly if the time between desorption and growth start is too long. After the growth temperature is reached, growth is initiated by opening the In and Ga shutter simultaneously. After a few seconds, the d/4 reconstruction is transforming back into a d/2 reconstruction and the RHEED pattern gets spotty until after about 2 min, a streaky pattern with a weak d/2 reconstruction is observed.
(In,Ga)As can be grown lattice matched to the InP substrate (lattice constant 5.869 Å) by finding the correct combination of InAs and GaAs with corresponding lattice constants of 6.06 Å and 5.65 Å, respectively. Thus, theoretically, the absolute ratio is 0.53 / 0.47, corresponding to a flux ratio of In/Ga of about 1.3. By determining the lattice constant (by HRXRD measurements, see next chapter), the correct ratio of In/Ga can be found - for lattice matching, the (In,Ga)As layer signal will overlap with the InP signal. While cooling down after the growth, the RHEED reconstruction transforms into a d/3 along $[1\bar{1}0]$ and

d/4 along [110] pattern at substrate temperatures below 450 °C.
The main difficulty of the growth of (In,Ga)As layers is to avoid defects, that can be compared to "oval defects", which occur in III-V materials and can be classified into different types [29] (for GaAs). Here, similar but also different kinds of defects are found in the (In,Ga)As buffer layers - Fig. 2.4 is a collection of all different kinds of defects found. In general, there are two groups - small ($< 10\,\mu m$ length) and large ($> 10\,\mu m$ length) defects, that are all oval shaped, where the small ones are oriented along the $[1\bar{1}0]$ crystal direction, the large ones are oriented along the [110] crystal direction.

- 1a: Small, oval shaped hillocks, no core, oriented along $[1\bar{1}0]$, length 1-2 µm. This kind of defect is found on all samples and can cover the entire background, resulting in a continuous surface roughness.

- 1b: Small oval shaped hillock with a small core, oriented along $[1\bar{1}0]$, length 3-5 µm. Occurs ocassionally, probably caused by dirt or spits.

- 1c-e: Small oval shaped hillock, double, with core, oriented along $[1\bar{1}0]$, length 3-10 µm. Can exhibit round or pointed ends.

- 1f: Accumulation of several small oval defects, usually around a core. Oriented along $[1\bar{1}0]$.

- 2a: Large oval shaped defect, aligned along [110] crystal direction, with asymmetric core (that consists probably of an accumulation of small oval defects). Flat surface, mostly clear edges. Pointed ends.

- 2b: Large oval shaped defect, aligned along [110], with asymmetric core. Surface rough, ridge along the boundary.

- 2c: Asymmetric large oval shaped defect, aligned along [110], accumulation of small oval defects.

- 2d: Large oval shaped defect, aligned along [110], with steps like if grown in several phases on top of each other.

- 2e: Large oval shaped defect, aligned along [110], core is small oval defect without core (like 1a). Flat surface.

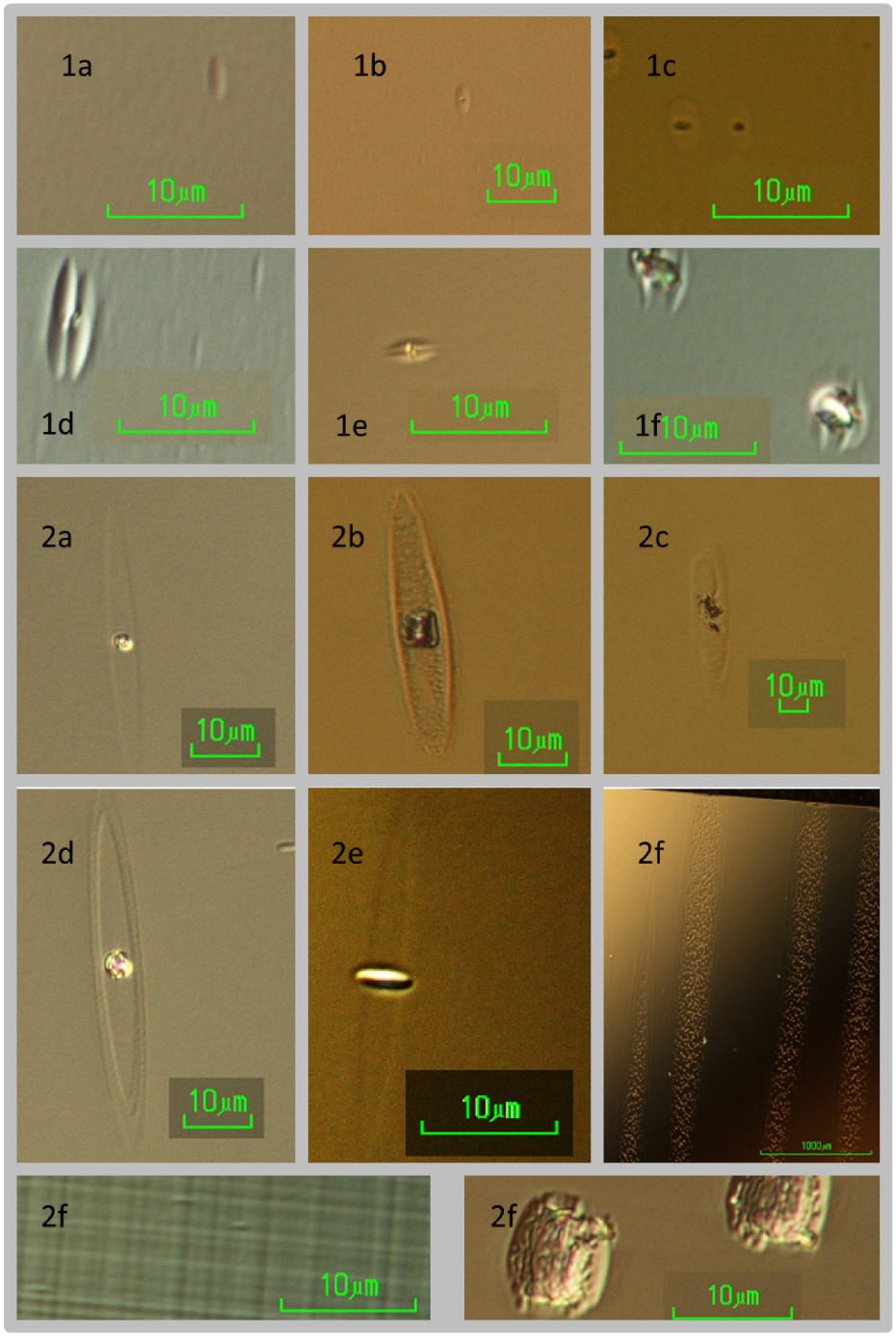

Figure 2.4: Growth defects found in (In,Ga)As on InP.

- 2f: "'tiger stripes"' occurring in case of too high In flux, consisting of cross-hatches (2e), and islands, (2f)

A large number of modifications in growth process have been tested to avoid these defects - beginning with varying the As-overpressure, cleaning processes of the shutters and finally changing the cell temperatures. The change of cell temperatures turned out to be significant for the density of small defects of type 1a. First, for both Indium and Gallium, the difference in temperature between Tip and Base is reduced significantly, from about 150 - 200 °C to 50 °C for Gallium and 15 °C for Indium. This results in a flat background, and also HRXRD measurements confirmed the drastically decreased density of defects - however, the large defects of type 2.a-e occur. It is found that these types of large defects only occur when the Tip and/or Base temperature of the Indium-cell is too low - the Gallium temperature does not effect them and seems responsible for the density of small defects. Thus, the following compromise is found: For the Gallium-cell, the difference between Tip and Base should not be larger than 50 K, whereas the absolute temperature should be high enough to achieve a high enough flux (house numbers are a minimum Base temperature of about 800 °C). For Indium, the difference between Tip and Base temperature can be larger, however the absolute temperature should also be high enough. A typical set of parameters would be: Gallium (Tip/Base) 865/815 °C and Indium (Tip/Base) 850/695 °C. These growth parameters can still result in few large or small defects, meaning that there are still other parameters playing a role that are not found yet - however, as will be seen in the next chapter, the HRXRD measurements suggest a significant improvement of layer quality. The surface roughness of the (In,Ga)As layer will continue throughout the entire sample stack (it is still visible by Nomarski optics when the layer stack including a sputtered cap is completed) and thus determines the interface roughness of NiMnSb and adjacent layers. The reduction and control of these defects described above is thus an important factor for the growth of heterostructures, where interface roughness plays a role.

2.4 Growth of NiMnSb on (In,Ga)As

As described above, for the growth of (In,Ga)As, a very high As flux compared to the fluxes of Indium and Gallium is applied - nonetheless (In,Ga)As with the correct ratio of (In,Ga) to As can be grown. Such growth is called self-limiting, since only the amount of atoms needed to built the crystal correctly is actually incorporated into the sample. For

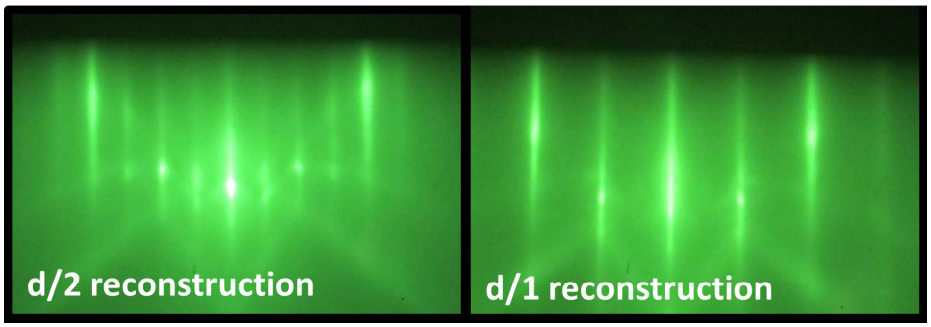

Figure 2.5: RHEED reconstruction of the NiMnSb surface under optimum growth conditions.

NiMnSb, that is not the case. The growth of NiMnSb is stoichiometric, meaning that all atoms that arrive at the sample are built into the crystal structure (with some corrections due to different sticking coefficients for the different materials). The challenge is thus to find the exact flux ratios and achieve highly stable fluxes. As it will be described below, very small changes of cell temperature (even less than 1 K change) can cause a noticeable change in the crystal resulting in significant changes in magnetic properties. The growth rate of NiMnSb is extremely low, compared to other standard MBE growth rates that lie in the range of $1\,\text{Å}\,\text{s}^{-1}$ to $2\,\text{Å}\,\text{s}^{-1}$. Here, the extremely low fluxes result in a growth rate smaller than $0.1\,\text{Å}\,\text{s}^{-1}$. It has turned out previously that this low growth rate improves the crystal quality significantly [28].
The chamber for the NiMnSb growth is prepared by heating all cells to their growth temperature and letting them stabilize for at least 40 min. A cleaning process for the shutters can be applied, where the shutters are closed in front of the hot cells for few minutes and then opened again, which is repeated several times. After the sample is transferred into the chamber, the substrate temperature is set to 250 °C and also let stabilizing at this temperature for several minutes. During this time, the shutters of the cells are open while the main shutter is still closed to avoid peaks in the fluxes that can occur when a shutter in front of a hot cell is opened. Immediately after growth start, the RHEED reconstruction pattern of the cooled down (In,Ga)As buffer can still be seen, with a d/3 reconstruction along $[1\bar{1}0]$ and a d/4 reconstruction along the [110] direction. After 1 - 2 minutes (depending on growth rate), corresponding to about one monolayer thickness, the surface reconstruction changes into a weak (low intensity) d/2 in both [110] and $[1\bar{1}0]$ crystal direction. For all samples, disregarding (moderate) changes in the flux ratios, after few more minutes (usu-

ally around 2 min to 4 min), a clear pattern with a $d/2$ reconstruction in the [110] crystal direction and a $d/1$ reconstruction along $[1\bar{1}0]$ direction (see Fig. 2.5) is seen.
After this first stage of growth, the RHEED pattern evolves differently depending on the flux ratios. The layer thickness at which a change in the RHEED pattern also depends on the amount of change in fluxes - minor changes can cause a change in the RHEED pattern that occurs only after growth times longer than 1 hour (corresponding to layer thicknesses of 10 nm to 20 nm), whereas larger changes can already cause a change in RHEED pattern after few minutes.
In reference [27], an overview for significant changes in flux ratio is shown, where the Sb/Ni flux ratio is either optimum or too high, and within these boundaries, the Mn/Ni flux has been changed. In this thesis, a more detailed study on the RHEED reconstruction is given, where distinct patterns and their crystal direction are presented together with the corresponding relative, qualitative flux ratio. It is difficult to give quantitative values of the flux ratios since the absolute fluxes are very small and cannot be measured with the needed accuracy - thus, a certain RHEED reconstruction (see below) has been identified to be corresponding to the optimum growth conditions and all qualitative changes in flux ratio are referred to these optimum growth parameters. Fig. 2.6 shows a cartoon sketch of all RHEED reconstructions observed for all variations of flux changes. These reconstructions are reproducible and are presented rather than photographs since the latter do not always show all features, especially of low intensity. If available, corresponding photographs are shown in addition. This collection of RHEED patterns is very useful to find the correct growth parameters e.g. after a chamber opening and/or refilling of the cells. Furthermore, it is related to the magnetic and structural properties (like lattice parameter, magnetization and anisotropy, see next two chapters) and thus allows for the control and prediction of sample properties *in-situ*. The next subsections describe the RHEED patterns in detail, together with the corresponding flux changes and possible impact on sample quality.

Optimized fluxes and stable growth of NiMnSb

The optimum growth conditions are considered to be achieved when the RHEED pattern is not changing during the entire growth time of maximal 2h (corresponding to about 40 nm to 60 nm layer thickness), where the d/2 reconstruction is always seen along the [110] crystal direction, the d/1 reconstruction is seen in the $[1\bar{1}0]$ crystal direction. Unfortunately, there is no independent method available to determine the stoichiometry directly like e.g.

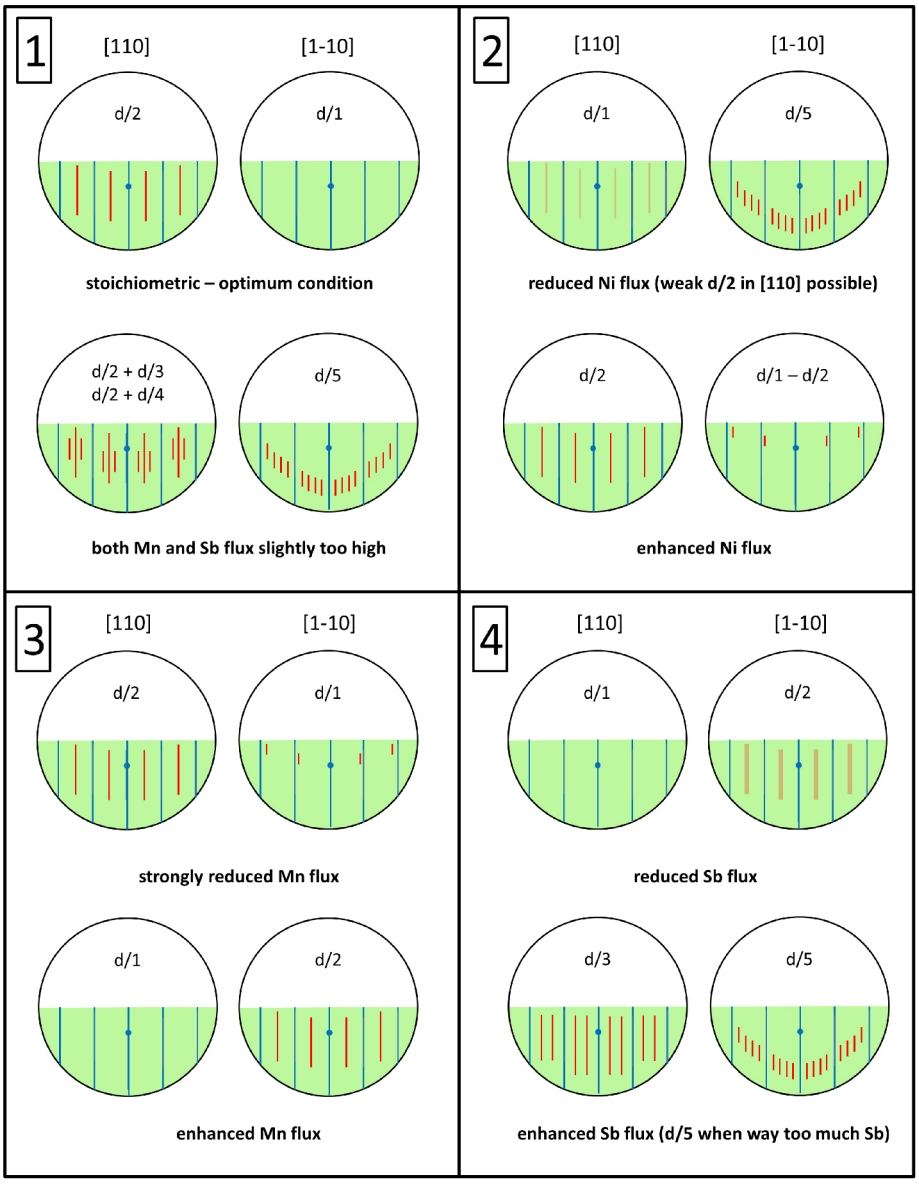

Figure 2.6: Schematics of all RHEED reconstructions observed for stoichiometric and non stoichiometric NiMnSb. In panel 1, upper picture, the reconstruction for optimum growth conditions is shown. Panel 2, 3 and 4 show reconstructions for changes in flux from optimum values for Ni, Mn and Sb, respectively.

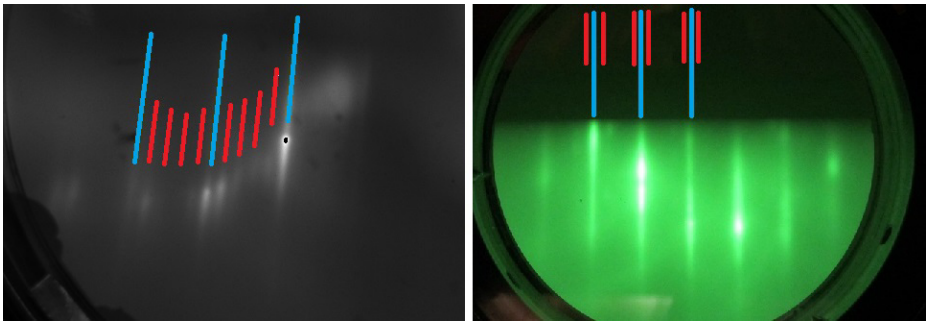

Figure 2.7: Left: RHEED pattern with d/5 reconstruction in case of too low Ni flux along the [110] direction. Right: Asymmetric d/2 pattern in case of too high Ni flux.

Rutherford backscattering. Nonetheless, using the XRD data of a stoichiometric, relaxed sample [15] together with an estimated Poisson's ratio (see section 3.1), a range of vertical lattice constants corresponding to stoichiometric conditions was found. Additionally, the saturation magnetization of theoretical 4.0 μ_B is another indicator for stoichiometry. Investigation of the lattice constant and magnetization indicate that samples with such RHEED pattern are stoichiometric, see also next chapter. For this set of flux ratios, the streaks are clear, elongated and have high intensity, a clear specular spot can be observed which are all signs for high crystal quality. (Schematics of this RHEED pattern see Fig. 2.6, panel 1 and Fig. 2.5.)

Reduced or enhanced Ni flux

Since the Ni flux is the lowest of all three applied fluxes (in the low range of 10^{-9} mbar), already a very small change in temperature and thus in flux has a large impact on the crystal structure and growth. In case of a too low Ni flux, a d/5 reconstruction evolves along the $[1\bar{1}0]$ crystal direction. The d/5-streaks are short and positioned on a half-circle (compare sketch in Fig.2.6, panel 2, and Fig. 2.7 left panel). Along the [110] direction, a very weak d/2 or no reconstruction (d/1) can be seen. With an enhanced Ni flux, the d/2 reconstruction along the [110] direction remains, and an asymmetric reconstruction along $[1\bar{1}0]$ is observed. This asymmetric reconstruction is shown as a schematics in Fig. 2.6, panel 2, and also as a real photograph in Fig. 2.7, right panel.
In case of a very small increase or decrease of the Ni cell temperature, corresponding to a cell temperature change of less than 1 K, the crystal structure can still be of high quality (meaning 2D RHEED pattern) after the growth of about 40 nm. However, if the Ni flux is

further enhanced or reduced, the crystal will exhibit significant surface roughness, resulting in a RHEED pattern consisting of only 3D dots.

Reduced or enhanced Mn flux

A reduction of the Mn flux leads to a more blurry RHEED pattern, however the orientation of the reconstruction of the growth start (d/2 along [110] crystal direction) remains the same. In case of a drastically reduced Mn flux, a similar pattern like for too much Ni can be seen, with an asymmetric reconstruction. Compare Fig.2.6, panel 3. With a surplus of Mn, the d/2 reconstruction is fading away in the [110] direction and appears in the $[1\bar{1}0]$ direction, which can result in a complete rotation of the RHEED pattern by 90°. The d/2 streaks in $[1\bar{1}0]$ direction are shorter than observed in [110] direction for the case of optimum/reduced Mn flux. The thickness at which the RHEED pattern has rotated completely depends on the absolute Mn flux: With only a small surplus of Mn (meaning about 2 K to 3 K above the optimized temperature), the rotation of the RHEED pattern can still be in process at the end of growth, at a thickness of 40 nm. When a strongly enhanced Mn flux is applied (more than 5 K increase in temperature), the rotation can be finished within a few nanometer layer thickness and the rotated pattern is then stable for the rest of the growth time.
The change in Mn flux has less significant impact on the crystal quality than for Ni. Even a strong enhancement of the flux still results in a high crystal quality layer, in fact the thickness oscillations observed in HRXRD (see next chapter, Fig. 3.3) can be of higher intensity for NiMnSb grown with slightly enhanced Mn flux, compared to those grown with the optimized parameters. In the opposite direction, meaning reducing the Mn flux, there is a smaller range of Mn cell temperatures where good crystal quality is still achieved and the thickness fringes are of lower intensity (compare Fig. 3.3 in section 3.1, blue (low Mn) and black (medium Mn) curves).
The change in Mn concentration however has a strong impact on the lattice parameter and magnetic properties as will be described in the following chapters.

Reduced or enhanced Sb flux

With a slightly enhanced Sb flux, the reconstruction in [110] changes from the original d/2 into a d/3 reconstruction, whereas the d/1 reconstruction along $[1\bar{1}0]$ remains unchanged. If the absolute Sb flux is not too high, this reconstruction can be stable for up to 2 h, where

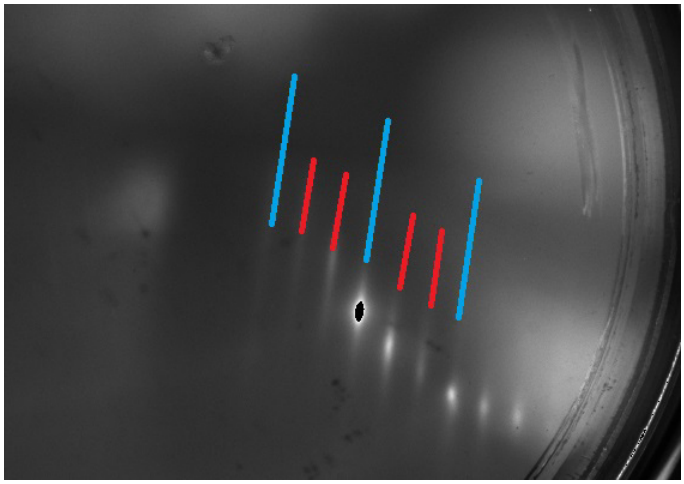

Figure 2.8: d/3 RHEED reconstruction in case of slightly enhanced Sb flux.

the d/3 streaks are short and of high intensity. Fig. 2.6 panel 4 and Fig. 2.8 show this type of RHEED reconstruction. Here, an enhanced Sb flux means an increase of the cell temperature of 1 K to 2 K, with correct cell temperature of around 420 °C. A higher order of reconstruction, a d/5 patterns can be seen along the $[1\bar{1}0]$ crystal direction in case of large enhancement of Sb. When a too small Sb flux is used, the reconstruction rotates, meaning a d/2 pattern along the $[1\bar{1}0]$. However, all streaks get blurry in contrast to the sharp and clear reconstruction in case of enhanced Mn flux. Here, the range of cell temperature for that good crystal quality is achieved is again small, comparable to Ni.

Meaning and analysis of RHEED patterns

Unfortunately, it is impossible to conclude from the observed RHEED pattern to the actual atomic structure of the surface. From a given or assumed structured surface, a corresponding RHEED pattern can be simulated [26], but many different surfaces can exhibit equal or similar RHEED pictures. Thus, the here observed reconstructions can only be related to certain growth conditions, but do not give enough information to extract the exact surface structure and composition.

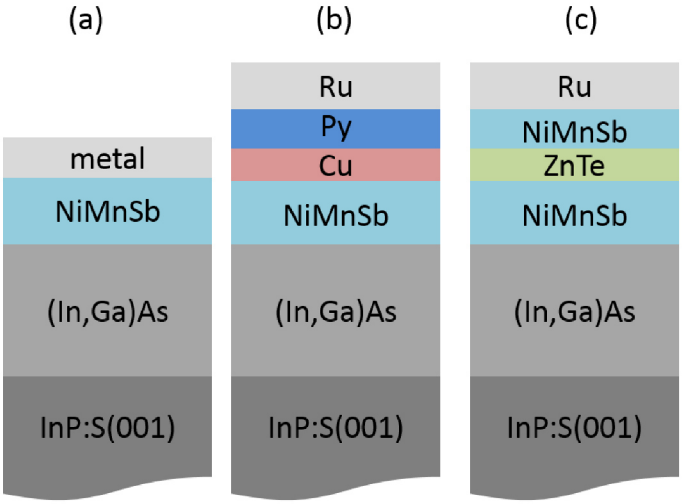

Figure 2.9: Different layer stacks grown during this thesis.

2.5 Summary

In this chapter, the growth processes of (In,Ga)As on InP substrates as a buffer layer and of NiMnSb have been presented. The main challenge in the growth of (In,Ga)As is the reduction of defects or hillock defects that can induce a significant surface and interface roughness that continues throughout the entire layer stack. However, the buffer layer is needed to ensure a stable and epiready substrate for the growth of NiMnSb. Due to the stoichiometric growth of NiMnSb, extremely stable fluxes of the individual elements are essential to achieve an optimum and homogeneous growth. In-situ RHEED observations show the sensitivity of the crystal structure to the composition of NiMnSb - the reconstruction pattern changes depending on the flux ratios, where small changes in cell temperature of 1K can already decide whether a layer has a flat 2D surface or exhibits significant surface roughness.

With the above described methods and processes, different layer stacks are grown for different studies: In Fig. 2.9, three exemplary layer stacks of the three different types of samples grown during this thesis are shown. On single layers of NiMnSb (a), the main part of the investigations presented in this thesis are conducted. Single layers with a wide variation of thicknesses, composition and capping material are grown and the corresponding structural and magnetic properties are investigated. Most single layers are grown to study the magnetic anisotropy - depending on all composition, thickness and capping material.

Stack example (b) shows a GMR stack, where a second ferromagnetic layer (Permalloy, NiFe) is deposited, separated by a conducting spacer layer, here Cu. The work (processing and transport measurements) on these layers is described elsewhere [30], [31]. A third kind of layer stacks is a heterostructure composed of two NiMnSb layers separated by ZnTe. This special layer stack is an application of the gained knowledge on the control of the anisotropy - growth processes and both structural and magnetic characterization will be described in chapter 5.
In the following chapter, the basic characterization of the NiMnSb single layers is presented.

Chapter 3

Characterization of NiMnSb single layers by HRXRD and SQUID

The basic characterization of the samples contains structural investigations by High resolution X-Ray diffraction (HRXRD) to determine e.g. the lattice parameter and SQUID measurements to get information on the magnetic properties. Both lattice parameter and saturation magnetization give quantitative information that can be related to the composition of the grown material. These parameters can then be used as a measure for investigations of other properties and their dependence on the composition.

3.1 Structural characterization by HRXRD

The structural characterization of the samples is done by High resolution X-Ray diffraction (HRXRD) measurements, and standard $\omega - 2\theta$-scans and ω-scans are recorded. The diffraction pattern is an image of the reciprocal lattice and allows for the analysis of lattice parameter and crystal quality. In Fig. 3.1 left, the reciprocal (h=0,k=0,l=l) crystal direction of two crystals with different vertical lattice constants is shown. Here, the InP/(In,Ga)As substrate has a smaller vertical lattice constant than NiMnSb, resulting in a larger lattice constant in reciprocal space. The red vectors $\vec{k}$ and $\vec{k'}$ represent the incident and diffracted wavevectors, respectively. In an $\omega - 2\theta$-scan, the detector angle 2θ is swept with the double rate as the sample angle ω so that the addition of the incident and diffracted wavevector runs along the (0 0 l) direction, resulting in high intensity peaks whenever a diffraction center (lattice point) is hit. To decide which reflex exhibits highest intensity, scattering

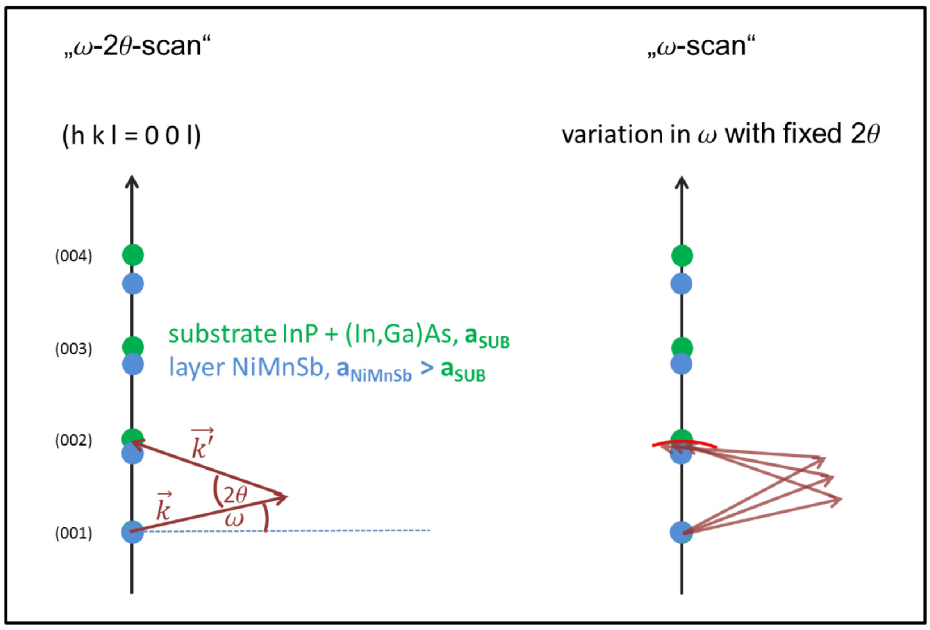

Figure 3.1: Left: Reciprocal space schematics of the (0 0 l) direction. Right: ω-scan.

factors have to be considered - for NiMnSb the (002) Bragg reflection turns out to yield highest intensity [27]. From the distance between two peaks, the vertical lattice constant can be calculated, as described in the next subsections, where peaks at smaller angles correspond to crystal structures with larger lattice constant in real space.
In an ω-scan, the 2θ-angle is kept constant, thus the direction in an arc across the (0 0 l) direction is scanned - see Fig. 3.1, right panel. In case of lattice defects, parts of the crystal will exhibit a change in crystal orientation and thus a diffraction signal is measured for a wider range of angles and the ω-peak will be broadened. For a sample with very low crystal disorder, the ω-peak is narrow. The ω-scan and quantitatively its FWHM is thus a measurement of the crystal quality of the sample and can be compared to other materials/structures.

A standard $\omega - 2\theta$-scan of a single NiMnSb layer is shown in Fig. 3.2: Peak 1 originates from the InP substrate and superimposed, lattice-matched (In,Ga)As buffer, peak 2 originates from the NiMnSb layer with larger vertical lattice constant than the substrate-buffer peak. The features labeled with (3) and (4) are resulting from interference of the X-rays at the interfaces of a layer and called thickness fringes. These fringes can be compared to a diffraction pattern resulting of a slit, where the width of this slit is here the thickness of the corresponding layer. The intensity of these thickness fringes depends on the smoothness of

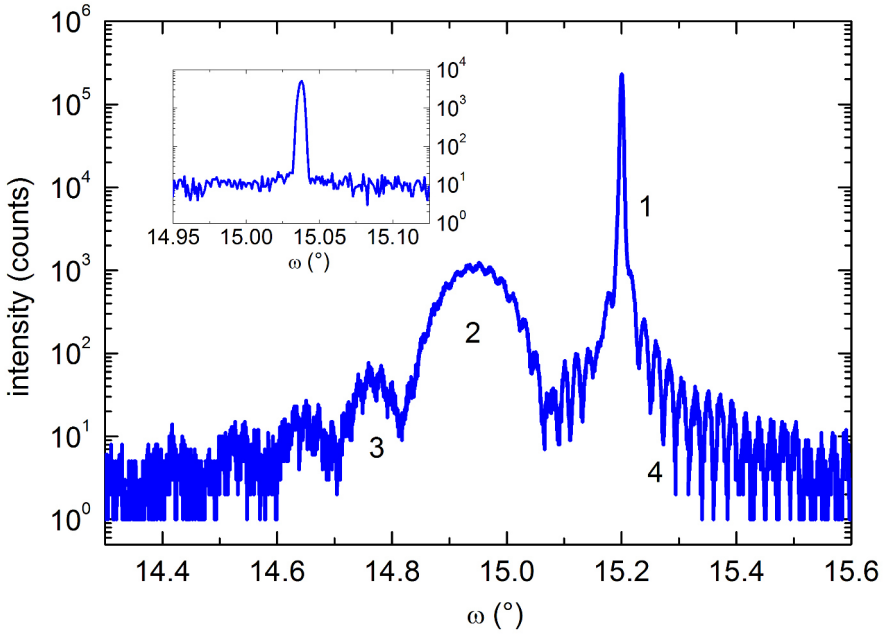

Figure 3.2: HRXRD ω-2θ-scans of a NiMnSb sample. Inset: ω-scan of the NiMnSb layer peak showing high crystalline quality.

the interface of the corresponding layer with adjacent layers and are thus an indication for the crystal quality. Besides that, the thickness t of a layer can be determined by measuring the spacing of the related thickness fringes at angles $\omega_{1,2}, \theta_{1,2}$ and is calculated by [32]:

$$t = \frac{\lambda \cdot \mid \gamma_H \mid}{\delta\theta \cdot \sin(2\theta)} \tag{3.1}$$

Here, λ is the wavelength of the X-rays, $\delta\theta$ is the spacing of two adjacent fringes at angles $\theta_{1,2}$, $\mid \gamma_H \mid$ corresponds to the sine of the angle between diffracted beam and sample surface $((\omega_1 + \omega_2)/2)$.

Poisson's ratio

When a crystalline structure is grown fully strained on a substrate, ideally the lateral lattice constant remains unchanged and subsequently, the vertical lattice constant must change to preserve the volume of the unit cell. However, due to the elasticity modulus of the crystal structure and the bindings within it, the vertical lattice constant cannot increase such that the volume of the unit cell is completely preserved. The scaling factor that determines

how much the vertical lattice constant is stretched when grown fully strained on a given substrate, is called the Poisson's ratio ν. Together with the known lattice constant of the substrate a_S and the lattice constant of a relaxed layer a_{rel}, the vertical lattice constant $a_\perp$ can be calculated by the following formula (taken from reference [27]):

$$a_\perp = \frac{a_S^2(\nu - 1)}{(\nu + 1)a_{rel} - 2a_S} \tag{3.2}$$

On the other hand, if the vertical lattice constant is known (e.g. as here measured by HRXRD scans), the relaxed lattice constant of the material can be determined - assumed that the Poisson's ratio is known. Thus, in order to determine the Poisson's ratio of a material, the lattice constant of a relaxed layer AND the vertical lattice constant of a fully strained layer need to be known. In case of NiMnSb, one would need 1) information about the stoichiometry, 2) the relaxed lattice constant of stoichiometric NiMnSb and 3) the vertical lattice constant of fully strained NiMnSb on a given substrate. Such measurements have been reported in references [27] ($\nu = 0.27$) and [33] ($\nu = 0.15$), with the assumption of stoichiometric NiMnSb. However, the large discrepancy between those two experimental values shows that the two corresponding samples must have different composition, since HRXRD measurements of the lattice parameters are usually quite accurate and do not allow such large errorbars. Since the majority of materials exhibit a Poisson's ratio in the range of 0.3, for the following analysis of HRXRD data, this value is assumed for NiMnSb with a relative error of 10%.

Vertical lattice constant

Using the distance between the two peaks of the NiMnSb and the buffer/substrate layer and the known lattice constant of InP (5.869 Å), the vertical lattice constant of the NiMnSb layer can be calculated by Bragg's Law:

$$2dsin(\theta) = \lambda \tag{3.3}$$

where $d = a/\sqrt{h^2 + k^2 + l^2}$ with the lattice constant a and the Miller indices h, k and l. λ is the wavelength of the used X-rays and θ the angle of the peak. For all of the here presented measurements, the (002) reflex is used, resulting in $2d = 2a/\sqrt{2^2} = a$. Thus, it is

$$\begin{aligned} a_{InGaAs} \cdot \sin(\theta_{InGaAs}) &= a_{NiMnSb} \cdot \sin(\theta_{NiMnSb}) \\ a_{NiMnSb} &= a_{InGaAs} \cdot \frac{\sin(\theta_{InGaAs})}{\sin(\theta_{NiMnSb})} \end{aligned} \tag{3.4}$$

and the vertical lattice constant a_{NiMnSb} can be calculated.
To find the vertical lattice constant for stoichiometric NiMnSb, an XRD measurement of a stoichiometric sample (stoichiometry has been confirmed by Rutherford Backscattering experiments) from reference [15] is used: A 125 nm thick layer of NiMnSb has been grown on GaAs (111), resulting in a sample that is assumed to be relaxed due to the large lattice mismatch between GaAs and NiMnSb of more than 4% (for ZnTe on NiMnSb, the critical thickness after that relaxation will occur has been estimated to be 1 nm for a similar lattice mismatch of about 3%, see chapter 5). The relaxed lattice constant was determined to be $a_{rel} = (5.926 \pm 0.007)\,\text{Å}$, and together with the lattice constant of the here used InP/(In,Ga)As substrate, 5.8688 Å, and an estimated Poisson ratio of 0.3 ± 0.03, the maximum and minimum vertical lattice constants expected for stoichiometric NiMnSb are: $a_{\perp,max} = 5.999\,\text{Å}$, $a_{\perp,min} = 5.957\,\text{Å}$.

Comparing $\omega - 2\theta$-scans of various NiMnSb samples, it is found that the position of the

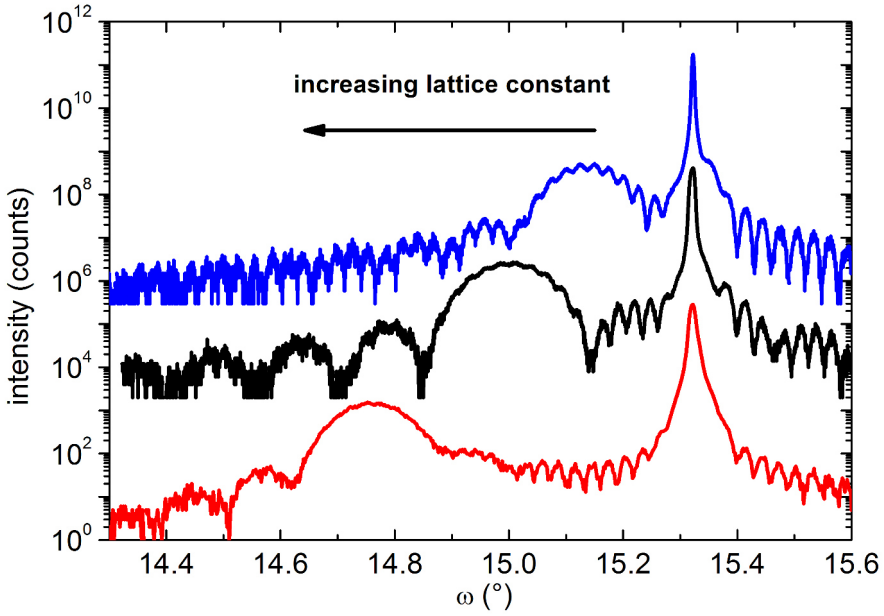

Figure 3.3: HRXRD ω-2θ-scans of three NiMnSb samples with different Mn concentration (blue: lowest, red: highest).

NiMnSb-peak shifts, in comparison with the InP-substrate peak. This behavior of varying vertical lattice constant correlates with the Mn concentration in the sample: Layers with a high Mn concentration exhibit a larger vertical lattice constant than layers with a reduced

Mn concentration, where an almost linear behavior could be observed (see Fig. 3.10 in section 3.4). For three different samples with different vertical lattice constants the $\omega - 2\theta$-scans of the (002) Bragg reflection are shown in Fig. 3.3. The sample with the highest Mn content (red) has a vertical lattice constant of 6.092 Å and that with the lowest Mn content (blue) has a lattice constant of 5.939 Å. The sample with medium Mn concentration (black) has a vertical lattice constant of 5.994 Å and thus lies in the range of stoichiometric NiMnSb.

ω-scans

In Fig. 3.4, the ω-scans for the three samples presented in Fig. 3.3 are shown. As said before, the FWHM of the ω-peak is a measure for the crystal quality - here, both samples with low and medium Mn concentration (blue and black) exhibit narrow FWHM in the range of 15 arcsec. Such narrow ω-widths are comparable with the single crystal quality

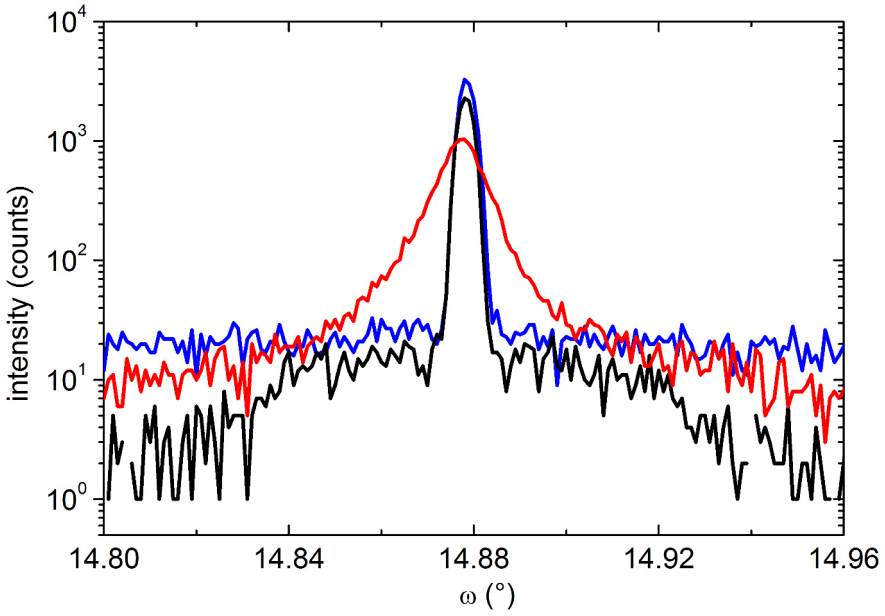

Figure 3.4: ω-scans for the three samples shown in Fig.3.3: The sample with largest lattice constant and thus largest lattice mismatch exhibits a broadening of the ω-scan (red).

of semiconductors and are a sign of extremely high crystalline quality. In case of very large Mn concentration (red curve) a broadening in the ω-scan is observed, with a FWHM

of 35 arcsec, which is nonetheless still very good. The broadening can be explained by the significantly enlarged lattice mismatch between the buffer and the NiMnSb layer, and resulting massive strain and possible partial relaxation.
The background of the ω-peaks gives information on the defect density in a crystal structure. Especially for the (In,Ga)As buffer layers, this is a method to determine the optimum growth conditions discussed in the previous chapter. In Fig. 3.5, the ω-scans of three buffers grown with different cell temperatures are shown: In sample A, the cell temperatures of

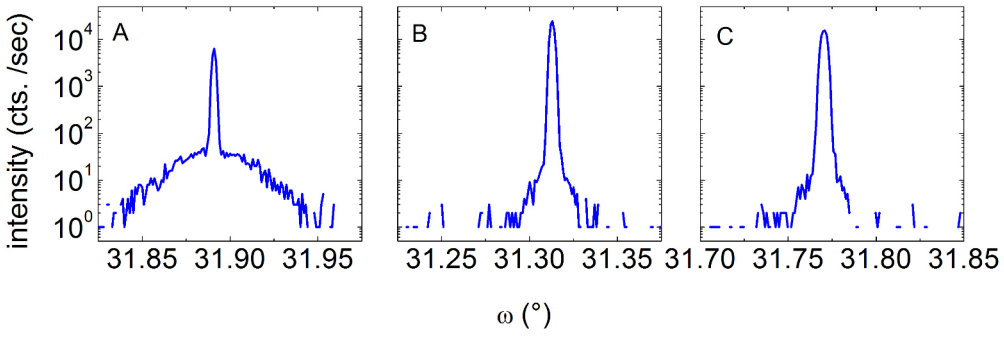

Figure 3.5: ω-scans of three differently grown (In,Ga)As buffer layers.

Tip and Base for both Gallium and Indium have a difference of more than 100 °C, resulting in many oval defects in the background (see also Fig. 2.4 1a). A high intensity and broad background in the ω-scan is the result - the scan can be interpreted by an addition of a sharp peak with no background, coming from the parts of the layer with high crystalline quality, and a broad low intensity peak, coming from the defect parts of the layer. Sample B is grown with small temperature differences between Tip and Base for both Indium and Gallium, resulting in an ω-peak with significant reduced background - this means that only a very small fraction of the layer exhibits defects. By optical microscopy it was found that large oval defects are still present (compare defects type 2 in Fig. 2.4), however with a much lower density than small oval defects. By combining a small difference in temperature of Tip and Base for Gallium and a big difference for Indium, sample C is grown, avoiding large oval defects and small oval defects in the background at the same time. As can be seen, the background of the ω-peak is very small as well, indicating high crystal quality of the buffer layer.

3.2 Magnetic characterization - SQUID

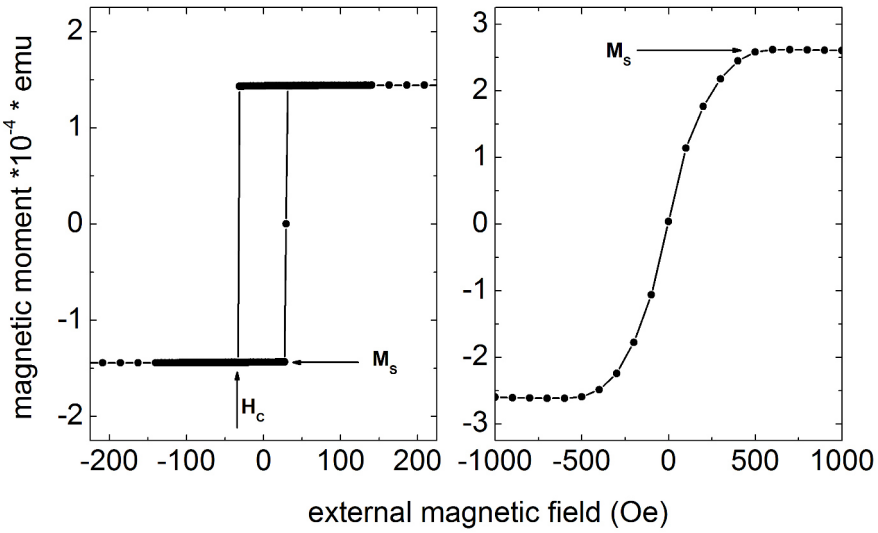

Figure 3.6: Hysteresis curves of two single layers NiMnSb, exhibiting an easy axis (left panel) and a hard axis (right panel).

The saturation magnetization of NiMnSb is another property that gives information on the composition of the layer and is thus an important parameter to compare between different samples. A SQUID (superconducting quantum interference device) is a tool to measure with high accuracy and high resolution the magnetization of a sample responding to an external magnetic field. In a standard hysteresis curve, the external magnetic field is swept from high positive to high negative values and back in opposite direction, while measuring the magnetic moment of the sample. At high positive and negative external fields, the sample is saturated, where this term is used here to describe the state of parallel alignment between the magnetization and the external field. In other contexts, the saturation magnetization can describe the state where all domains in a sample are aligned parallel to each other.
In Fig. 3.6, exemplary hysteresis curves for two single layers are shown. The shape of the hysteresis curve gives information on the magnetic anisotropy and coercive field H_C as well as saturation magnetization M_S. The sample in the left panel exhibits an easy axis that is characterized by the sharp switching event at a small negative field (coming from positive) and a small positive field when coming from high negative fields. The magnetic field required to switch the easy axis is called the coercive field H_C, and can be seen as

a measure for the strength of the anisotropy: The higher the field needed to switch the magnetization from its energetically favored position (along easy axis) the stronger the anisotropy is.
The magnetization in the right panel does not switch but rather rotates gradually, beginning already at high fields, and thus exhibits a hard axis. In case of zero external magnetic field, an ideal hard axis aligns itself 90° to the measurement axis, still in-plane, and thus giving zero response. In comparison with the easy axis, the magnetic field at which the magnetization starts to rotate can be seen as a measure for the strength of the hard axis.
As mentioned above, the saturation magnetization is determined by the measured magnetic moment at large external magnetic fields, where a change in magnetic field does not change the measured magnetic moment. In theory, the saturation magnetization M_S in units of μ_B of Half-Heusler compounds can be calculated by the Slater-Pauling rule that says ([34], [35]):

$$M_S = (N_V - 18) \times \mu_B \tag{3.5}$$

where N_V is the average valence electron number per formula unit (here: $N_V = 22$). In NiMnSb, [NiSb]3- and [Mn]3+ hybridize, resulting in four unpaired electrons at the Fermi energy, leading to the saturation magnetization of 4.0 μ_B per unit formula, see also reference [36]. Only in case of stoichiometric NiMnSb, this value for M_S can be found - all changes in composition or defects result in values smaller than 4.0 - see also next section 3.3.
It has been reported that the majority of the magnetic moment (above 90%) is located at the Mn atom [37], [16]. Thus, it is not surprising that a change in Mn concentration effects significantly the magnetization of NiMnSb. To be more precise, the saturation magnetization M_S changes with off-stoichiometric defects [38], thus being a measure for the composition of the sample.
To calculate M_S using hysteresis curves measured by SQUID, the unit formula for NiMnSb needs to be calculated:

$$1u.f. = \frac{4}{(a_{rel})^3} = \frac{4}{(a_{rel})^3 \cdot 10^{27}} m^{-3} \tag{3.6}$$

with a_{rel} being the relaxed lattice constant of NiMnSb. When M_S is the magnetic moment at saturation from a hysteresis curve (in units *emu*) and V is the volume of the sample (in cm^3), it is:

$$M_S[\mu_B] = \frac{\frac{M_S}{V} \cdot 1000}{1u.f. \cdot \mu_B} \tag{3.7}$$

For samples in the stoichiometric region (meaning samples with vertical lattice constants in the stoichiometric region and according RHEED patterns), the measured saturation magnetization agrees well with the theoretical value of 4.0 μ_B within the estimated errorbars of 8%. This error accounts mainly for errors in the measurement of the volume (area measured with caliper, thickness measured by HRXRD thickness fringes). This is a further confirmation that the RHEED pattern indicated as optimum and resulting lattice constant are consistent and actually are parameters that can be expected for stoichiometric NiMnSb. For samples with a variation in Mn concentration, both reduced or enhanced, the saturation magnetization is found to be smaller than 4.0 μ_B, even within the errorbars. For the sample with highest Mn concentration (being the sample with largest lattice constant, see Fig. 3.3 red curve) a saturation magnetization of about 3.5 μ_B is measured.
A change in Mn flux and thus in Mn concentration has obvious effects on both structural and magnetic properties of the samples - in the following, off-stoichiometric defects and their effect on the properties of NiMnSb are presented as they are discussed in references [39] and [38]. It will be concluded that the change in Mn concentration can be related to one certain kind of defect.

3.3 Nonstoichiometric defects in NiMnSb

In references [38] and [39] (the latter is a detailed case study for one specific defect), a theoretical study on all possible defects in NiMnSb, covering interstitial, antisite and additional vacancies, is shown, where probability (formation energy) and effects on lattice constant and magnetic properties are reported as well. In the following, these three types of defects are described:

a) *Interstitial defects* are defects where the natural vacancy position in the NiMnSb lattice is occupied by an additional atom, so these can be either Ni_I, Mn_I or Sb_I. Among these, Ni_I has the lowest formation energy of 0.2 eV and is thus highly probable, which is not surprising since it leads to the Full-Heusler Ni_2MnSb. This is a further indication that extremely stable and well calibrated Ni fluxes are needed for the growth of stoichiometric NiMnSb. The second type of defect, in case of Mn occupying the vacancy position Mn_I, the formation energy is significantly larger (0.73 eV). Sb_I has a very high formation energy of 8.19 eV and is thus very unlikely to occur. These interstitial defects have a very small positive or none effect on the

saturation magnetization, and except for Sb_I the half-metallic character is preserved. The reported change in saturation magnetization of 0.008 μ_B per unit formula is too small to be detected by the standard SQUID measurements presented above, corresponding to a relative change of 0.2% (being 40 times smaller than the relative error). Thus, even if defects of this kind occur, it would be hard to detect them by SQUID measurements.

b) An *antisite defect* describes the situation where a certain lattice site is occupied by an atom that normally occupies a different lattice site. Thus, in NiMnSb the six corresponding defects are Mn_{Ni}, Mn_{Sb}, Ni_{Mn}, Ni_{Sb}, Sb_{Mn} and Sb_{Ni}. Among these defects, Mn_{Ni} has the lowest formation energy (0.49 eV), whereas all others, especially those associated with Sb, have rather large formation energies, ranging from 0.92 eV for Ni_{Mn} to 6.47 eV for Sb_{Ni} and are considered to be unlikely to occur. In reference [39], the special case of Mn_{Ni} is investigated in more detail - it is found that the lattice constant increases with increasing concentration of this kind of defect, while the saturation magnetization decreases. This is exactly the behavior of the here presented samples grown with varying Mn flux - it was concluded that the antisite defect Mn_{Ni} is the most present defect in those samples and the corresponding change in lattice constant (which can be measured most accurately) can be used as a measure for the Mn concentration.

c) The third type of defect is an additional vacancy position at a normally occupied lattice site, vac_{Ni}, vac_{Mn} or vac_{Sb}. Formation energies for these defects are above 1 eV, making them unlikely - they are shown here for the sake of completeness.

Remark concerning formation energies and probability of the above stated defects Mn_I and Mn_{Ni}: To estimate the probability $P_{Mn_I,Mn_{Ni}}$ of occurrence of these defects, the Boltzman distribution is used where $P_{Mn_I,Mn_{Ni}} \propto \exp\frac{-E}{k_B \cdot T}$. The formation energies E of these two defects are 0.73 eV *and* 0.49 eV *respectively, the temperature of the system during growth is* 250 °C *or* 523 K. *As a result, the probability of defect Mn_I is $P_{Mn_I} \approx 9 \times 10^{-8}$ and thus a factor of 200 smaller than $P_{Mn_{Ni}} \approx 2 \times 10^{-5}$.*
In the C1b structure of NiMnSb, the atoms on the space diagonal in the unit cell are occupied by X_1, X_2, Y and Z, where X_1 (1/4) is the vacancy position, X_2 = Ni (3/4), Y = Mn (0) and Z = Sb (1/2), see Fig. 3.7, the stacking order is thus Mn, vacancy, Sb, Ni (or when starting at Ni: Ni, Mn, vacancy, Sb). This lattice exhibits two alternating lattice

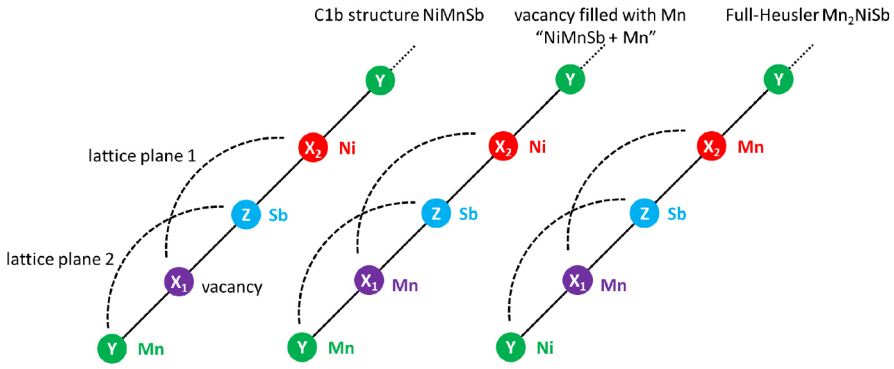

Figure 3.7: Atomic order on the space diagonal in the unit cell.

planes in the (001) stacking direction: one occupied with Ni and the vacancy position, the other occupied with Mn and Sb, indicated with black dotted lines. When theoretically filling the vacancy position X_1 with Mn, the resulting crystal structure "NiMnSb + Mn" would have the stacking order Mn, Mn, Sb Ni and thus Mn and Ni would occupy one lattice plane, Mn and Sb the other lattice plane. The hypothetical Full Heusler "Mn_2NiSb" however has two Mn atoms sitting on lattice sites X_1 and X_2 as shown on the right in Fig. 3.7. This lattice structure is not equivalent to the "NiMnSb + Mn" structure!
To sum up, simply filling up the vacancy position will not result in a Full Heusler structure (this would only be the case for filling the vacancy position with Ni, consistent with the low formation energy for this kind of defect) and the defect of type Mn_I is unlikely. On the other hand, Mn substituting Ni is much more likely and also consistent with characterization measurements, see sections above and also next section.

3.4 Actual Mn concentration in NiMnSb

In order to get an estimate on the actual Mn concentration, XPS measurements on a set of four samples grown with different Mn cell temperatures are conducted *in-situ*, directly after growth before adding a cap layer. Two of these samples are grown with lower Mn cell temperature, the other two are grown with increased Mn cell temperature (difference in temperature: 5 K). XPS can be a useful method to determine the composition, however it is very surface sensitive, thus the results have to be evaluated with caution. In Fig 3.8, the single XPS spectra for Ni, Mn and Sb are shown. From the single measurements, the integrated peak area is determined and scaled with atomic scattering factors (Ni 2p: 5.4,

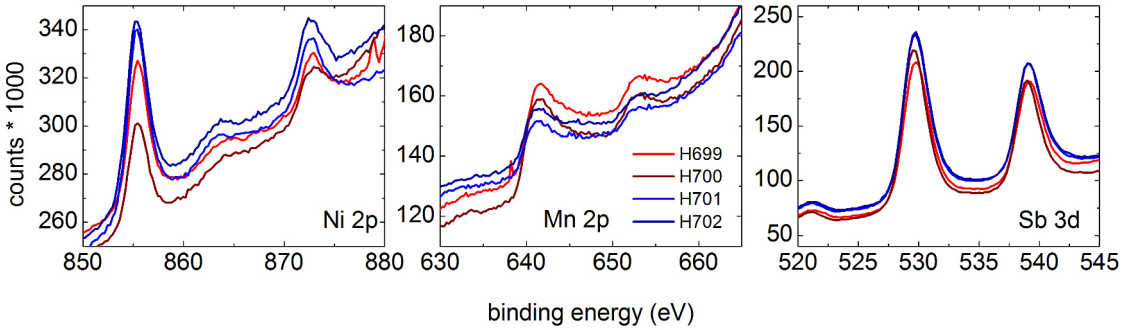

Figure 3.8: XPS spectra for samples with different Mn concentration. Sample H699 and H700 are grown with higher Mn flux than samples H701 and H702.

Mn $2p_{3/2}$: 2.1 and Sb $3d_{5/2}$: 3.55, [40]). For each element of each sample, this scaled peak area is divided by the sum of all three peak areas to determine the ratio, thus representing the relative peak area and the relative amount of material. These values (relative peak area) are plotted in Fig. 3.9 versus the lattice constant of these samples (H699 and H700 are grown with higher Mn flux than samples H701 and H702). First of all, it is obvious that these values cannot represent the actual concentration of each element, since according to these measurements the composition Ni:Mn:Sb would be 20:20:60 for the samples with lower Mn concentration. Samples with that composition are not considered to yield the theoretically expected saturation magnetization and lattice parameter - as these samples do (samples H699 and H700 have vertical lattice constants of 5.99 Å and 5.98 Å, whereas samples H701 and H702 have smaller lattice constants of 5.95 Å). The drawback of this method is the in general small sampling depth of only few nanometers - the energy used for these measurements is 80 eV, resulting in electron mean free paths of 2 nm to 3 nm [40], [41]. To make this even worse, it has been reported that in NiMnSb, Mn segregates at the surface [17], making XPS even more inappropriate to determine the absolute Mn concentration of a bulk sample. Nonetheless, it can be seen that for the two samples grown with higher Mn flux, the relative peak area of Mn increases and the relative peak areas of Ni and Sb are constant or decreasing slightly. This can bee seen as evidence that in samples grown with increased Mn flux actually more Mn is incorporated in the crystal, at least in the surface region.

In Fig. 3.10, the vertical lattice constant of several samples grown with different Mn cell temperature whereas Ni and Sb cell temperatures are stable, are shown (black filled

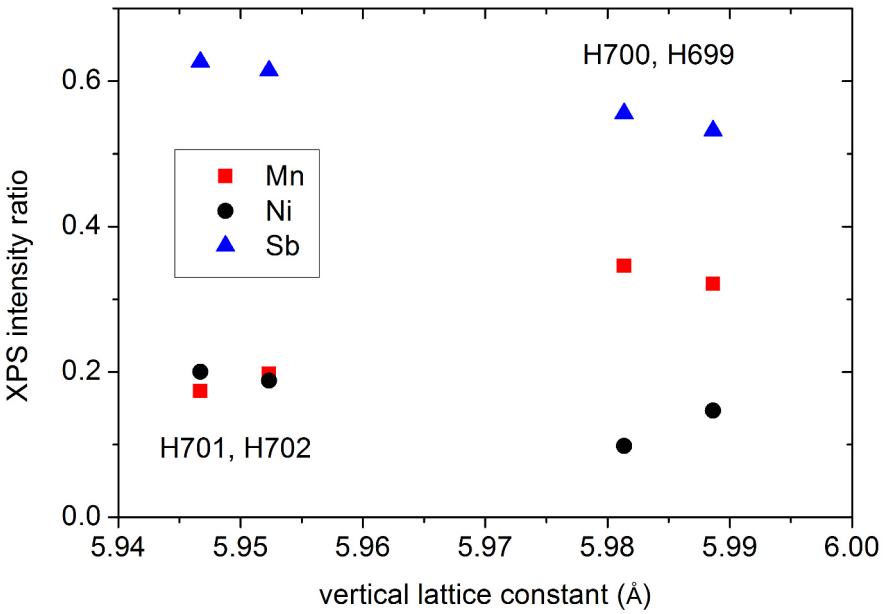

Figure 3.9: Relative peak area of XPS measurements (individual peak area for Ni, Mn and Sb divided by sum of peak areas (Ni+Mn+Sb).

squares). It can be seen clearly, that the increase of the cell Mn temperature actually increases the lattice constant of the resulting crystal, exhibiting an almost linear behavior. The inset shows measurements of the BEP (beam equivalent pressure) measured for different Mn cell temperatures in that range, with a difference in flux between the two extrema of approximately 40%. In this graph, the vertical lattice constant for additional samples are shown as well (colored crosses) - the samples represented by purple crosses were grown in the same growth period as the previous set (black squares) and show similar vertical lattice constants for corresponding Mn cell temperature. However, samples grown in earlier time periods (green and blue crosses) where cell filling levels and absolute cell temperatures were different, show also different resulting vertical lattice constants. But again, the increase of cell temperature results in an increase of lattice constant (blue crosses). This emphasizes again that the growth is extremely sensitive to changes in cell temperatures, and that the vertical lattice constant has to be used as a measure for the Mn concentration rather than the measured flux or cell temperature.

From two experimental data points taken from reference [39], an estimate of difference

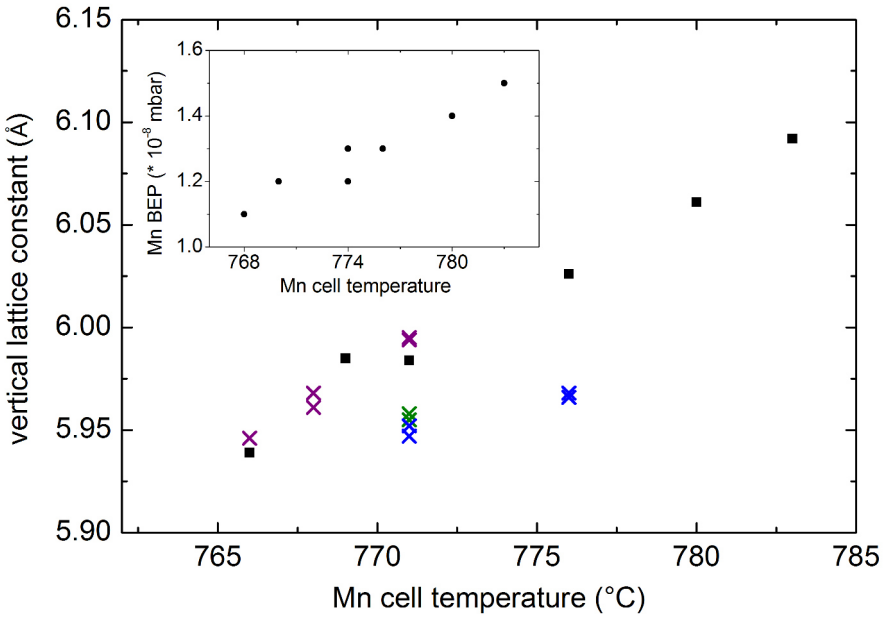

Figure 3.10: Vertical lattice constant of NiMnSb layers grown with different Mn cell temperature, where Ni and Sb temperatures are kept constant (black squares, purple crosses). Blue and green crosses: vertical lattice constant of samples from earlier growth periods where cell filling level and absolute cell temperatures were different. Inset: measured beam equivalent pressure (BEP) at different Mn cell temperatures.

in absolute Mn concentration can be done: The given lattice constants are 5.918 Å and 5.954 Å, corresponding to vertical lattice constants of 5.96 Å and 6.03 Å for a substrate lattice constant of 5.8688 Å (InP) and assumed Poison's ratio of 0.3. This increase in lattice constant corresponds to an increase in Mn concentration of 17%, accordingly, a change in vertical lattice constant of 0.01 Å represents a change in Mn concentration of 2.4 %. The range of vertical lattice constants in the here (Fig. 3.10) presented samples is 0.16 Å that corresponds accordingly to a difference in Mn concentration of 38%. This value is surprisingly consistent with the 40% change in Mn flux - however it must be noted that this is only a very rough estimate coming from two data points. Quantitative results could be achieved by other methods like Rutherford Backscattering - however, no such setup has been available for this thesis.

3.5 Summary

This chapter described the basic characterization methods and analysis to determine parameters that allows one to deduce on composition and stoichiometry of the grown samples. HRXRD measurements to determine the structural properties have been presented - one main parameter that is analyzed is the lattice constant, that has been found to change with changing composition of the material. Changing the Mn concentration while keeping the Ni and Sb concentration stable results in a vertical lattice constant larger (more Mn) or smaller (less Mn) than expected for stoichiometric NiMnSb. It can thus be used as a gauge for the Mn concentration when comparing other properties depending on the Mn concentration since there is no method to determine the composition directly available. Omega-scans are used to determine the crystal quality of the samples, where extremely narrow linewidths are measured for samples in the stoichiometric region and in a certain range around. Going to far off-stoichiometric NiMnSb (increased Mn concentration) can result in a broadening of the omega-peak, resulting from the increased lattice mismatch between NiMnSb and the buffer underneath. The background of an omega-scan can also be used to determine the degree of defect density as in the case of the (In,Ga)As buffer layers which is an important factor regarding interface roughnesses in a layer stack.
The magnetic characterization of the NiMnSb layers is done by SQUID measurements to determine the saturation magnetization. The theoretical expected value of 4.0 μ_B is achieved for samples in the expected stoichiomteric region within the errorbars, and decreased values are measured for samples with decreased or increased Mn concentration.
The actual Mn concentration cannot be determined by the available methods. Surface sensitive XPS measurements show an increase of the Mn concentration, however absolute values cannot be derived. An evaluation of lattice constants of samples depending on the actual Mn cell temperature used for the growth show an increase of lattice constant with increasing Mn cell temperature. However, it also shows that the cell temperature (or corresponding flux) cannot be used as a measure for the Mn concentration.
To sum up, the lattice constant measured by HRXRD is the most accurate method to evaluate the Mn concentration in these samples. The change in structural and magnetic properties (saturation magnetization measured by SQUID) for increased Mn concentration is consistent with an increasing density of defects of type Mn_{Ni}.

Chapter 4

Magnetic anisotropy in NiMnSb

The magnetic anisotropy of a ferromagnet is one of its important properties. It describes the energetically favored and unfavored directions of the magnetization and is thus essential to be known for the design of devices where state and orientation of the magnetization are functional parameters. The preferred axis is called easy axis and indicates the direction the magnetization is aligned to in case of equilibrium and zero external influence. The opposite direction (in case of uniaxial anisotropy, that will be 90° rotated to the preferred axis) is called hard axis - maximum energy is needed to align the magnetization along that direction. In a cartoon picture, the easy axis corresponds to a valley in the potential surface, whereas the hard axis describes a hill.
So far, the state of the art was that the magnetic anisotropy in NiMnSb is thickness dependent [42], and the crystal direction of the easy axis rotates by 90° while going from thin to thick films. While attempting to reproduce this result, it is found that this behavior is not always valid and other parameters than thickness play a role as well. Investigations on single layers of NiMnSb of both small and large layer thickness reveal that the exact composition of the NiMnSb not only changes lattice parameter and saturation magnetization as described in the previous chapter, but also has significant influence on the magnetic anisotropy. In this chapter, the method and analysis of FMR (ferromagnetic resonance) is presented that is used to determine the anisotropy, followed by several studies on samples with varied composition as well as different thicknesses and capping materials. An attempt to describe the behavior is made, however there is still no detailed microscopic picture that describes the anisotropy in NiMnSb. Nonetheless, Mn turns out to be the most influencing factor and can be used to control both strength and orientation of the anisotropy.

4.1 Ferromagnetic resonance - measurement methods and analysis

FMR - ferromagnetic resonance - is a method to investigate various magnetic properties of a ferromagnet. In the classical picture, an external, tunable, magnetic DC field excites the magnetization of the sample, where its frequency (Lamor frequency) is proportional to the magnetic field strength $\omega = -\gamma \cdot B$ (γ is the gyromagnetic ratio). Additionally, a high frequency (hf) signal is applied to a waveguide directly underneath the sample. In case of resonance, the Lamor frequency matches the frequency of the hf-signal and an absorption signal can be measured. The magnetic field required to match this high frequency is the so-called resonance field H_{res}. In the QM picture, in the case of resonance, the spins of the ferromagnet are driven by the hf field which is then acting like an angular momentum on the magnetization vector. This leads to zero angular momentum when the magnetic field and thus the magnetization vector is parallel to the magnetic field component of the hf signal (that is the case for 90° between the external magnetic field and the waveguide) - in case of a perfect alignment, there is no measurable absorption signal is this configuration.

The FMR setup (detailed description of the setup and measurement method see also reference [24]) consists of the following main components (see Fig. 4.1): a coplanar waveguide (gold stripes on insulator) serves as a sample holder and is used to apply the hf-signal with a B-field perpendicular to the waveguide. An external magnetic field is generated by coils, mounted on a rotatable device directly beneath the waveguide. Two hf-signal arms are set up, where in one arm, the hf-signal is transferred through an attenuator and a phaseshifter (reference arm), in the second arm, the signal is led through the waveguide (sample arm). For a measurement, the attenuator and phaseshifter are calibrated thus that the overlapping signals of reference and signal arm interfere destructively (minimizing the signal). When sweeping the external magnetic field, it will eventually hit the resonance field and the amplitude of the signal in the sample arm will change due to resonance between the Lamor frequency of the magnetization in the sample and the frequency of the hf signal. This change in signal will cause a change in interference of the overlapping sample and reference arm that can be detected. The external magnetic field additionally is superimposed with a modulation field with a frequency of 156 Hz to allow lock-in technique and the measured signal is the derivative of the DC signal. Fig. 4.2 shows such a single measurement (AC signal) for the external magnetic field in a given crystal direction. To determine the magnetic anisotropy, such single measurements are conducted with different

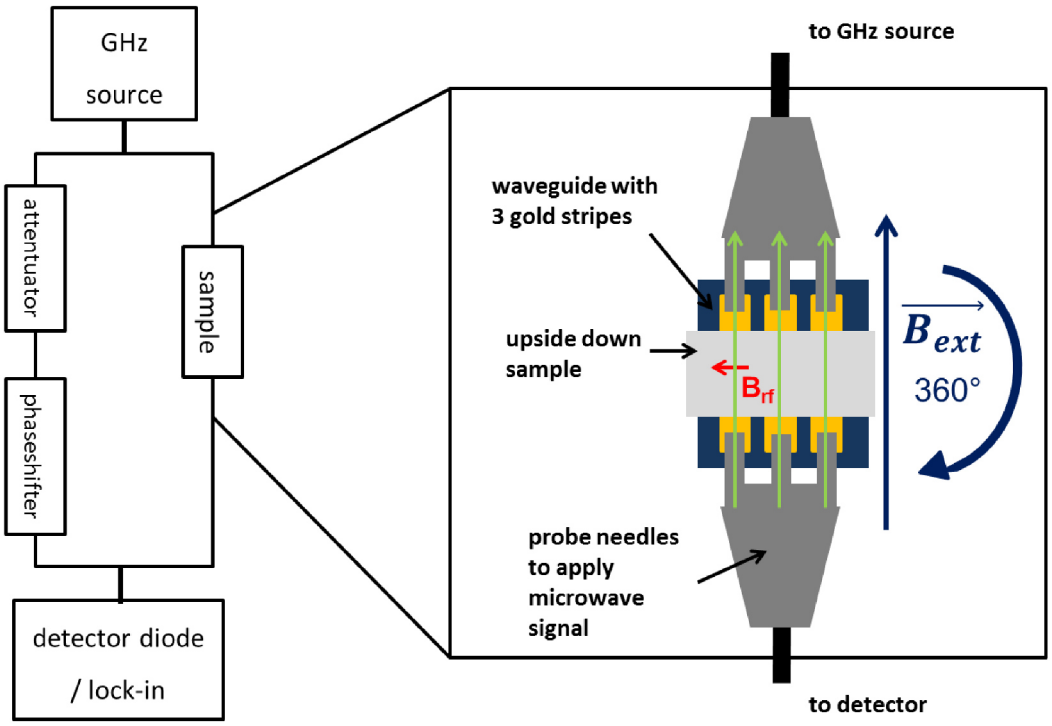

Figure 4.1: Schematics of the FMR setup.

angles between the external magnetic field and the sample, typically every 10° or 20° from 0° to 180° to cover all relevant crystal directions. The sample pieces (usually in the range of 2 mm x 7 mm) were cut from the wafer with their long edge either in one or the other crystal direction. For the 0° configuration, the external magnetic field is thus aligned either along the [110] or [1$\bar{1}$0] crystal direction. For the analysis, the measurements were shifted such that the crystal direction [100] (in the raw measurements either along 45° or 135°) corresponds to the 0°. This has been done since it is easier to align the sample piece in a rectangular configuration to the waveguide than at a 45° angle, to minimize errors coming from misalignment between crystal direction and external magnetic field. Fig 4.3 shows a typical set of FMR measurements - each symbol represents a single absorption signal where the resonance field has been identified as the peak in the DC signal or the interception with zero in the AC signal. A first number that can be extracted from such FMR data is the amplitude, meaning the difference between maximum (hard axis) and minimum (easy axis) resonance field. Here, the amplitude is 140 Oe, however, this kind of analysis is only meaningful for purely uniaxial anisotropy. It is also found that the shape of the data

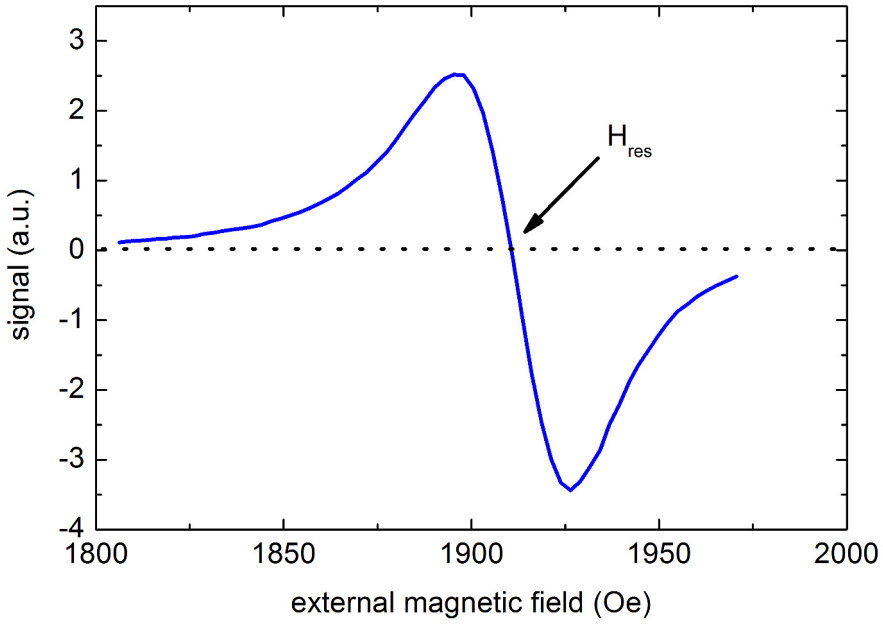

Figure 4.2: Exemplary single FMR measurement.

curve can differ from a pure sine or cosine function (representing pure uniaxial anisotropy), meaning a fourfold anisotropy component can also be present. A fourfold anisotropy exhibits two hard axes along the two crystal directions [110] and $[1\bar{1}0]$ and thus deforms the sine or cosine shape of the uniaxial anisotropy. A quantitative value that can be related to other parameters of the material and also compared with other materials is the uniaxial (fourfold) anisotropy constant $2K_U$ ($2K_1$). In the following section, the model to simulate FMR measurements and extract these material constants used here is presented.

Simulation of FMR data

In references [43] and [24], a model, first described by Kittel [44], to simulate FMR data based on the free energy of the material together with the resonance condition is introduced. Fitting parameters are the anisotropy fields $\frac{2K_U^{\parallel}}{M_S}$ (uniaxial, in-plane) and $\frac{2K_1^{\parallel}}{M_S}$ (fourfold, in-plane) and the angles ϕ_M, ϕ_H, ϕ_F and ϕ_U between crystal direction [100] and the magnetization, external magnetic field, fourfold and uniaxial anisotropy, respectively. Besides that, the out-of-plane anisotropy components are combined in the effective magnetization M_{eff} which is treated as a constant. The derivation of the formula used for this simulation

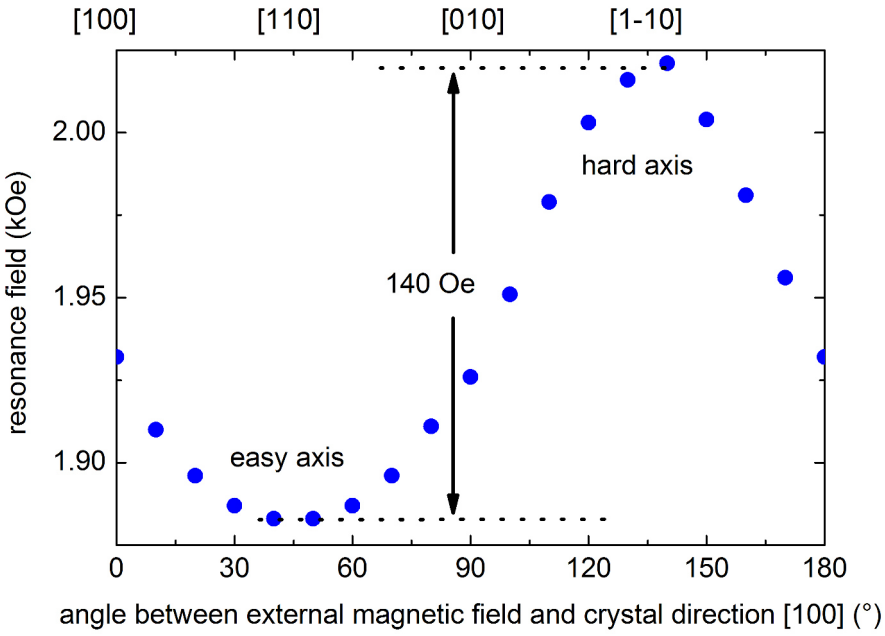

Figure 4.3: Standard FMR measurement (symbols) of the anisotropy. Shown is a uniaxial anisotropy with one easy and one hard axis (along the [110] and [1$\bar{1}$0] crystal direction respectively).

is presented in a condensed way in the following:
First, the free energy equation for thin films of cubic materials is set up. The basic formula is given by:

$$\epsilon_c = -\frac{K_1^{\parallel}}{2}(\alpha_x^4 + \alpha_y^4) - \frac{K_1^{\perp}}{2}\alpha_z^4 - K_u\alpha_z^2 \tag{4.1}$$

where α_x, α_y and α_z describe the magnetization in respect to the crystal directions [100], [010] and [001]. $K_1^{\parallel}$ is the four-fold in-plane anisotropy constant, K_u and $K_1^{\perp}$ represent the perpendicular uniaxial anisotropy (second and fourth order respectively). In the in-plane FMR geometry as it is used here, the fourth order perpendicular anisotropy term $K_1^{\perp}$ can be neglected, instead, an additional uniaxial in-plane anisotropy term is added:

$$\epsilon_u = -K_u^{\parallel}\frac{(\hat{n}\cdot\hat{M})^2}{M_S^2} \tag{4.2}$$

with the unit vector $\hat{n}$ along the uniaxial anisotropy and the saturation magnetization M_S, $\hat{M}$. This uniaxial anisotropy term is actually the most prominent part of the anisotropy in

the here presented NiMnSb samples.
The external magnetic field is taken into account by a Zeeman term, defined as:

$$\epsilon_Z = -\mathbf{M} \cdot \mathbf{H_0}. \tag{4.3}$$

A third additional term is the demagnetization term which is based on an out-of-plane anisotropy component, caused by shape-anisotropy due to the thinness of the layer.

$$\epsilon_{demag} = -\frac{4\pi D M_\perp^2}{2}. \tag{4.4}$$

All the above terms are combined to the total free energy equation:

$$\epsilon_{total} = \epsilon_c + \epsilon_u + \epsilon_Z + \epsilon_{demag}. \tag{4.5}$$

Calculating the partial derivation of this total free energy after the magnetization will result in the effective magnetic field H_{eff}, including the rf-contribution $\vec{h}$:

$$H_{eff} = -\frac{\partial \epsilon_{total}}{\partial \mathbf{M}} + \vec{h} \tag{4.6}$$

The result is then used to solve the Landau Lifshitz Gilbert equation, that describes the time dependency of a magnetization M:

$$-\frac{1}{\gamma}\frac{\partial M}{\partial t} = [M \times H_{eff}] - \frac{G}{\gamma^2 M_S^2}[M \times \frac{\partial M}{\partial t}] \tag{4.7}$$

with the gyromagnetic ratio $\gamma = \frac{g\mu_B}{\hbar}$ and the Gilbert damping constant $G = \frac{\alpha}{\gamma M_S^2}$. The terms with the damping constant G are neglected in the following, considering the very low value for α of order 10^{-3} or lower [24]. Solutions of the LLG equation for the magnetization M, m^{rf} depend on the already above mentioned fitting parameters including angles, anisotropy constants and fields. In the last steps, the susceptibility [44], [45], $\chi = \frac{\partial m^{rf}}{\partial h}$ is calculated and the resonance condition is found by determining the case of susceptibility diverging to infinity (set denominator to zero). For the here considered system, this will lead to:

$$(\frac{\omega}{\gamma})^2 = B_{eff}\mathcal{H}^*_{eff} \tag{4.8}$$

with

$$\mathcal{H}^*_{eff} = H_0 cos[\phi_M - \phi_H] + \frac{2K_1^{\parallel}}{M_S} cos[4(\phi_M - \phi_F)] + \frac{2K_U^{\parallel}}{M_S} cos[2(\phi_M - \phi_U)] \tag{4.9}$$

$$B_{eff} = H_0 cos[\phi_M - \phi_H] + \frac{K_1^{\parallel}}{2M_S}(3 + cos[4(\phi_M - \phi_F)]) \tag{4.10}$$
$$+4\pi D M_S - \frac{2K_U^{\perp}}{M_S} + \frac{K_U^{\parallel}}{M_S}(1 + cos[2(\phi_M - \phi_U]))$$

with the angles ϕ_M, ϕ_H, ϕ_F and ϕ_U of the magnetization, external magnetic field and in-plane easy axis, respectively, in respect to the crystal direction [100]. The angle-independent parts $4\pi D M_S - \frac{2K_U^{\perp}}{M_S}$ are defined to be the effective magnetization $4\pi M_{eff}$ and considered as a constant here. For each crystal direction (angles between 0° and 180°), the resonance condition $(\frac{\omega}{\gamma})^2 = B_{eff}\mathcal{H}^*_{eff}$ is then fulfilled for each angle with a certain resonance field given by the measurement, the used frequency (here usually 12.5 GHz) and a fixed set of the above mentioned fitting parameters, that will then be extracted.
Using this model, the anisotropy of a set of samples with thickness in the range of 40 nm (considered as thick samples) has been analyzed and is presented in the next section. These results are published in reference [46].

4.2 Anisotropy in thick NiMnSb films

For this study, a set of 17 samples with different Mn concentration is selected, applying the following criteria: The thickness of the NiMnSb layers is comparable (here (38 ± 2) nm, two samples are 45 nm thick) and lies in the thick regime, and a non-magnetic capping layer (Ruthenium) is deposited on the sample. Later it will be seen that the capping material can also have influence on the anisotropy, so only samples with equal capping material are compared. Furthermore, the RHEED reconstruction observed during growth of the layers must be either d/2 or d/1, including samples with rotated pattern, to exclude samples where enhanced or reduced Sb or Ni fluxes have been applied. The majority of these samples are grown intentionally for this study within a short period of time that allowed for using the same cell temperatures of Ni and Sb and only change the Mn cell temperature. However, also samples from an earlier growth period were chosen, grown with different absolute cell temperatures, and it is found that they also fit well in the overall picture. Among these samples, the observed anisotropies can be ordered in two different categories: Mainly or purely uniaxial anisotropies, or uniaxial anisotropies superimposed with fourfold anisotropies, where these two types of anisotropy can occur in both main crystal directions [110] and [1$\bar{1}$0]. Fig. 4.4 shows four representative samples exhibiting these four different kinds of anisotropy, together with simulations according to the above

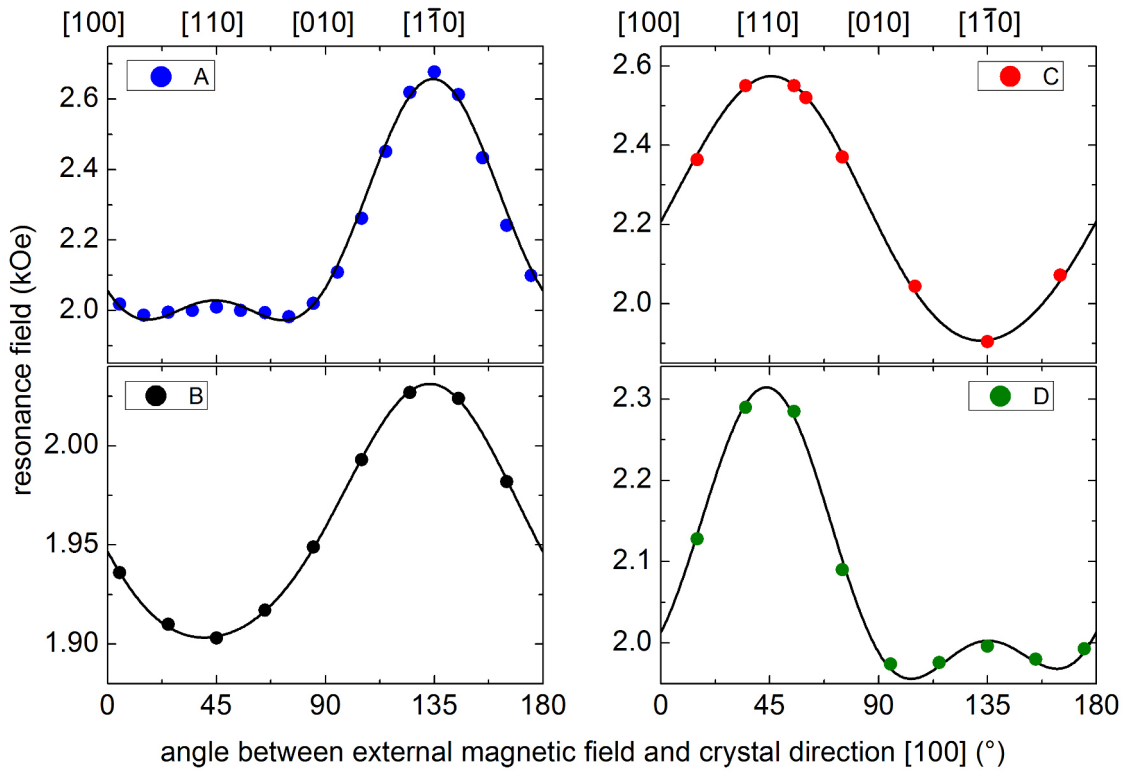

Figure 4.4: Four representative samples exhibiting four different kinds of anisotropy observed in NiMnSb. Sample A, D: uniaxial anisotropies superimposed with a fourfold anisotropy, sample B, C: mainly uniaxial anisotropy.

described model (black lines). Samples A and D show uniaxial anisotropies superimposed with a fourfold anisotropy, samples B and C show mainly uniaxial anisotropy. In case of a fourfold anisotropy, the two main crystal directions [110] and [1$\bar{1}$0] always exhibit the hard axes, whereas in between, shifted by 45°, the easy axes occur. The superimposed uniaxial anisotropy is still characterized by the direction of the easy axis, meaning e.g. in sample A, the easy axis of the uniaxial anisotropy is parallel to the [110] crystal direction.
For all 17 samples of this set, the anisotropy fields $\frac{2K_U^{\parallel}}{M_S}$ (uniaxial in-plane) and $\frac{2K_1^{\parallel}}{M_S}$ (fourfold in-plane) are extracted. A first consideration shows that the anisotropy can be quite different, independent on layer thickness, as shown in Fig. 4.5 - the layer thickness has been determined by HRXRD measurements, coming with an error of ± 1 nm. To be able to relate the anisotropy to the Mn concentration, the vertical lattice constant of each sample

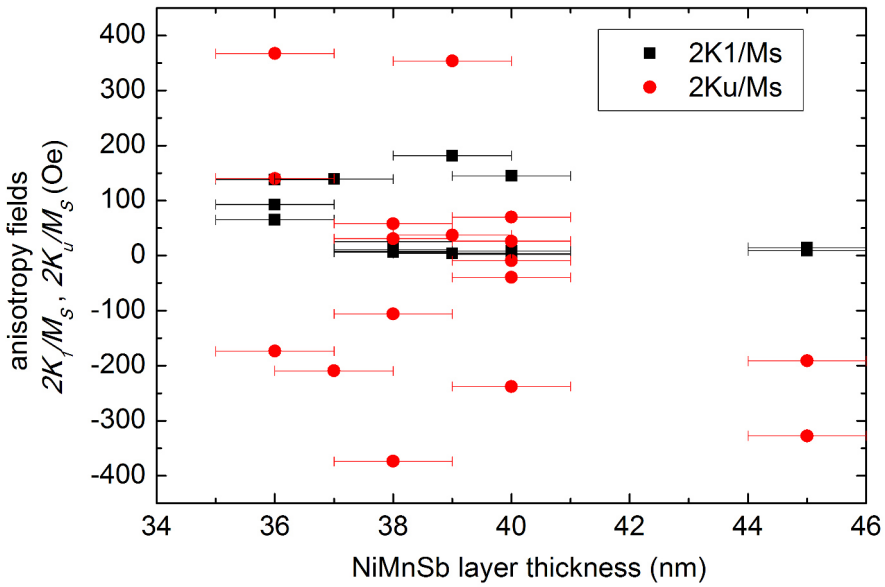

Figure 4.5: Uniaxial and fourfold anisotropy fields versus layer thickness - different anisotropies can be observed for layers of similar thickness.

is determined by HRXRD measurements as well (more details see section 3.1). The error for the vertical lattice constant comes from misreading the exact position of the layer peak in an $\omega - 2\theta$-scan and results in relative errors of well below 1%.

First, the fourfold component of the anisotropy field $\frac{2K_1^{\parallel}}{M_S}$ is plotted versus the vertical lattice constant in Fig. 4.6. The two vertical lines in these graphs mark the range where stoichiometric NiMnSb is expected (based on an estimation of the vertical lattice constant of stoichiometric NiMnSb, see section 3.1) and filled (empty) symbols represent samples with stable (rotated) RHEED pattern respectively. The four samples of Fig. 4.4 are marked with A-D. Considering stoichiometric samples, the fourfold anisotropy field is rather small in the range of 10 Oe or even lower. For samples with decreasing Mn concentration (decreasing vertical lattice constant), $\frac{2K_1^{\parallel}}{M_S}$ increases significantly, where the sample with smallest Mn concentration has a maximum fourfold anisotropy field of 170 Oe. When the Mn concentration is increased, however, the $\frac{2K_1^{\parallel}}{M_S}$ remains fairly small, and increases only to about 25 Oe for the sample with highest Mn concentration. A very interesting fact is that all samples with rotated RHEED pattern (open symbols) exhibit only a comparably small fourfold anisotropy, on the other hand a non-rotated or stable RHEED reconstruction results in a

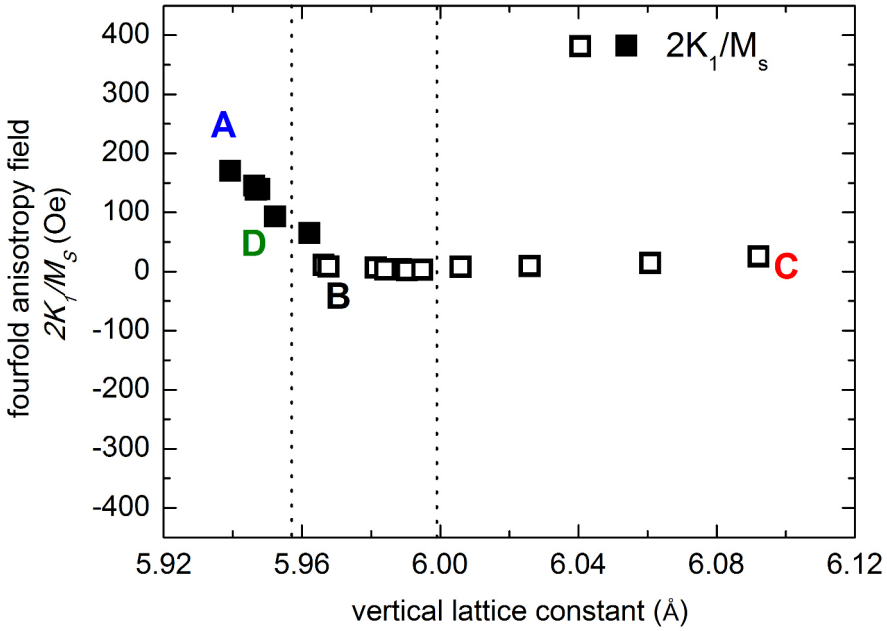

Figure 4.6: Fourfold anisotropy field vs. vertical lattice constant (Mn concentration). Open symbols represent samples with a rotated RHEED pattern, filled symbols represent samples with a stable RHEED pattern.

significant fourfold anisotropy component (filled symbols). This behavior might be related to the fact that the crystal structure is increasingly stretched in the vertical direction with increasing Mn concentration, resulting in a more cuboid unit cell compared to the more cubic unit cell in case of smaller vertical lattice constant.

A similar plot is created for the uniaxial anisotropy field and is presented in Fig. 4.7: For the uniaxial anisotropy field, either positive or negative fields are found, where positive fields mean an easy axis along the [110] crystal direction and negative fields describe an easy axis rotated by 90° to the $[1\bar{1}0]$ direction. First, for an increasing Mn concentration, the uniaxial anisotropy field is clearly increasing towards higher negative values, up to a value of $-374\,\mathrm{Oe}$ for sample C with highest Mn concentration. In the opposite direction, $\frac{2K_U^{\parallel}}{M_S}$ is increasing in absolute value, however the sign and thus crystal direction of the easy axis is no longer stable: The three samples showing negative uniaxial anisotropy fields for a reduced Mn concentration (whereas all other samples in this region exhibit positive $\frac{2K_U^{\parallel}}{M_S}$) seem out of place - at a first glance, the absolute value of those three anisotropy fields would fit perfectly in the overall trend of increasing positive anisotropy fields. Since the

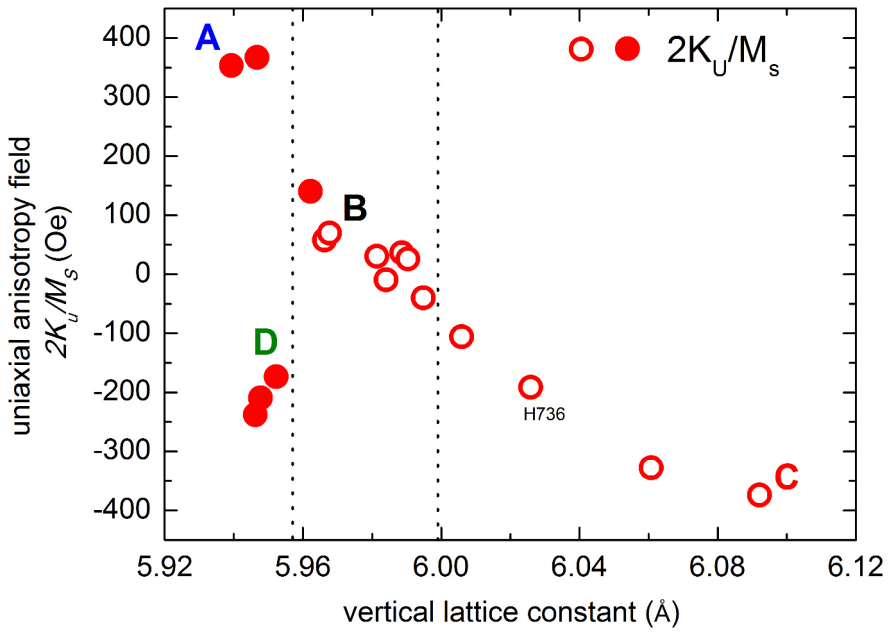

Figure 4.7: Uniaxial anisotropy field vs. vertical lattice constant (Mn concentration). Open symbols represent samples with a rotated RHEED pattern, filled symbols represent samples with a stable RHEED pattern.

sign of these data points has been verified by repeating measurements, an additional parameter must be the reason for this discontinuity. What parameter that would be can only be speculated.

The most important result here can be found in a small range of Mn concentration around the stoichiometric region: At a Mn concentration corresponding to a vertical lattice constant of 5.99 Å, the uniaxial anisotropy field is changing sign, corresponding to a rotation of the easy axis from the [110] to the [1$\bar{1}$0] crystal direction. Here, the RHEED reconstruction does not seem to influence the anisotropy field in a way it has been for the fourfold anisotropy - samples with rotated RHEED reconstruction can have both positive or negative uniaxial anisotropy fields. What cannot be shown in this graph is the growth time and thus thickness at which this rotation of the RHEED pattern has been completed, where this thickness of completed RHEED rotation depends on the absolute Mn concentration. Samples in the stoichiometric region exhibit RHEED rotation that completed at the end of growth and at an already large layer thickness, meaning the majority of the sample has exhibited a non-rotated RHEED pattern. These samples can then show a uniaxial

anisotropy field that is positive. For samples with a significantly larger Mn concentration, the rotation of the RHEED pattern occurs at already smaller layer thicknesses, thus that a significant part of the layer exhibits a rotated RHEED pattern. It is difficult to make a quantitative statement about this, however from experience this behavior can be concluded. Furthermore, even if the range of Mn concentration to reliably achieve a positive uniaxial anisotropy field seems rather small, by adjusting the Mn cell in steps of 1 K, the control of the anisotropy is possible and also reproducible.
So far, the anisotropy fields are discussed - as can be seen from the formula ($\frac{2K_{U,1}}{M_S}$), they are still dependent on the saturation magnetization M_S, which is different from material to material. In NiMnSb, the saturation magnetization is theoretically 4.0 μ_B - but only when assuming stoichiometric material. So when the Mn concentration is changed, the saturation magnetization changes as well, as it is described in reference [39] and sections 3.2, 3.3. For some of the above presented samples, the saturation magnetization is measured by SQUID and plotted vs. the vertical lattice constant in Fig. 4.8: For samples in

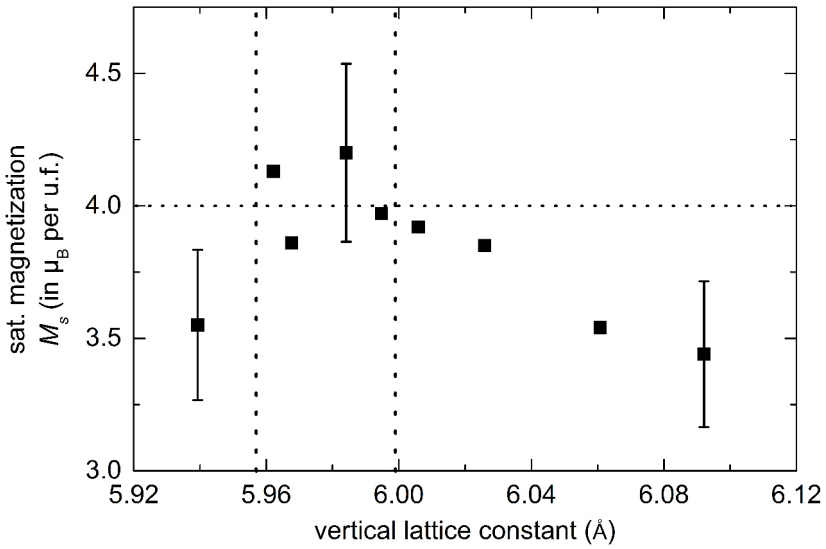

Figure 4.8: Saturation magnetization of stoichiometric and off- stoichiometric NiMnSb.

the stoichiometric regime (marked with vertical dotted lines in the graph), the saturation magnetization agrees well with the expected 4.0 μ_B. When the Mn concentration is either increased or decreased, the saturation magnetization gets smaller. The error bars in Fig.

4.8 mark the estimated error of 8% and account mainly for errors in the measurement of the volume of the sample - the thickness is determined by the period of the thickness oscillations in a HRXRD scan, the area of the sample is measured with a caliper. Scaling the anisotropy field with the saturation magnetization would however not change the overall behavior of the anisotropy, instead an additional error would be introduced, and that is why the anisotropy fields are presented unscaled in the study above.
Another fitting parameter, the effective magnetization $4\pi M_{eff} = 4\pi D M_S - \frac{2K_U^{\perp}}{M_S}$, represents the out-of-plane components of the anisotropy. Fig. 4.9 shows M_{eff} in dependence of the Mn concentration (vertical lattice constant). A decrease for the far off-stoichiomteric sam-

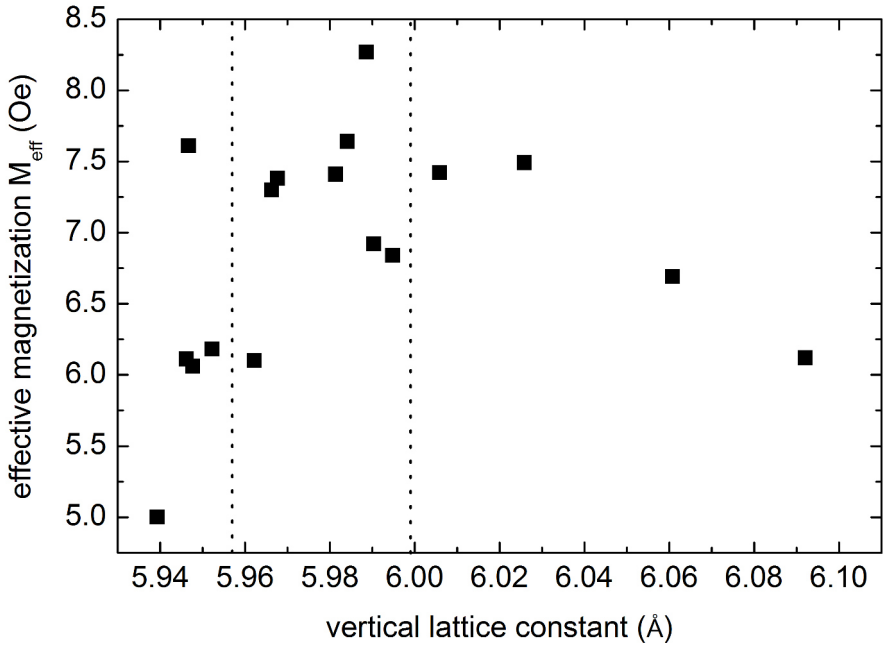

Figure 4.9: Effective magnetization M_{eff} depending on Mn concentration - in the stoichiometric region (vertical dotted lines), a maximum can be seen whereas for far off-stoichiometric samples, M_{eff} decreases.

ples is seen, and in the region of expected stoichiometric NiMnSb M_{eff} exhibits a maximum (within vertical lines in Fig. 4.9). In reference [43], is is reported that the perpendicular, uniaxial interface anisotropy depends strongly on the composition of the interface - this is consistent with the here observed behavior of decreasing M_{eff} for samples with a large deviation from stoichiometry and resulting change in interface composition. Due to the

strongly scattered data points, no quantitative evaluation can be made. Nonetheless, assuming that the perpendicular, uniaxial interface anisotropy $\frac{2K_U^{\perp}}{M_S}$ is positive, an increase with both decreasing and increasing Mn concentration can be concluded.
The behavior of the uniaxial in-plane anisotropy $\frac{2K_U^{\parallel}}{M_S}$, saturation magnetization M_S and also the effective magnetization M_{eff} are further confirmation that the estimated region of stoichiometric NiMnSb is valid, since a certain behavior can be observed in this region: $\frac{2K_U^{\parallel}}{M_S}$ changes sign, M_S exhibits the theoretical expected 4.0 μ_B and M_{eff} exhibits a maximum.

In the here presented results, the unit of the anisotropy fields is Oersted - to be able to compare it with other materials in other reports, where the anisotropy constant is often given in units of $\mathrm{J\,m^{-3}}$ or eV/atom, the conversion will be briefly presented. To do so, the saturation magnetization given in units of μ_B is converted into units of $\frac{J}{T \cdot m^3}$ and is assumed to be 4.0 μ_B:

$$\begin{aligned}
&\text{volume of 1 unit formula (u.f.)} \equiv \frac{(5.926 \cdot 10^{-10})^3}{4} m^3 \\
&\rightarrow 1m^3 \equiv \frac{4}{(5.926 \cdot 10^{-10})^3} u.f. \rightarrow 1m^3 \equiv 1.92 \cdot 10^{28} u.f. \\
&\rightarrow M_S[m^3] = 4.0\mu_B \cdot 1.92 \cdot 10^{28} = 7.1 \cdot 10^5 \frac{J}{T \cdot m^3} \text{ with } \mu_B = 9.27 \cdot 10^{-24} \frac{J}{T} \\
&\rightarrow K_U = \frac{1}{2} \cdot X \cdot 7.1 \cdot 10^5 \frac{J}{T \cdot m^3} = 3.6 \cdot 10^5 \cdot X \frac{J}{T \cdot m^3}
\end{aligned}$$

X is the anisotropy field in units of Tesla - here, ranging from $1 \times 10^{-3}\,\mathrm{T}$ to $1 \times 10^{-2}\,\mathrm{T}$ (corresponding to 10 Oe to 100 Oe). The uniaxial anisotropy constant in NiMnSb can thus be tuned from very low values in the range of $100\,\mathrm{J\,m^{-3}}$ up to values 2 orders of magnitude higher (for an anisotropy field of 300 Oe, the corresponding anisotropy constant would be $10\,800\,\mathrm{J\,m^{-3}}$). In comparison, anisotropy constants for Fe are reported in the range of $10 \times 10^5\,\mathrm{J\,m^{-3}}$ [47], many other materials exhibit values in that range (see e.g. also reference [48] for metallic multilayers) as well. Thus, stoichiometric NiMnSb exhibits a rather weak anisotropy, however with a change of composition it can be tuned up to the range of e.g. Fe.

4.3 Anisotropy in NiMnSb films of other thicknesses

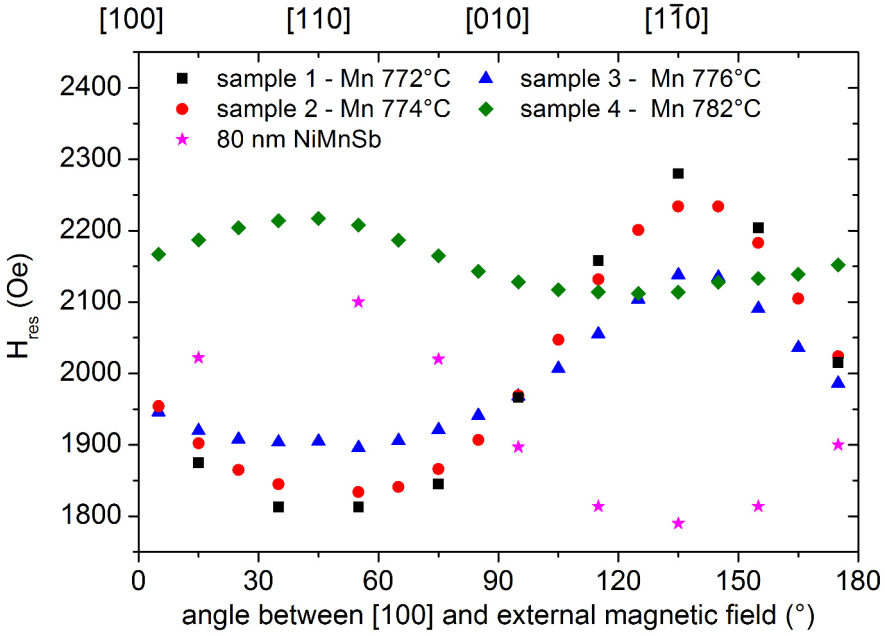

Figure 4.10: Anisotropy in thin films of NiMnSb (10 nm, black, red, blue and green) and very thick films (80 nm, pink stars).

To get a more complete picture of the anisotropy, thin films (of about 10 nm thickness) with different Mn concentration are investigated as well. Fig. 4.10 shows the anisotropy of four such samples where the Mn flux is increased slightly from sample 1 to sample 3 (increase of 2 K Mn cell temperature for each sample) and significantly in sample 4 (increase of 10 K compared to sample 1). Sample 1, with lowest Mn concentration, shows a clear uniaxial anisotropy with the easy axis along the [110] axis - the same behavior as in thick samples with low Mn concentration. When going to higher Mn concentration (sample 2), the amplitude is decreasing, however the easy axis remains in [110] direction. This is also the case even for higher Mn concentration (sample 3), at which a thick sample would exhibit a rotated anisotropy - in terms of Mn concentration, sample 3 can be compared to sample H736, a 40 nm thick NiMnSb film with a vertical lattice constant of 6.025 Å and a significant uniaxial anisotropy with its easy axis along [1$\bar{1}$0] direction, see Fig. 4.7. Only if an extremely high Mn flux is applied (sample 4) and the RHEED reconstruction is rotated almost immediately after growth start, the direction of the anisotropy can be

rotated. Sample 4 is grown with a comparable Mn cell temperature as the sample C with highest Mn concentration in Fig. 4.7.
For this set of samples, a direct relation to the Mn concentration represented by the lattice constant (as for the thick layers) is not possible, since the vertical lattice constant is hard to determine: the peak position, used for calculating the vertical lattice constant comes with a big uncertainty. In the HRXRD measurement of a thin, 10 nm NiMnSb layer, the signal resembles rather a broad shoulder than a distinct peak and an accurate peak maximum is hard to define, see also Fig. 4.11, red curve.

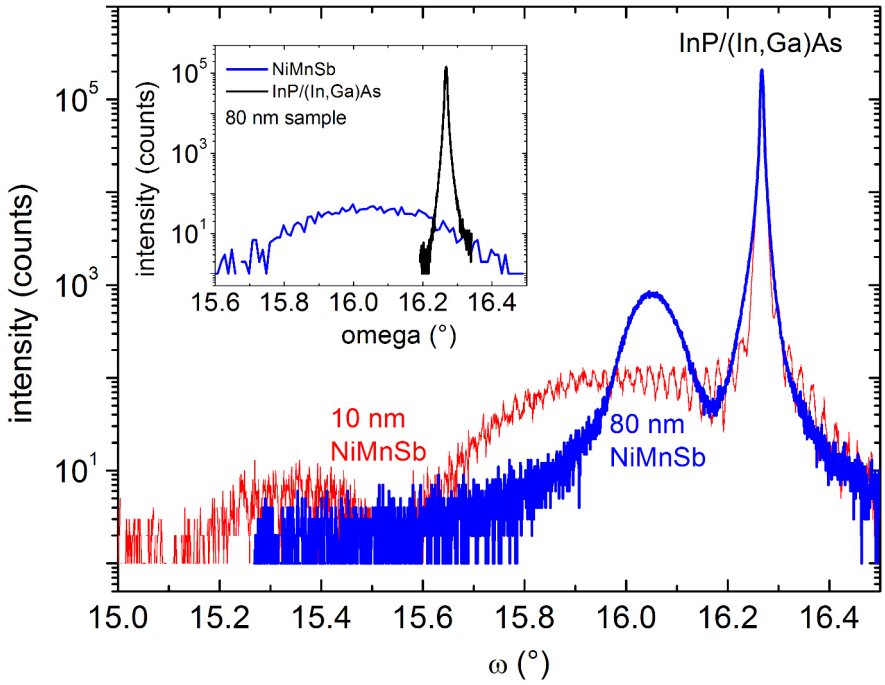

Figure 4.11: HRXRD measurements of the 80 nm and 10 nm NiMnSb layers.

In the opposite direction, going to thicker samples than 40 nm layers, the anisotropy can be rotated as well: For a Mn concentration in the stoichiometric regime, a very thick layer with about 80 nm thickness is grown (see Fig. 4.10, pink stars). Interestingly, the uniaxial anisotropy of that layer is rotated again with the easy axis along the $[1\bar{1}0]$ crystal direction. In Fig. 4.11, the $\omega - 2\theta$-scan of this sample (blue curve) together with the ω-scan of both substrate and NiMnSb layer (inset) are shown. It can be seen clearly that the $\omega - 2\theta$-scan

of this sample shows no thickness fringes, suggesting rather rough interfaces and probable, at least partial, relaxation of the crystal. Furthermore, the ω-scan of the NiMnSb peak is very broad, another sign for relaxation of the layer.

4.4 Influence of capping material on anisotropy

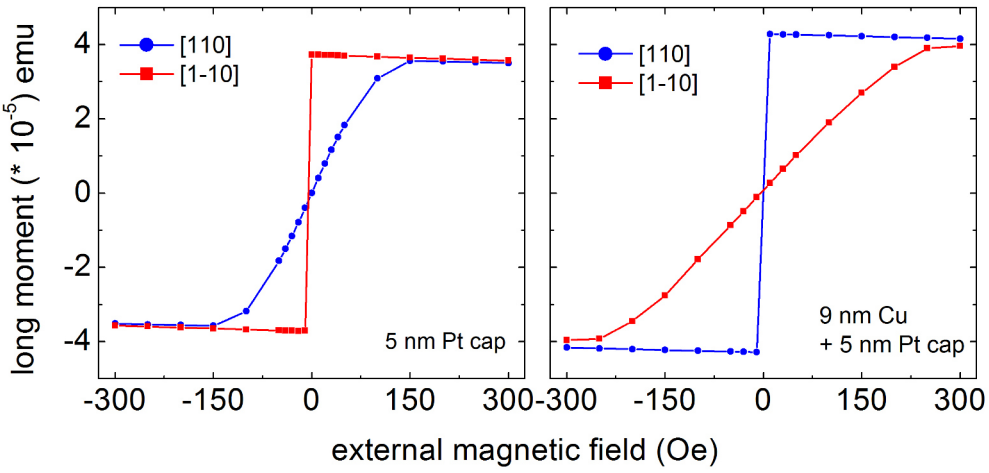

Figure 4.12: SQUID measurements of two 5 nm NiMnSb layers with different capping materials along the [110] direction. For Pt as a cap material, the anisotropy behaves like in case of very large Mn concentration.

In the set of thick samples presented above, the capping material for all samples is Ruthenium, with a thickness in the range of 10 nm. In other samples, e.g. in layer stacks for GMR devices, the material directly on NiMnSb is Copper, whereas insulating materials like ZnTe and MgO are used for other purposes, e.g. for optical investigations (not shown in this thesis) and as tunnel barriers (see next chapter). Including these, throughout all samples, the described picture of the (uniaxial) anisotropy is consistent: samples in a certain range of low or stoichiometric Mn concentration exhibit a "non-rotated anisotropy" with its easy axis along the [110] direction, but an enhancement of the Mn concentration can rotate the anisotropy (amount of Mn concentration to rotate the anisotropy depending on film thickness) and the easy axis is now aligned along the $[1\bar{1}0]$ crystal direction.
However, if Platinum is used as a capping layer, the anisotropy in thin NiMnSb layers of 5 nm thickness is rotated, meaning it exhibits its easy axis along the $[1\bar{1}0]$ direction, even

when the Mn concentration is thus that a thick (40 nm) layer would exhibit a non-rotated anisotropy. To ensure maximum comparability, two sets of samples of 5 nm thickness have been grown literally within one hour (for 2 subsequent samples, all cell temperatures were stable and unchanged), where one sample is capped with Platinum, the other sample is capped with Ruthenium or Copper + Platinum. It is found that the sample capped with Cu+Pt shows a non-rotated anisotropy as expected, whereas the sample capped with Pt exhibits a rotated anisotropy. Fig. 4.12 shows the SQUID hysteresis curves for both crystal direction of two such samples - in the left panel, the NiMnSb is capped with only 5 nm Pt, in the right panel, the capping is a 9 nm Cu layer plus an additional 5 nm Pt cap - the direct contact of Pt with NiMnSb thus influences the anisotropy.

Fig. 4.13 shows the magnetization measured by SQUID along the [110] direction for four

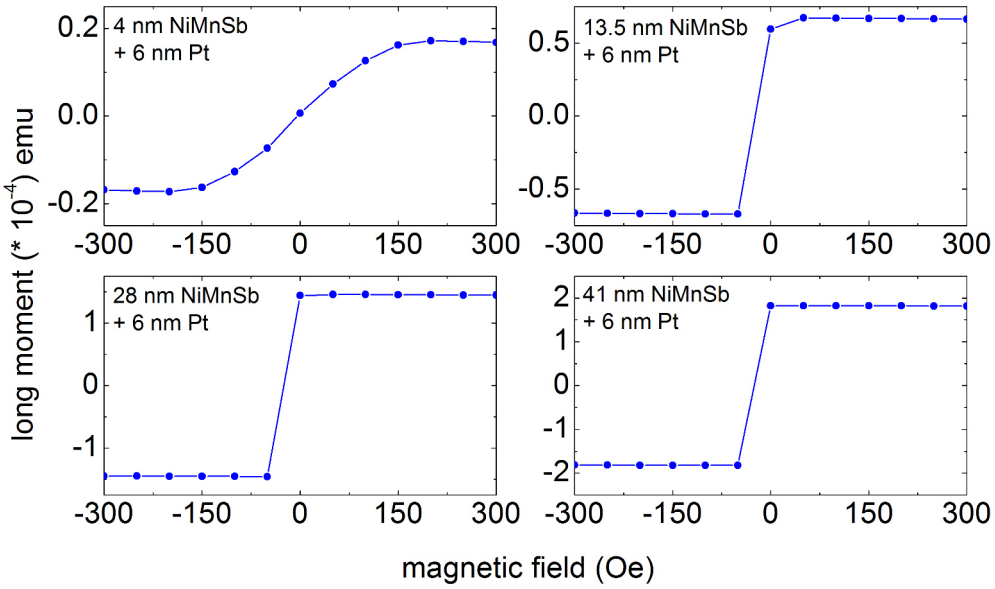

Figure 4.13: SQUID measurements of four samples with different thickness and 5 nm Pt cap measured along [110] crystal direction.

NiMnSb layers of different thickness 4 nm, 13.5 nm, 28 nm and 41 nm, each with a 6 nm Pt cap (nominal thickness). As can be seen clearly, the 4 nm thick layer exhibits a hard axis, where all other layers exhibit an easy axis. The effect of rotated anisotropy in combination with a Pt capping layer seems to occur here only in thin layers. To explore this further, a series of six samples is grown, with nominal thicknesses of 5 nm to 30 nm and a cap of

nominally 5 nm Pt. The hysteresis curves measured along the [1$\bar{1}$0] direction are shown in Fig. 4.14. In this series, all layers exhibit a rotated anisotropy, independent of thickness. In the hysteresis curves of the samples with 10 nm and 30 nm thickness, a feature in the range of −10 Oe to 0 Oe can be seen, indicated by a black arrow. This could be the sign of a second phase in the layer, however the origin is not clear.

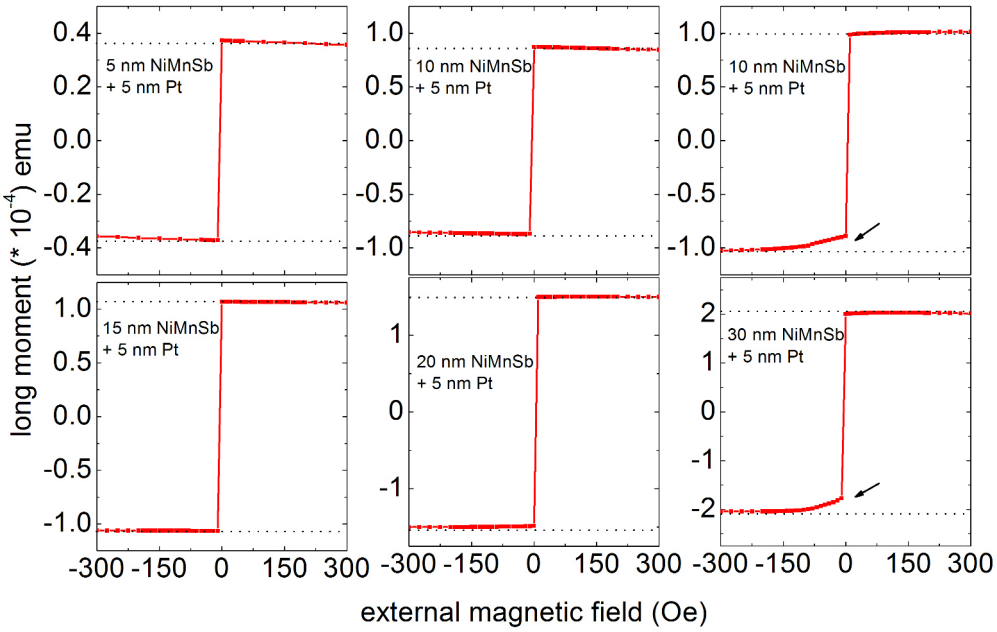

Figure 4.14: A second growth series of NiMnSb layers with different thicknesses and 5 nm Pt cap, hysteresis curves measured along [1$\bar{1}$0] crystal direction.

An interface anisotropy (possible explanation for the change in anisotropy when Pt caps are applied) is the result of two different environments the spins are exposed to (on the one side to bulk, on the other side to the adjacent material, here Pt), and resulting in two different terms of exchange energy. This effect induces an additional term to the anisotropy, the interface anisotropy, which becomes more and more important with decreasing thickness of the bulk part of the sample. Thus, a thickness dependent study should give information on how strong such an interface anisotropy is - quantitatively, this can be evaluated by $K_{eff} = K_V + \frac{2K_S}{t}$ [49], where K_V is the volume anisotropy and K_S the interface or surface anisotropy. Such a thickness dependency has not been observed here.
The problem of a thickness dependent series in NiMnSb is, that with increasing thickness, the Mn concentration has to be considered as well - thus, samples with low and equal Mn

concentration have to be grown to ensure that disregarding the Pt cap, the anisotropy would be "non-rotated". It is possible, that in the series of six samples above, the Mn concentration has changed slightly and thus the thicker layer exhibit a rotated anisotropy due to an increased Mn concentration, independent of the Pt cap.

4.5 Magnetic damping in off-stoichiometric NiMnSb

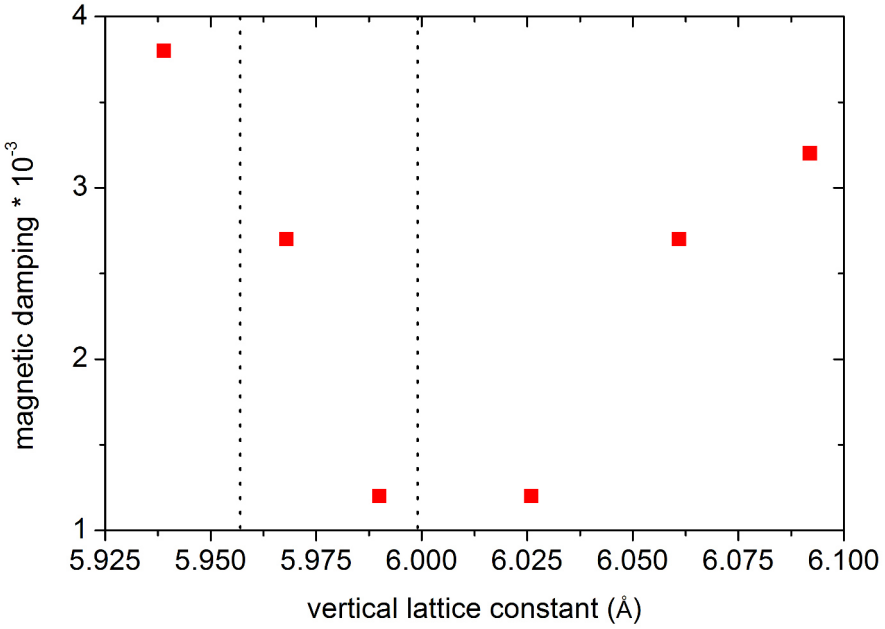

Figure 4.15: Magnetic damping factor α for stoichiometric and off-stoichiometric NiMnSb.

For a subset of the 17 thick off-stoichiometric layers (presented in section 4.2), the damping is measured for the easy axis direction - these measurements were done by P. Dürrenfeld in the group of J. Åkerman at University of Gothenburg, using a PhaseFMR setup by NanOsc AB. Fig. 4.15 shows the magnetic damping (dimensionless factor) α for samples in the low-Mn, stoichiometric and high-Mn regime. For all samples, even in the far off-stoichiometric region, the damping factor is very low, and a minimum damping is found for two samples in the upper stoichiometric regime (marked by vertical dotted lines) and the region with slightly enhanced Mn concentration. This result shows that the low magnetic

damping is preserved in samples with off-stoichiometric composition. From a technological point of view, this is important since it allows to tailor the anisotropy according to the device design and at the same time have a low-damping material.

4.6 Empirical picture of the anisotropy in NiMnSb

The magnetic anisotropy of a ferromagnet can have different origins [50]: The *crystalline (or magnetocrystalline) anisotropy* originates from the spin orbit coupling, where the spins are aligned along a certain crystal direction by their coupling to the electron orbits. Other anisotropy terms are *shape-* or *strain-related*, where external parameters such as shape and dimension or intrinsic parameters such as strain induced by lattice mismatch can effect or even induce additional anisotropy terms. Besides that, interfaces and surfaces can cause additional anisotropy terms - however, the majority of reports on the latter are on out-of-plane anisotropy or very thin layers, whereas in this case, only in-plane anisotropies of comparably thick layers (referring to the study of 17 samples in section 4.2) are investigated.

There are two earlier studies on the magnetic anisotropy in MBE-grown NiMnSb, where the first investigates the dependence on film thickness [42] and the second one studies the effect of externally induced lateral strain on the film [51]. For the study of thickness dependence, the anisotropy of eight samples with thicknesses between 5 nm and 85 nm has been measured. It has been found that both very thin and very thick samples exhibit a significant uniaxial anisotropy. According to Fig. 7 in this report, for thin samples, the uniaxial easy axis is aligned along the $[1\bar{1}0]$ crystal direction (5 nm and 10 nm), for thick samples along [110] crystal direction (42 nm and 85 nm). The result for the thin samples is at first contradicting the results presented in this thesis. However, the saturation magnetization of one of the thicker samples has been measured to be 3.6 μ_B, being significantly smaller than the theoretical expected value or 4.0 μ_B. It suggests that the investigated sample(s) are off-stoichiometric, furthermore some samples of the study are capped with 5 nm Ti, some are not. So it is not clear if this set of samples can be compared with the here presented samples in terms of composition. Nonetheless, a linear dependence on the inverse thickness is reported for the thinnest (5 nm and 10 nm) and the thickest (42 nm and 85 nm) samples, that is then interpreted by the interface between the (In,Ga)As buffer and the NiMnSb layer to be the origin of the uniaxial anisotropy. Furthermore, an in-plane shear strain is suggested to induce an additional uniaxial anisotropy term. The fourfold component has

been found to be increasing for increasing thickness.
In the second study, thin films of NiMnSb (10 nm and 5 nm) have been glued to piezostacks, to control and induce external strain to the sample and investigate the effect on the FMR signal [51]. By a relative change in length of 0.1%, the uniaxial anisotropy could be changed by 20% resulting in a dip of the hard axis - however the anisotropy is in now way rotated as it is the case in the here presented study.
As a summary, the origin of the uniaxial anisotropy is assumed to be the interface between the (In,Ga)As buffer and the NiMnSb layer and thus exhibits a thickness dependent behavior. Besides that, external strain was found to influence the anisotropy, however only weakly. From the results presented here above, a dependence on composition, and - depending on the degree of off-stoichiometry - also on thickness, is concluded. In the following, an attempt for an empirical picture for the anisotropy is made:
An approach to evaluate the strain (and related strain anisotropy) and possible relaxation in the off-stoichiometric samples presented here is made by calculating the critical thickness at which relaxation can occur [52]:

$$t_{crit} = \frac{b * (1 - \frac{\nu}{4})}{4 * \pi * (1 + \nu) * \frac{\Delta a}{a}} \ln \frac{t_{crit}}{b} + 1 \tag{4.11}$$

Here, b is the burger's vector $\sqrt{2}a_{rel}/2$, ν the estimated Poisson ratio of 0.3, $\Delta a/a$ the lattice mismatch. The first term in equation 4.11 is summarized as the constant C. Then, equation 4.11 can be written as:

$$b = \frac{t_{crit}}{exp\frac{t_{crit}}{C}} - 1 = \frac{\sqrt{2}a_{rel}}{2} \tag{4.12}$$

Setting values for t_{crit} in steps of 1 Å, a numerical solution can be found, where t_{crit} is thus that equation 4.12 holds. For the samples in Fig. 4.7 (samples of 38 nm and 45 nm thickness), this critical thickness has been determined and is plotted versus the vertical lattice constant in Fig. 4.16. Consequently, the thickness at which strain occurs decreases with increasing Mn concentration and resulting increasing lattice mismatch.
It is found that samples with a critical thickness of 6 nm and smaller, meaning that 32 or more out of 38 nm layer are possibly relaxed, exhibit a rotated anisotropy. This critical thickness (which is in the range of stoichiometric NiMnSb), seems rather small; the HRXRD scans contradict this, it is hard to believe that the majority of the crystal is relaxed. It has to be noted though that the above given formula was derived originally for pure zincblende

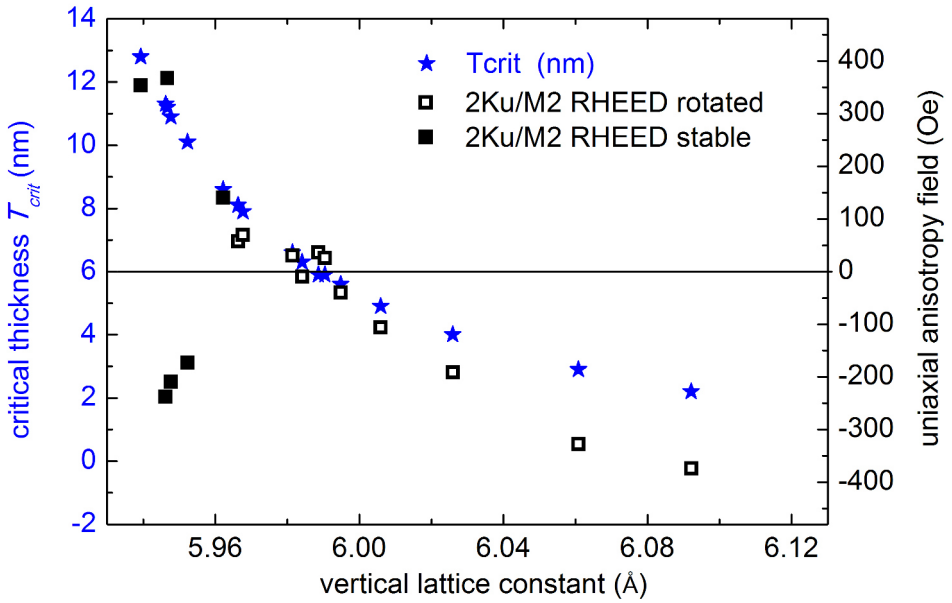

Figure 4.16: Critical thickness versus vertical lattice constant, together with uniaxial anisotropy - when the uniaxial anisotropy is minimal and crossing zero, the critical thickness is in the range of 6 nm.

lattices - however in the case of NiMnSb the structure is a combination of two such lattices, where one zincblende sublattice has a vacancy position. As it will be seen later (chapter 5), for ZnTe - being a pure zincblende - this estimation works quite well.
Nonetheless, it is interesting to see that the curvature of the critical thickness plotted versus the vertical lattice constant is similar to the curvature of the anisotropy fields - both are monotonic (at least in some range) and non-linear - even if the absolute numbers are only a rough estimate.
A second hint on possible origin of the anisotropy comes from the RHEED observation - a rotation by 90° has been observed for increased Mn concentration, where the thickness at which the pattern has rotated completed, depends on the amount of Mn surplus. This rotation could be the result of a complete rotation of the lattice by 90°, meaning a strong shear strain (shear strain origins from the different strain relaxation for different crystal orientation). An excess of Mn atoms in the crystal might be a cause for so-called antiphaseboundary defects (see Fig. 4.17), where the Mn-Sb sublattice (black and black-white striped atoms) is rotated by 90° compared to the sublattice in the previous lattice

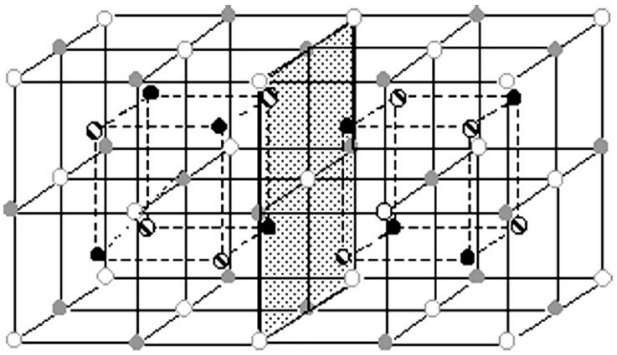

Figure 4.17: Antiphaseboundary defect - the Sb-Mn sublattice (black and black-white striped atoms) is rotated by 90° compared to the previous lattice plane. (picture taken from [27])

plane (picture taken from [27]). It has been shown that such strain can induce a uniaxial anisotropy component [53], [54] and was also assumed to be an origin of the anisotropy in reference [42] (study of thickness dependent anisotropy in NiMnSb).
Such strain-induced anisotropies can explain the here observed behavior like follows: there are two competing anisotropy terms, one coming from the original, bulk magnetocrystalline anisotropy and one originated by strain. However, the type of strain (relaxation, shear strain, ...) cannot be defined explicitly. The strain anisotropy term can win over the original anisotropy in NiMnSb by either an artificially enhanced defect density by either reducing or enhancing the Mn concentration compared to what stoichiometric NiMnSb would be, or by increasing the film thickness above the critical thickness of relaxation (compare the 80 nm layer described above). The superimposition of both anisotropy terms is then what is measured in FMR.
A change of the spin orbit coupling due to crystal defects (Mn_{Ni}) and thus a change in magnetocrystalline anisotropy seems unlikely, due to the different behavior of thin, off-stoichiometric samples compared to thicker layers: In such thin layers, a lot more Mn has to be added to rotate the anisotropy - assuming the defects to occur already at growth start, the thickness of the sample with a certain Mn concentration should not influence the anisotropy.

4.7 Anisotropy in NiMnSb - summary

The magnetic anisotropy in NiMnSb can be tuned by a small change in composition, both strength and orientation can be controlled, where at the same time the very low magnetic damping is preserved! Fig 4.18 summarizes the results of the magnetic in-plane uniaxial

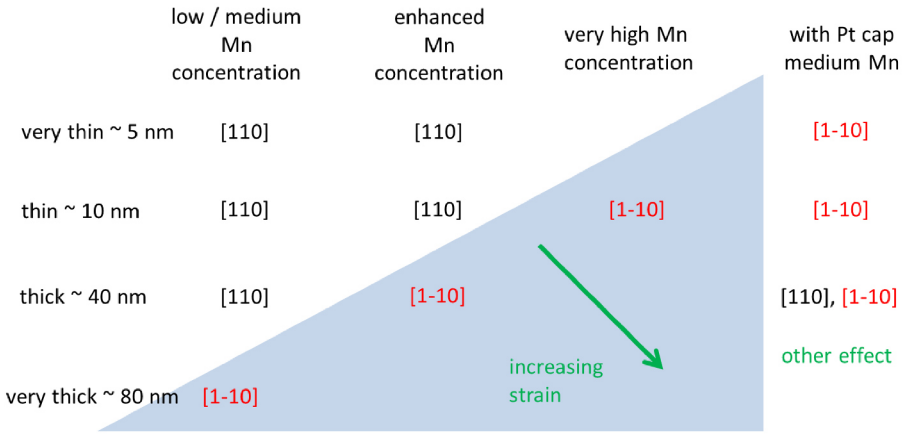

Figure 4.18: Summary of the magnetic in-plane anisotropy in NiMnSb - crystal directions for the uniaxial easy axis are given.

anisotropy in NiMnSb for changing Mn concentration and thicknesses, with the exception of Platinum as a capping material: For medium (stoichiometric) Mn concentration, the anisotropy in thin and thick layers is uniaxial with the easy axis along the [110] direction. Going to very high thicknesses (exceeding the range of standard layer thicknesses, meaning 80 nm), the uniaxial easy axis rotates and is found in the $[1\bar{1}0]$ crystal direction. For samples with an enhanced Mn concentration, thin layers exhibit the same basic uniaxial anisotropy as samples with lower or medium Mn concentration. However, thick layers (about 30 nm to 40 nm layer thickness) show a rotated anisotropy, where now the easy axis is found along the $[1\bar{1}0]$ crystal direction. To rotate the anisotropy in thin layers (10 nm range), an extremely high Mn concentration is needed. The former behavior of thickness dependency fits into this bigger picture in a way that the anisotropy indeed depends on layer thickness, however differently for different Mn concentration.
Besides this, the anisotropy can also be changed by the interaction between the cap layer and the NiMnSb layer. Where on the one hand, capping materials such as Ruthenium, Cu and also insulating caps such as ZnTe and MgO are not effecting the above described picture of the anisotropy, a Platinum cap can change it and the resulting total uniaxial

anisotropy has its easy axis along the $[1\bar{1}0]$ direction.
The former picture of thickness dependent anisotropy has been extended and is included in a wider picture including layer composition. Using these results, samples for devices with specific designs of anisotropy can be grown. Very low Mn concentration (below stoichiometric regime) however is not recommended to be used since here the uniaxial anisotropy can occur in either [110] or $[1\bar{1}0]$ crystal direction in a certain range. Furthermore the crystal quality suffers as suggested by more blurry RHEED patterns. Within a small range of stoichiometric and enhanced Mn concentration, the anisotropy can be tuned and rotated reliably. Thus, for two layers with mutually orthogonal easy axes, a medium and a high Mn concentration should be applied.

Chapter 5

NiMnSb - ZnTe - NiMnSb heterostructures as a basis for spin torque oscillators

This chapter describes the application of the above presented investigations on magnetic properties in NiMnSb based magnetic tunneling junctions as a basis for spin torque oscillators. First, the theory of spin transfer torque is presented shortly, together with resulting main requirements on potential materials for spin torque oscillator devices. In the second part of the chapter, the design of magnetic tunneling junctions (MTJs) based on NiMnSb is described, where especially the growth process for such heterostructures is presented. The last section will show structural and magnetic characterization by HRXRD and SQUID of such MTJs.

5.1 Spin Torque Oscillator

Spin Transfer Torque - STT

In the following, the theory of spin transfer torque will be described shortly (a detailed explanation can be found e.g. in reference [55]). Spin transfer torques are originated in the interplay between the spin polarization of a current and the magnetization, where the electrons can exert a torque on the magnetization vector: A simple cartoon model can be made, imagining two ferromagnets separated by a conducting, non-magnetic spacer

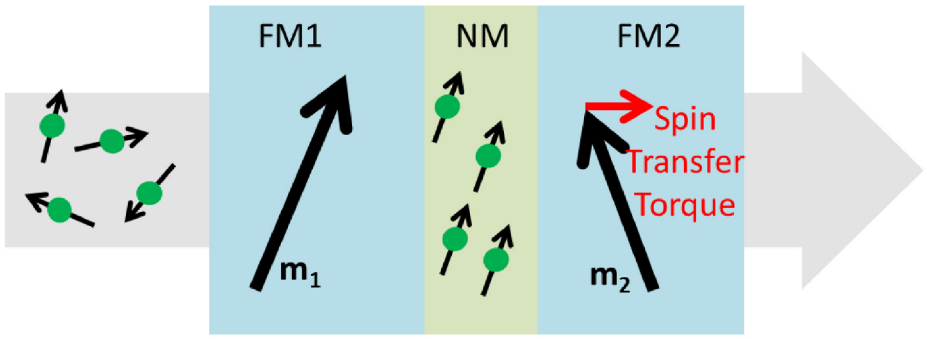

Figure 5.1: Cartoon model for the concept of Spin Transfer Torque.

layer, see Fig. 5.1. Electrons flowing through the first ferromagnet (FM1) will be spin polarized and aligned to the magnetization m_1. These electrons, now carrying a spin angular momentum, reach the second ferromagnet (FM2), in which the magnetization m_2 is aligned differently compared to FM1. The magnetization vector in FM2 now tries to orient the spins of the electrons to itself, exerting an angular momentum on them - and due to the conservation of momentum, the electrons exert an identical, reversed angular momentum on the magnetization. This time dependent change in angular momentum is then called *spin transfer torque* (STT). The interaction between magnetization and spin polarized current can also be described by a form of filtering: at an interface, part of the spin polarized current will be transmitted, part will be reflected. For the case of equal transmission and reflection for both spin directions ($t_\uparrow = t_\downarrow$ and $r_\uparrow = r_\downarrow$), there is no spin filtering, and no net spin current, resulting in zero STT. This corresponds to the case where both ferromagnets are collinear and the spin polarized electrons coming from FM1 exert no angular momentum on FM2. For all other cases, there is spin filtering of some sort (when the transmission and/or reflection of the electrons is spin dependent), resulting in a net spin current, that corresponds to the spin transfer torque. This spin transfer torque is maximal for two mutually orthogonal magnetizations [56].

Spin Torque Oscillators

Functionality

A basic spin torque oscillator (STO) consists of two ferromagnetic layers (FM1 and FM2), separated by a thin spacer layer - a spin valve. The current will flow perpendicular to the ferromagnets' film planes, is spin polarized by FM1 and the spins are aligned to the

magnetization in FM1. In FM2, these spin polarized electrons will exert a spin transfer torque (current induced) on the magnetization m_2 - the current can be adjusted thus that the magnetization m_2 starts to oscillate. Subsequently, the mutual orientation of the two magnetizations m_1 and m_2 is changing periodically. In an overly simplified picture, one magnetization (polarizer, or fixed layer) remains stable whereas the other magnetization undergoes oscillations (free layer). In reality, the magnetic anisotropy of the two ferromagnets together with the current density determines the actual trajectories of the magnetizations which can be quite complex [55].
Depending on the mutual configuration of the magnetizations of two ferromagnetic layers in a spin valve, the resistance over such a device changes (GMR effect [57], [58] for conducting barrier, TMR effect for insulating barrier [59]). This fluctuating resistance at a constant current results in a fluctuating voltage and electric field, which is a generator of electromagnetic waves - the spin valve then acts as a spin torque oscillator (STO).

Materials and design

The required spin torque to start oscillations correlates to the applied current density - thus, first of all the magnetic damping of the used ferromagnets plays an important role. MBE grown NiMnSb turns out to exhibit a very small damping factor in the low 10^{-3} range and is thus a most attractive material for application in such devices. Low required current densities are favorable from a more practical point of view: Too high currents in too small devices can cause material breakdown due to overheating. Besides that, a high spin polarization is desirable to achieve high MR ratio and thus increase the efficiency of a device - again, NiMnSb with a 100% spin polarization in bulk and 60% at the surface is a most promising candidate.
The step from all conducting spin valves towards magnetic tunneling junctions (MTJs) increases the MR ratio significantly. By choosing special barrier materials, the MR ratio can exceed well above 100% (e.g. MgO, [60], [61]). In reference [62], MTJs based on one NiMnSb layer with Aluminumoxide as a tunnel barrier and CoFe as the second FM are presented and MR ratio in the range o 10 % percent is reported. An MTJ based on only NiMnSb is thus an interesting option for the basis of an STO. Such an attempt has been made [14], [13], however the top NiMnSb layer has been capped with Fe, making it a non-all-NiMnSb based approach.
In the following, the growth of NiMnSb-ZnTe-NiMnSb heterostructures is described. The

main challenge in this process is to grow an epitaxial barrier that exhibits high resistance or ideally insulating character, and additionally allows to preserve the high crystalline quality of the NiMnSb grown on top of it. ZnTe is chosen as the barrier material due to it's wide bandgap of 2.2 eV and it's well-known MBE growth process that can be applied at temperatures below 300 °C (being crucial to avoid damage of the InP substrate). A drawback is the lattice mismatch of 3% between ZnTe and NiMnSb, causing massive strain and limiting the thickness of pseudomorphic layers.

5.2 Growth of MTJs based on NiMnSb and ZnTe

In reference [27], a first growth process for NiMnSb - ZnTe - NiMnSb heterostructures is described. There, a few monolayers of ZnTe were grown by MEE (migration enhanced epitaxy) and then a standard MBE growth was used for the remaining ZnTe. For the here presented samples, the entire ZnTe layer is grown by an ALE process which is similar to the MEE process, and has been optimized.
First of all, the bottom NiMnSb layer is grown with the standard process onto the (In,Ga)As buffer layer on the InP substrate. In order to achieve a mutually orthogonal magnetic configuration, this bottom layer is grown with an enhanced Mn concentration, and a thickness of 30 nm (in most cases, but also other thicknesses have been explored), resulting in a strong uniaxial anisotropy with its easy axis along the $[1\bar{1}0]$ crystal direction. Curiously, such layers with rotated RHEED pattern have turned out to be most suitable for the growth of ZnTe, compared to NiMnSb layers with non-rotated RHEED patterns. The process of the ZnTe growth is described in the following section:

ALE process for the growth of ZnTe on NiMnSb

Two main problems have to be addressed when growing ZnTe on NiMnSb: The first is the large lattice mismatch of about 3% between NiMnSb (5.92 Å) and ZnTe (6.10 Å). With the formula to estimate critical thicknesses already given above (equation 4.11, [52]) the critical thickness for ZnTe on NiMnSb is estimated to about one nanometer (see equation 4.11 in section 4.6 using the the lattice mismatch $\frac{\Delta a}{a} = 0.030$.)
For the growth of ultra thin films in the range of very few nanometers, a so-called Atomic Layer Epitaxy (ALE) process is beneficial: In contrast to the standard MBE process, here the wafer surface is exposed to only one element at a time, meaning the cell shutters are

opened subsequently for several seconds. In one period (Zn and Te shutter have each been opened once) ideally one monolayer (ML) grows. Fig. 5.2 shows a schematic of such an ALE process. The second main issue is that group VI elements (Te, Se, ...) react strongly

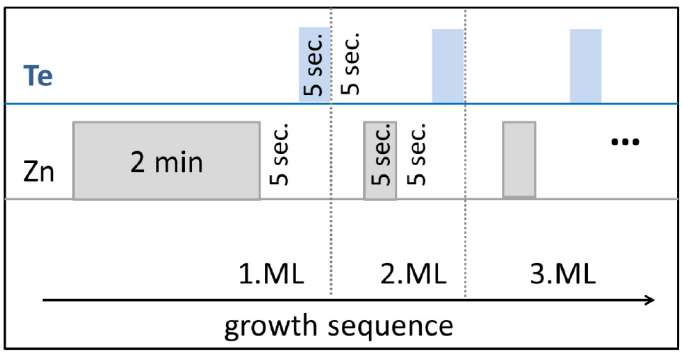

Figure 5.2: ALE process schematics.

with NiMnSb. Thus, in the growth process, the NiMnSb surface should be exposed to as little Te as possible. To achieve that, a Zn-rich atmosphere is prepared in the chamber (opening only Zn for about 5 min to 10 min) before the NiMnSb layer is transferred into it. After the transfer, when the growth temperature of 280 °C is stabilized, the sample is again exposed to only Zn for 2 min to 3 min before the actual ALE process is started with opening of the Te shutter for the first time.
While optimizing this process, it has been found that only NiMnSb layers grown with enhanced Mn flux are inert towards the Zn flushing at the beginning. The RHEED pattern does not change and stays streaky with a clear specular spot (Fig. 5.3, upper panel shows the d/1 and d/2 reconstruction of the rotated NiMnSb surface. In the middle panel, left, the unchanged NiMnSb surface exposed to Zn at 280 °C is shown.) In the other case when the NiMnSb layer has been grown with medium or low Mn flux and exhibits a non-rotated RHEED pattern, the surface changes into d/1 patterns in both crystal directions and gets blurry even before the actual ALE process has started. This is also the case when other surface reconstructions are present (d/3, d/5), meaning in case of lower or increased Ni or Sb flux. The actual growth starts when the Te shutter has been opened for the first time: The RHEED pattern then changes into a clear pattern with a d/1 reconstruction in both crystal directions. About 4 - 5 cycles of ZnTe can be grown smoothly, before the surface roughness increases. Fig. 5.3, middle panel, right, shows the RHEED pattern for 4 MLs of ZnTe (corresponding to 4 cycles of the ALE process) while cooling down from growth

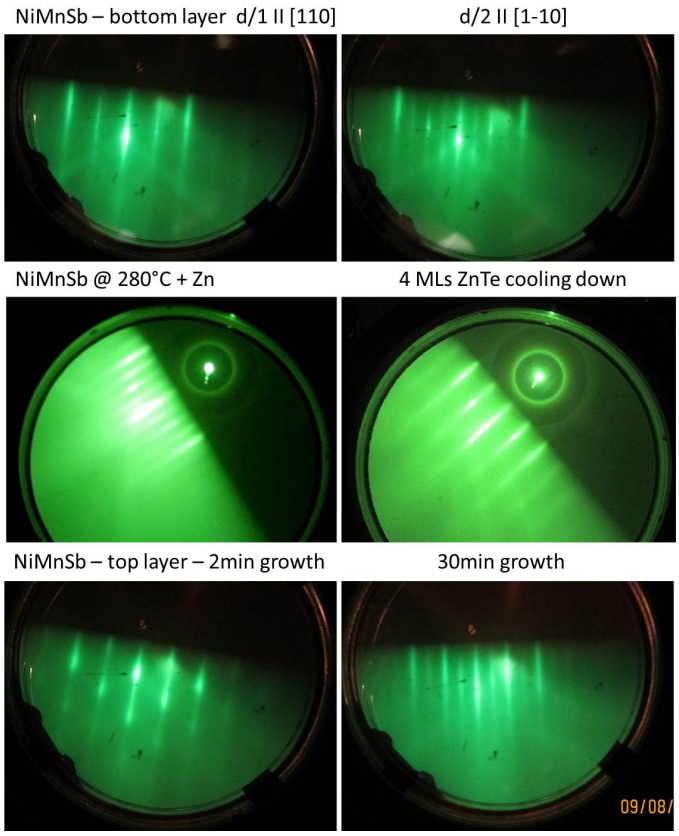

Figure 5.3: RHEED patterns observed during growth of NiMnSb - ZnTe - NiMnSb heterostructures.

temperature. Nominally, these 4 cycles result in a ZnTe layer of 1.2 nm (assuming that one cycle forms one monolayer with thickness of 3.05 Å). The exact thickness cannot be determined easily, nonetheless in HRXRD measurements (presented in the next section), additional features are present, and according simulation of the HRXRD scans confirm the existence of the layer and also roughly the thickness.
The following modifications of the ALE process have been tested for optimization: First, the opening time of the shutters have been varied, however within the tested range of a few seconds, no particular change was observed. Since the very early stages of growth are crucial (surface roughness occurs immediately when the NiMnSb surface is exposed to Te), the opening time of the Te shutter has been reduced for the first two cycles (now 2 s), wheres the opening time of Zn has remained unchanged (5 s). Deduced from observation of the RHEED pattern, with this modification more cycles could be grown before the RHEED

pattern exhibited features of significant surface roughness - however, with the reduced opening time of Te, the first two monolayers probably are not complete monolayers, and the total thickness of the layer remains the same, even with a higher number of cycles. Since the interface of the bottom NiMnSb and the ZnTe is obviously very crucial, the interface between the ZnTe and the top NiMnSb is as well. Thus, to ensure as little contact between Te and the following NiMnSb layer, the samples are exposed to only Zn for 1 min as a last step of the ALE process.

Growth of NiMnSb on ZnTe

The top NiMnSb layer is grown with the same process as the bottom layer, now with reduced Mn flux. After the sample is transferred back into the NiMnSb chamber, it is heated up to the standard growth temperature of 250 °C. The RHEED pattern of the ZnTe layer can be observed and remains unchanged. As soon as the Ni, Mn and Sb shutters are opened for growth, the surface roughens, indicated by the stationary under rotation dots in the RHEED patterns, see Fig. 5.3, lower panel, left. However, the surface flattens again after 5 min to 10 min of growth, corresponding to a few nanometers of thickness. In the end a smooth 2D RHEED pattern with d/2 reconstruction in both crystal directions is observed (see Fig. 5.3, lower panel, right).

With the above described processes, a variety of different MTJs have been grown: standard thickness of the bottom NiMnSb layer is 30 nm, with an enhanced Mn concentration. This thickness was chosen, considering possible lithography processes for the fabrication of actual STO devices - for such devices, the bottom NiMnSb layer has to be contacted electrically, and etching processes have to be developed where the etching stops within this layer. Thus, that layer should not be too thin. On the other hand, for the growth of the ZnTe, a thinner layer would be beneficial, since structures with high lattice mismatch like it is the case here, can be grown with larger thicknesses when the underlying layer is thinner. Besides that, a NiMnSb thickness in the range of 30 nm ensures a good control of the magnetic anisotropy, being another important factor. As for the ZnTe barrier, different thicknesses have been explored: Up to 10 cycles could be grown without a significant surface roughening, corresponding to about 3 nm thickness. Few samples with larger thickness have been grown, where 15 was the maximum number of cycles. Such thick ZnTe layers exhibit significant surface roughness and the subsequent NiMnSb layer exhibits surface roughness

up to larger thicknesses as well. The thickness of the top NiMnSb has been modified as well in the range of 5 nm up to 30 nm. The corresponding switching events observed in SQUID measurements (see section 5.4) scale with the thicknesses of the NiMnSb layers, confirming that also the top NiMnSb layer grows with reasonable crystal and magnetic quality. The detailed characterization is described in the next sections.

5.3 HRXRD measurements of NiMnSb-ZnTe-NiMnSb heterostructures

HRXRD measurements on NiMnSb-ZnTe-NiMnSb heterostructures are done to get information about the crystal structure and quality. Fig. 5.4 shows the standard $\omega - 2\theta$-scan of a NiMnSb-ZnTe-NiMnSb stack (blue, sample H684 described also in the following magnetic characterization) in comparison with a 45 nm single layer (black). Both the main

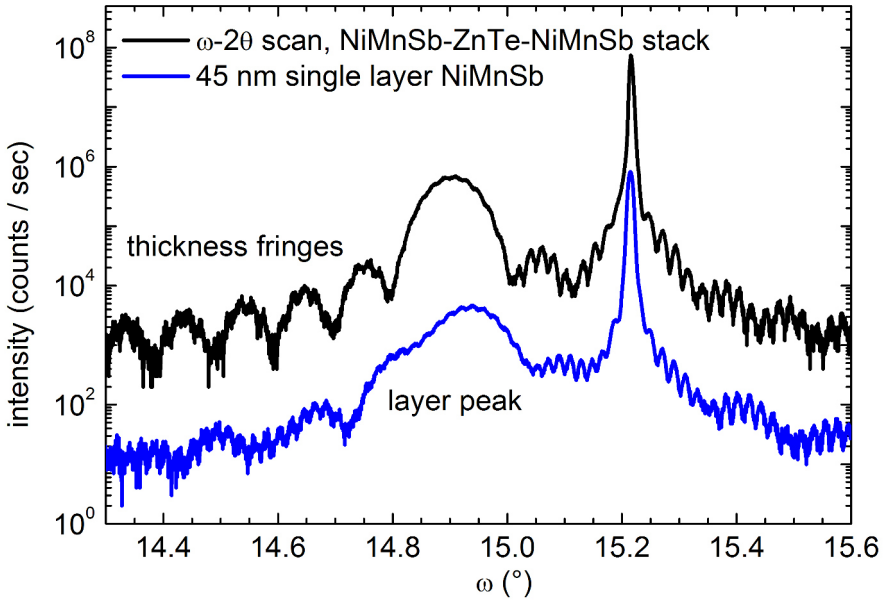

Figure 5.4: HRXRD measurement on a NiMnSb-ZnTe-NiMnSb stack in comparison with a 45 nm single layer.

layer peak of the NiMnSb-ZnTe-NiMnSb stack and the thickness oscillations are clearly deformed, compared to those from a single layer. One reason for the deformation of the

layer peak could be broadening by some sort of relaxation. To rule this out, ω-scans have been conducted at three different positions of the layer peak. The results are shown in Fig. 5.5: All three scans show very narrow FWHM, contradicting the assumption that the layer peak is broadened due to relaxation. It was thus concluded that the additional node(s) origin from the interference of the X-Rays at the additional interfaces NiMnSb-ZnTe and ZnTe-NiMnSb. To further confirm the existence of two spatially separated NiMnSb layers,

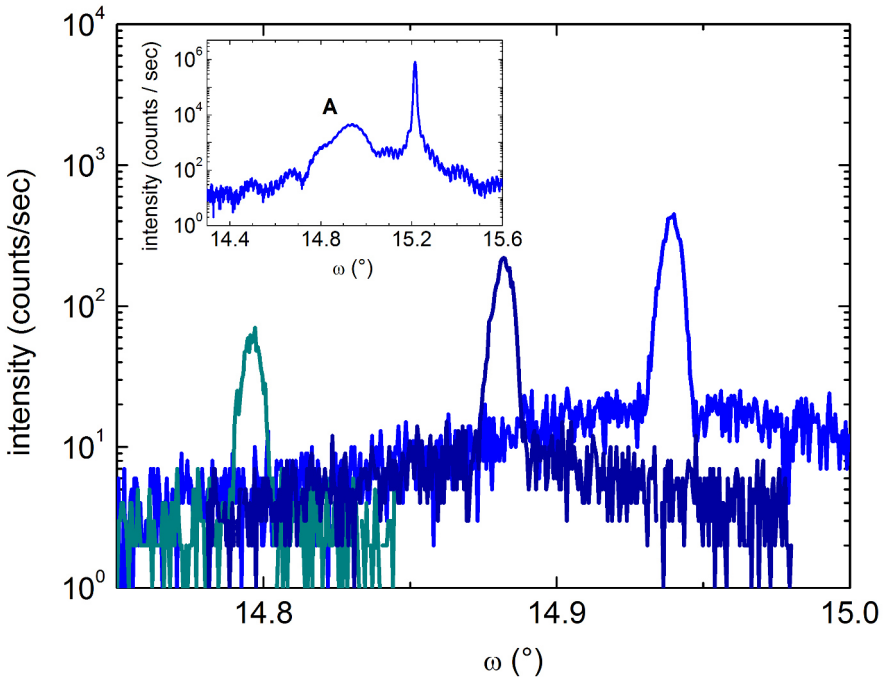

Figure 5.5: ω scans of peak A, confirming broadening by additional layers in the stack.

a simulation of the nominal layer stack is done by *DISCUS* ([63], software for - among others - the simulation of XRD measurements). The NiMnSb-ZnTe-NiMnSb multilayers are simulated assuming the layer stack shown in Fig. 5.6, where variables are layer thicknesses together with corresponding lattice parameters (indicated in red). For the simulation, the lateral lattice constant is assumed to be constant and corresponding to InP (5.8688 Å) - the z-component of the other layers NiMnSb1, ZnTe and NiMnSb2 is then scaled with the ratio of the vertical lattice constant of the individual materials and the lattice constant of the InP substrate to simulate fully strained growth of all layers.
In Fig. 5.7, the same HRXRD scan as in Fig. 5.4 is shown together with the correspond-

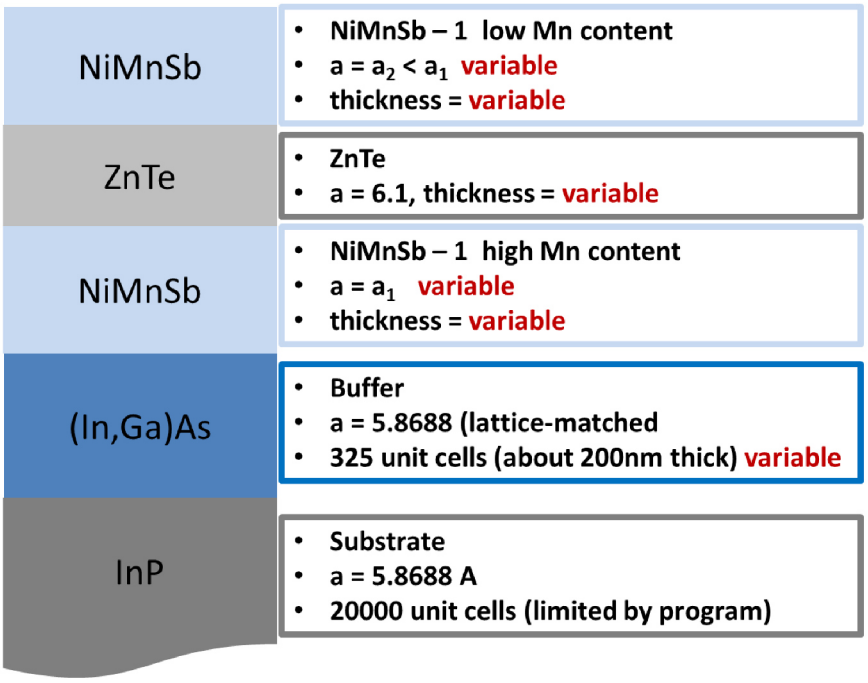

Figure 5.6: layer stacks simulated by DISCUS - variables are printed in red.

ing simulation, using the following parameters: InP (5.8688 Å, 26 µm, thickness limited by maximal number of atoms that can be simulated), (In,Ga)As (5.8688 Å, lattice matched to InP, 200 nm), NiMnSb-1 (6.000 Å, 27.6 nm), ZnTe (6.300 Å, 1.2 nm), NiMnSb-2 (5.925 Å, 12.9 nm). Comparing the simulation and the real measurement, the additional features are well reproduced by the simulation, confirming the nominal layer stack of two NiMnSb layers separated by a thin ZnTe barrier.

5.4 Hysteresis curves of NiMnSb-ZnTe-NiMnSb heterostructures

The magnetic properties are investigated by SQUID: Hysteresis curves are recorded with the external magnetic field in-plane to study the switching behavior of the two NiMnSb layers. It is found that - depending on the sample - these two layers can be either ferromagnetically or antiferromagnetically coupled, as well as without obvious signs of coupling. In the next sections, the physical background of different coupling mechanisms are presented shortly, followed by hysteresis curves recorded at room temperature for several heterostruc-

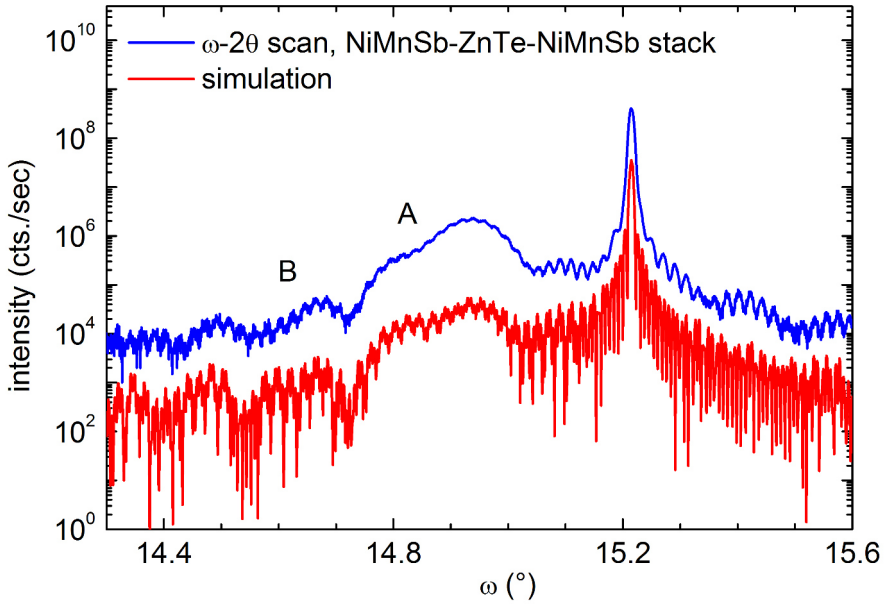

Figure 5.7: HRXRD scan of a NiMnSb-ZnTe-NiMnSb layer stack with simulation.

tures with different coupling and different designs of NiMnSb and barrier thicknesses. The measurements along [1$\bar{1}$0] direction will be shown in red, the complementary measurement along [110] direction is plotted in blue.

5.4.1 Magnetic coupling mechanisms

Two ferromagnetic layers separated by a thin, non-magnetic spacer layer (FM-NM-FM stack) can be coupled to each other, to minimize the total energy of the system. There are several different types of coupling, which will be presented here shortly [64].

a) Bilinear and Biquadratic Coupling
   Bilinear or "interlayer exchange" coupling is caused by interaction of the electron waves in the two ferromagnetic layers and oscillates with the spacer layer thickness. The theory states that in a trilayer FM1/NM/FM2, the electron waves in both magnetic layers FM1 and FM2 are reflected and interference effects occur in the spacer layer. Depending on the form of interference (which is correlated with the thickness of the spacer), the coupling is either ferromagnetic or antiferromagnetic, meaning the parallel or antiparallel alignment of the two ferromagnets is energetically favored.

This model is based on the RKKY coupling theory, that describes in its most basic form the interaction between magnetic impurities and their exchange via the conduction electrons of the host material [65],[66],[67]. It predicts the oscillating behavior of the coupling of two ferromagnetic layers with spacer thickness, however not accurately in magnitude and phase [68]. The theory of bilinear coupling in general is an extension of the RKKY coupling, where the interaction of the ferromagnetic layer (corresponding to the magnetic impurity in the RKKY model) and its surrounding electrons is described as the hybridization of d-levels with s-states of the electrons. For a detailed description, see e.g. reference [68] and references within.
Biquadratic coupling is ascribed to a periodic thickness variation of the spacer layer, meaning ferromagnetic and antiferromagnetic coupling occurs in periodically (lateral) spaced parts of the sample. It is an effective coupling caused by the fluctuation of the magnetizations.

b) Pinhole Coupling
Pinhole coupling is always ferromagnetic, where biquadratic coupling is induced by pinholes (both ferromagntic layers touch).

c) Magnetostatic Coupling - orange peel coupling
On the microscopic scale, the magnetostatic coupling is mostly related to the roughness of the layer, where so called fringing fields occur. When the roughness of the two ferromagnets is correlated, the total energy will be minimized when the two magnetizations are aligned parallel (meaning ferromagnetic coupling). This type of coupling is also called *orange-peel coupling*.

d) Magnetostatic coupling from demagnetization fields
Types a - c of magnetic coupling can occur in samples with a theoretically infinite area. In real devices, the functional layer stack is often limited to a small area on the 100 nm scale. In such dimensions, the two ferromagnetic layers can also be coupled by demagnetization fields that occur at the edge of the sample.

As a summary, there is either ferromagnetic or antiferromagnetic coupling. The latter only occurs for the interlayer exchange coupling, meaning there is weak or no interface roughness. Ferromagnetic coupling can origin from interlayer exchange coupling as well, or from interface roughness. Thus, antiferromagnetic coupling is a promising sign for the interface quality of the barrier layer in a FM-NM-FM stack. In the following, SQUID measurements

of double NiMnSb layers are shown, where both ferromagnetic and antiferromagnetic coupling is found, as well as other forms of coupling mechanism.
Table 5.1 lists all MTJs samples presented in the following, with their nominal layer thicknesses and Mn concentration. Fig. 5.8 shows all hysteresis curves in both [110] and [1$\bar{1}$0] crystal direction with the magnetic field in-plane for anti- and ferromagnetically coupled samples, Fig. 5.12 shows samples with no or other forms of coupling. By evaluating the step height of an event (easy axis switching or hard axis gradual rotation), the corresponding layer can be identified (thicker layers correspond to larger changes in magnetic moment).

sample	nominal thicknesses d_{bot}, d_{top} in nm	nominal barrier thickness d_{ZnTe} (MLs)	Mn concentration in bottom, top layer
H671	30, 5	5	low , high
H746	30, 15	5	high , low
H50	30, 20	7	high , low
H774	30, 15	4	high , low
H775	30, 15	10	high , low
H747	30, 15	10	high , low
H684	30, 15	4	high , low
H692	30, 20	4	high , low
H695	30, 15	10	high , low
H718	30, 15	5	medium , low

Table 5.1: MTJs presented in following sections - different couplings can be observed: antiferromagnetic (H671, H746, H750, H774), ferromagnetic (H775, H747), and other forms of weaker coupling or no obvious coupling (H684, H692, H698, H718).

5.4.2 Antiferromagnetically coupled layers

Antiferromagnetic coupling is the form of coupling that can be seen most clearly in SQUID measurements - it is characterized by three events in the hysteresis curve. Samples H671,

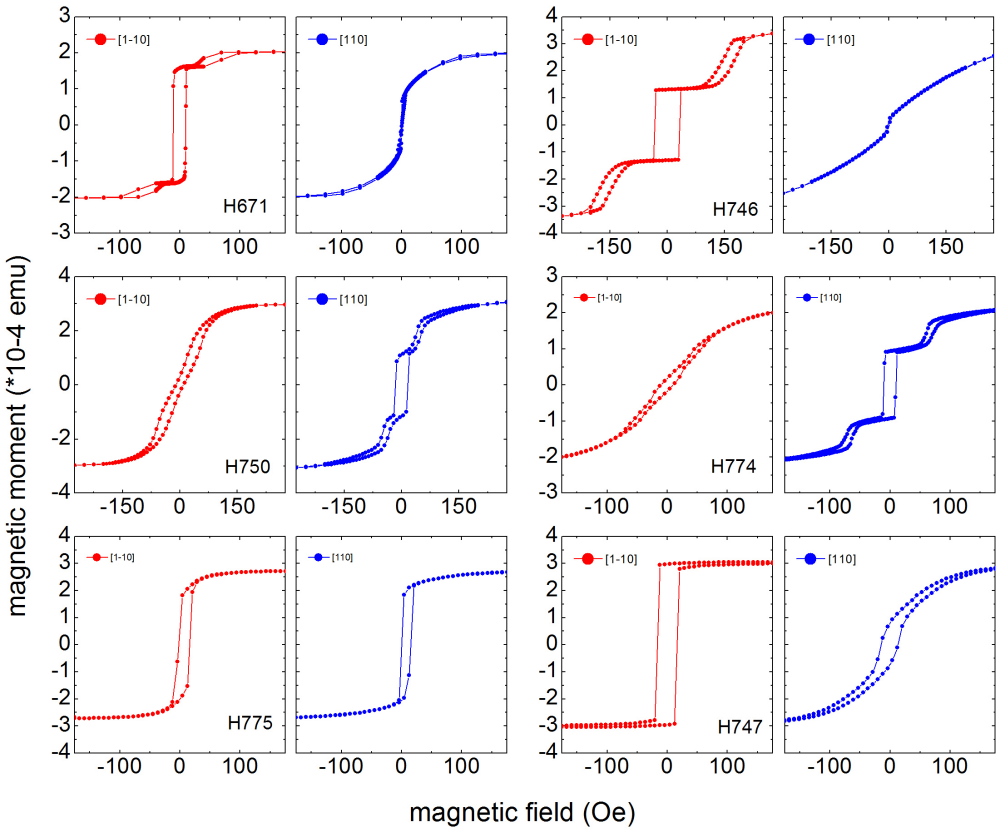

Figure 5.8: SQUID hysteresis curves of MTJs based on NiMnSb with ferro- and antiferromagnetic coupling.

H746, H750 and H774 are four representative samples that exhibit this form of coupling where the hysteresis curves can be explained by the following (Fig. 5.9 shows this behavior exemplary together with the hysteresis curve along $[1\bar{1}0]$ for sample H746): At high positive or negative fields, the sample is saturated and both layers are magnetized in parallel - the magnetization measured corresponds to the saturation magnetization of both layers combined. When going to smaller fields, one NiMnSb layer starts rotating, meaning it behaves like a hard axis. Now, additionally to the decreasing external field, the force to align both magnetizations anti-parallel acts. Thus, the hard axis layer has already rotated its magnetization completely, when the external field is zero and below. At some negative magnetic field, the second NiMnSb layer switches as one, like an easy axis and is characterized by the sharp steep switching event. Due to the antiferromagnetic coupling, the first layer will switch together with the second layer to preserve the anti-parallel configuration. When going to higher negative magnetic fields, the first layer slowly rotates again until the sample is saturated with a parallel configuration. This behavior can also be observed for the same crystal direction in sample H671, and in [110] direction for samples H750 and H774. The plateau that occurs for the case where one layer (here the thinner top layer) has already rotated and the other (thicker bottom layer) is still in its easy axis direction is different for these samples - this is caused by different coercive fields: In case of H746, the coercive field of the layer with easy axis is quite large, the sharp switching event occurs at about 40 Oe. In case of H671, H750 and H774, the coercive field is in the range of 10 Oe. Due to the antiferromagnetic coupling, the hard axis rotates completely even before the external magnetic field has crossed zero. Antiferromagnetic coupling can only be caused by interlayer exchange coupling, when the overlapping of the two electronwaves of FM1 and FM2 are thus that an antiparallel configuration is energetically favored. This is an indication for smooth interfaces between the FM layers and the spacer layer (favoring reflection and interference), since coupling effects caused by a rough interface are always ferromagnetic.

5.4.3 Ferromagnetically coupled layers

In contrast to the antiferromagnetic coupling, ferromagnetic coupling favors the parallel alignment of the two magnetizations. It can be either a result of interlayer exchange coupling, where the thickness of the spacer layer is thus that the interference of the electronwaves is different compared the case of antiferromagnetic coupling. Another reason can

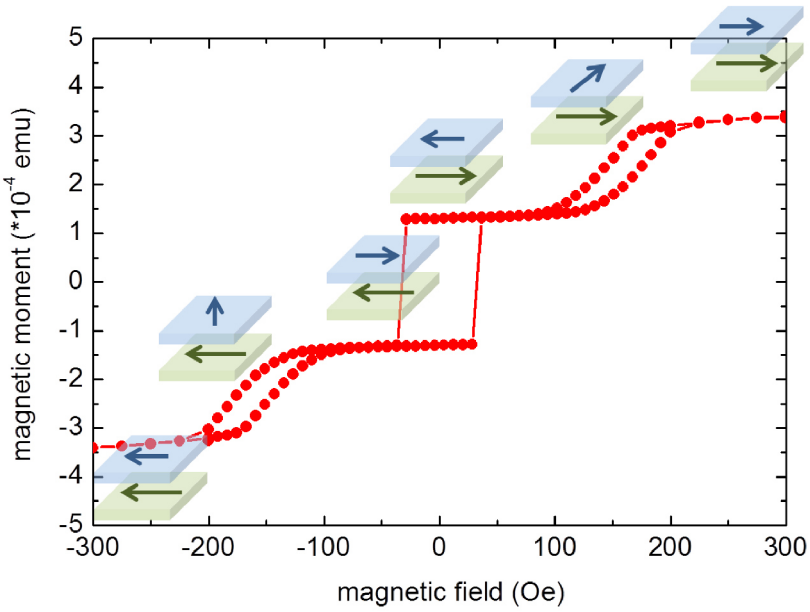

Figure 5.9: Schematics of the magnetic configurations in hysteresis curve of two antiferromagnetically coupled layers.

be interface roughness, where fringing fields at positions where the spacer layer is thinner cause a parallel alignment of the two magnetizations. In the hysteresis curve, only one switching event is observed - see samples H775 and H747 in Fig. 5.8. In case of H775 and crystal direction $[1\bar{1}0]$, it is not clear if there is purely ferromagnetic coupling present since the magnetization exhibits a curvature before there is one large switching event. Sample H747, same crystal direction, however exhibits a nearly flat magnetic moment corresponding to the sum of both magnetizations FM1 and FM2 and one single sharp switching, see also Fig. 5.10. Several NiMnSb-ZnTe-NiMnSb heterostructures turned out to be ferromagnetically coupled, however at first no obvious parameter was found that caused this type of coupling. Then, samples H775 and H774, grown nominally equal in terms of magnetic properties, have a nominally different barrier thickness and the coupling turned out to be ferromagnetic in one case (H775, 10 ML ZnTe, pure ferromagnetic coupling debatable) and antiferromagnetic in the other case (H774, 4 ML ZnTe). This could be a sign of interlayer exchange coupling, changing with barrier thickness - however, a thicker barrier layer here also means a rougher surface of the ZnTe and thus rougher interface towards the top NiMnSb layer, which can cause some sort of orange peel coupling. A reason against

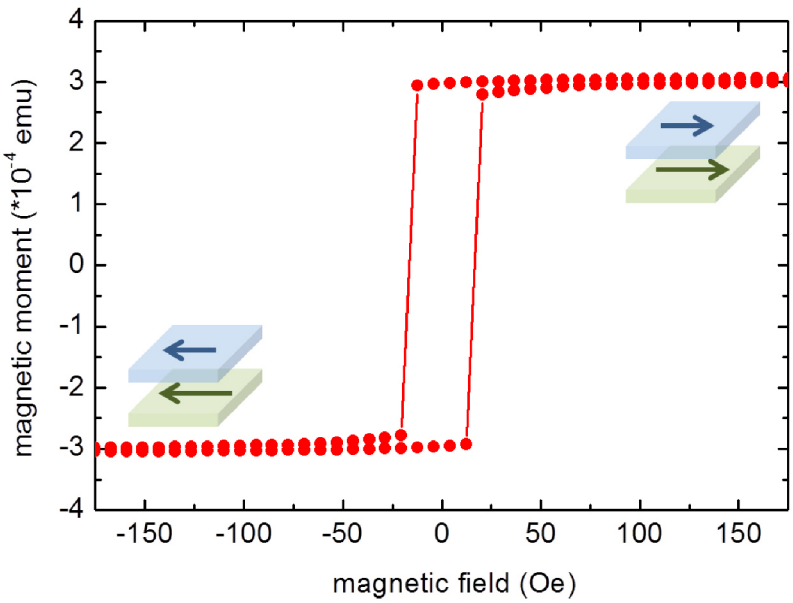

Figure 5.10: Schematics of the magnetic configuration in hysteresis curves of two ferromagnetically coupled layers.

this explanation is that in this picture of rougher ZnTe surface, only the upper interface exhibits this roughness, where for orange peel coupling, the roughness has to be correlated in both interfaces. See also schematics in Fig. 5.11. To explore this further, more series of magnetically equal but in terms of barrier thickness different MTJs should be grown. So far, almost all samples are grown under different conditions, making comparison difficult - however, the optimum growth parameters haven't been found yet. As soon as there is a reliably process for the ZnTe layer, samples with variations of Mn concentration and barrier thicknesses will be easier to compare.

5.4.4 Other coupling / no coupling

Samples H684, H692 and H718 in Fig. 5.12 represent samples that exhibit two distinct switching events. At a first glance, they can be assigned to the two individual NiMnSb layers: In case of H684 in $[1\bar{1}0]$ crystal direction, the sharp switching event results from an easy axis behavior of the thicker bottom NiMnSb layer, and the more gradual rota-

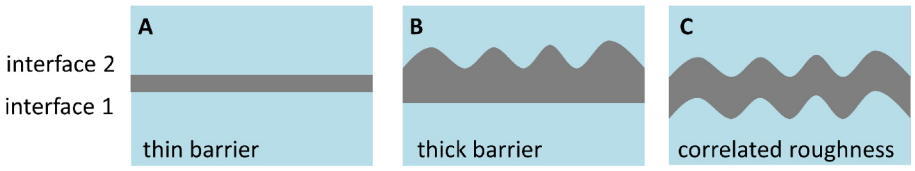

Figure 5.11: Considerations of different barrier thickness and corresponding interface roughness. For orange peel coupling, the roughness of the two interfaces NiMnSb1-ZnTe and ZnTe-NiMnSb2 would have to be correlated as in panel c.

tion with smaller magnetic step height comes from a more hard axis like behavior of the thinner top NiMnSb layer. Here it must be noted that the hard axis rotation of the top layer starts only when the magnetic field already passed zero and is negative - for a layer with a true hard axis and no coupling to other layers, the rotation would start already at positive fields. One explanation could be that the magnetic field from the thick bottom layer acts against the external field and thus the effective magnetic field seen by the top layer is smaller than the nominal external magnetic field. This would result in a shift of the hysteresis curve towards negative/positive fields, depending on the direction of the magnetization of the bottom layer. In the other crystal direction [110], the hysteresis curve shows complementary behavior - the thick NiMnSb layer exhibits a hard axis behavior where the magnetization rotates gradually between 50 and -50 Oe, whereas at about 12 Oe, a steeper switching event occurs that can be assigned to a more easy axis like behavior of the thinner NiMnSb layer.
Sample H692 shows a similar behavior - two main events are observed, however the ratio of the step heights is different due to a thicker top NiMnSb layer as compared to H684 (nominally 20 nm instead of 15 nm). The switching of the thicker layer is not as sharp as in H684, an indication of multidomain switching. In the opposite crystal direction, the behavior is not as distinct and resembles a combination of a hard axis behavior together with a multidomain switching of a more easy axis like layer.
Sample H698 is grown with two NiMnSb layers with identical Mn concentration - nonetheless in $[1\bar{1}0]$ crystal direction, there is a major hard axis behavior superimposed with a sharper switching event, meaning that the two layers exhibit different anisotropies. An explanation is the additional strain that the top NiMnSb layer is exposed to by the large lattice mismatch between ZnTe and itself. This is a further indication that strain is one main mechanism that influences the magnetic anisotropy in these layers. In the comple-

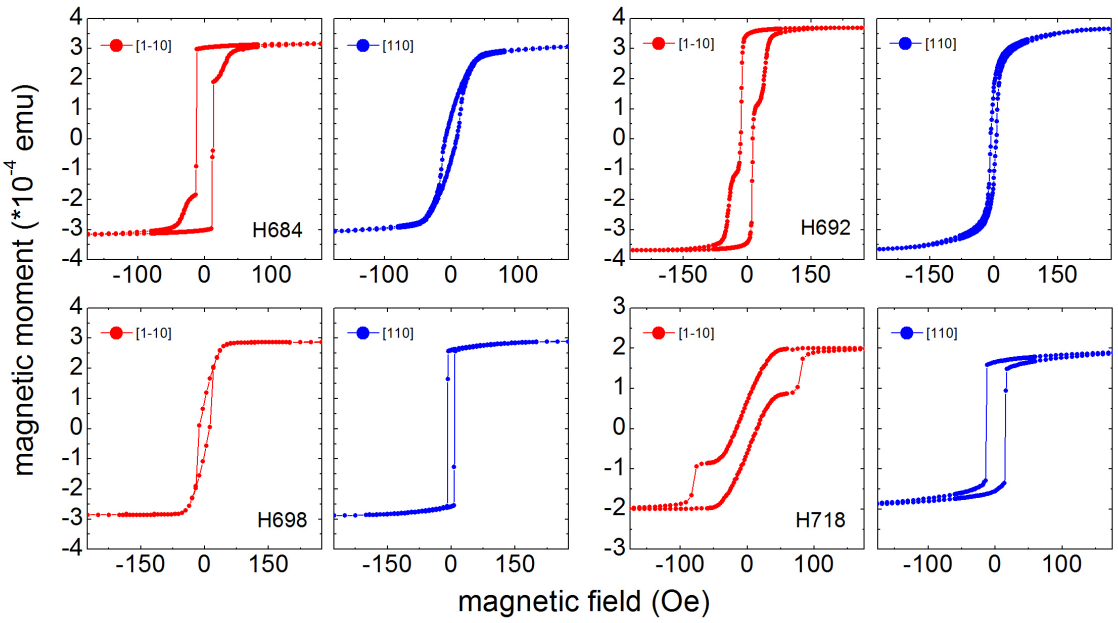

Figure 5.12: SQUID hysteresis curves of MTJs based on NiMnSb with other forms or no coupling.

mentary crystal direction, the hysteresis curve exhibits only one major switching event - this is curious since it means that either both layers exhibit an easy axis in this direction or that ferromagnetic coupling is present. Reason against the first explanation is that one of the layers would have to exhibit an easy axis in both crystal directions - fourfold anisotropies are possible in NiMnSb, but the easy axes appear in the [100] and [010] crystal directions, meaning 45° rotated. Here, the magnetization exhibits also a slight curvature before the main switching event. A complete explanation of this hysteresis curve remains to be found.

Sample H718 is an example for an MTJ with opposite magnetic configuration as sample H684 - the bottom NiMnSb layer has been grown with medium Mn (but rotated RHEED), the top layer with very low Mn concentration. The result is a hard axis behavior for the thick bottom layer in $[1\bar{1}0]$ direction, with a distinct sharp easy axis like switching event for the thin top layer. In the other crystal direction, the main switching can be addressed to the thick bottom layer, exhibiting an easy axis in this direction, where the curvature before and after this switch can be assigned to the thin top layer, now gradually rotating like a

hard axis. This sample is presented here to show that the magnetic anisotropies of the two layers can be controlled in some extend even in a heterostructure, thus a variety of options for the design of devices are possible. It must be noted however that such growth is not yet fully reproducibly, and especially the behavior of the anisotropy of the top NiMnSb layer with ZnTe as its substrate has to be investigated in more detail. It is interesting to see that in case of H684 the top layer (grown with medium/lower Mn concentration) exhibits a hard axis like behavior whereas in H718 (grown under similar conditions), the top layer clearly behaves like an easy axis. The additional strain and interaction with the ZnTe barrier layer and its influence on the magnetic anisotropy is yet to be understood. RHEED observations show a d/2 reconstruction in both crystal directions for most NiMnSb top layers, which is already a hint on a change in crystal structure and thus also magnetic properties.
Moreover it is found that - at least in samples H684 and H718 - the magnetization of the thick bottom layer does not behave as a macrospin, meaning switching as a single domain, but rather switches in several steps. Minor loops are measured with the magnetic field

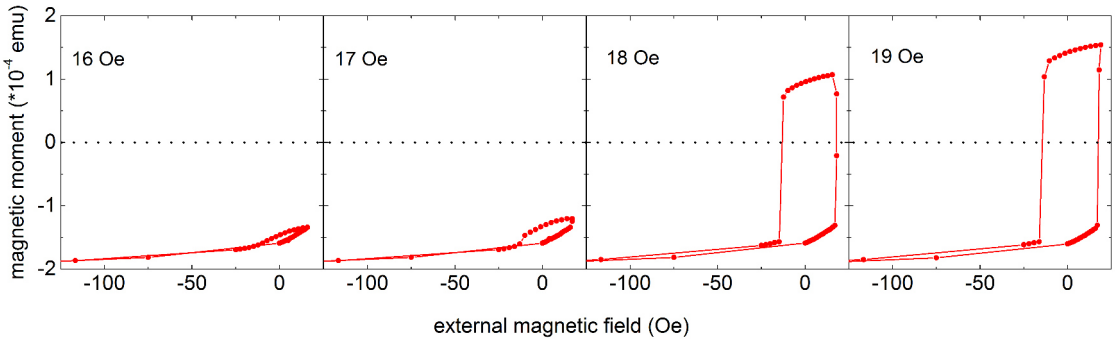

Figure 5.13: Minor loops of sample H718 - when the magnetic field is reversed at 18 Oe the magnetization stays at an intermediate state.

sweeping slowly towards the switching field and then being reversed, which is repeated for several fields in the close range of the switching field. Here (sample H718, see Fig. 5.13), when the magnetic field is reversed at 18 Oe, the magnetization stays at an intermediate state that does not correspond to the total magnetization of the bottom layer. Such behavior is excluded for single layers, compare Fig. 5.14 - here, the magnetization cannot be fixed at an intermediate state when reversing the magnetic field at values in the close range of the switching event. At 2.8 Oe, the magnetization switches as one macrospin from the negative to the corresponding positive value 4.4×10^{-4} emu. *(These hysteresis curves are*

shifted on the x-axis by a field of about 0.25 Oe *- such offsets of the external magnetic field can occur when previous measurements with high magnetic fields have been conducted. It does not change the qualitative result of this measurement.)*
Since the bottom NiMnSb layer is grown under same conditions as single layers, a decreased crystalline quality and resulting split up into domains is not likely. Whereas an inhomogeneous barrier thickness is very likely (together with a top NiMnSb layer exhibiting domains due to unfavorable growth conditions and resulting decreased crystal quality), that could result in areas of different coupling on a macroscopic scale (not comparable to orange peel coupling): parts of the magnetization of the top layer can still be coupled to the bottom layer when other parts already switched (see also Fig. 5.16). The following quantitative evaluation of hysteresis curves further supports this assumption.

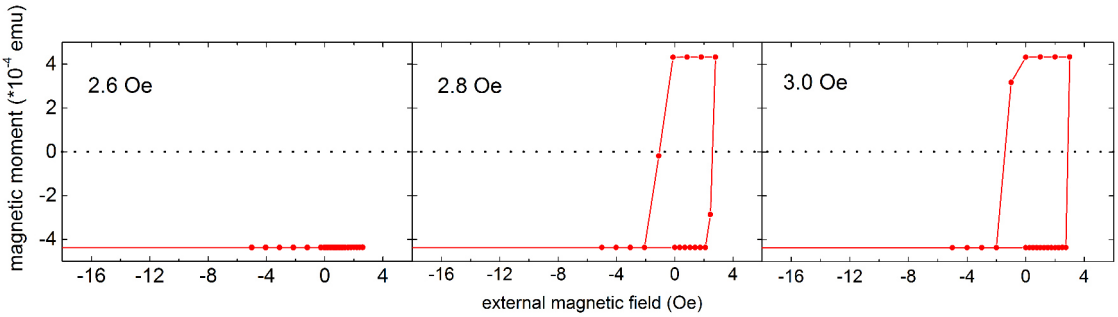

Figure 5.14: Minor loops of a single NiMnSb layer - within 0.2 Oe, the magnetization switches as a macrospin.

5.4.5 Quantitative evaluation of hysteresis curves

The magnetic moment measured in hysteresis curves corresponds directly to the magnetic volume of the samples. Since the area is the same for both NiMnSb layers in one sample, the change in magnetic moment can be related to a so-called effective magnetic thickness. The saturation magnetization of such a heterostructure thus corresponds (theoretically) to the magnetic moment of both layers combined.
Fig. 5.15 shows the hysteresis curves of the two samples presented as examples in the following analysis: E.g. in sample H684 (see also Fig. 5.12), the magnetic moment at saturation of the used sample piece is 3.1×10^{-4} emu. Together with the combined thicknesses

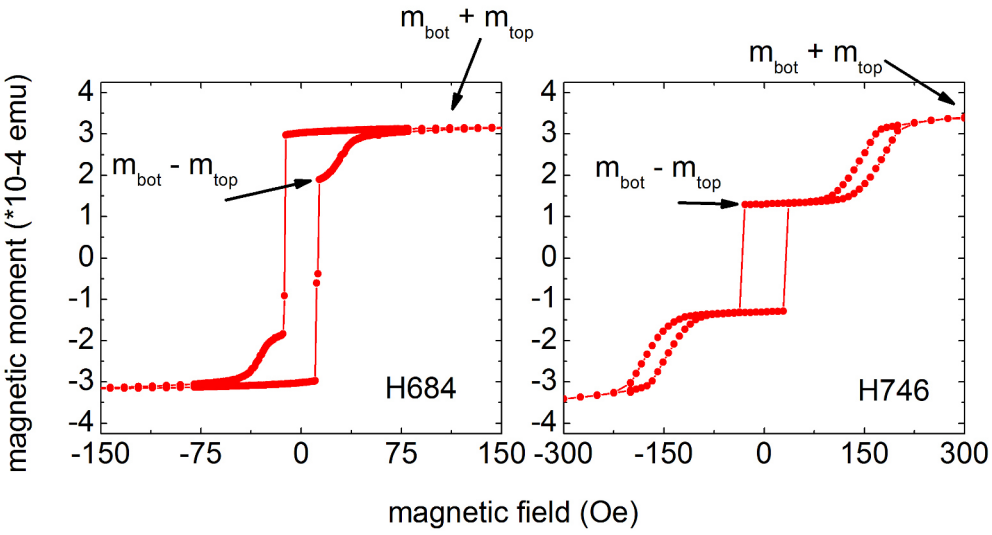

Figure 5.15: Magnetic moments of hysteresis curves used for quantitative analysis of the effective magnetic thicknesses.

of 27.6 nm and 12.9 nm (best fit for HRXRD simulation, see section 5.3), the saturation magnetization per unit formula is 4.1 μ_{Bohr}. This agrees well with the theoretically expected value and shows that NiMnSb with a total thickness of 40.5 nm (addition of 27.6 nm + 12.9 nm for bottom and top NiMnSb layer) is present in the sample. However, when evaluating the single events, the result is the following: The magnetic moment at 13.5 Oe corresponds to the state where the thick bottom layer has switched, the thin top layer however has not rotated yet, meaning $m_{bot} - m_{top}$ with $m_{bot,top}$ corresponding to the magnetic moment of the bottom/top layer. Here, it is $m_{bot} - m_{top} = 1.9 \times 10^{-4}$ emu. At high negative or positive values, the measured magnetic moment corresponds to the addition of both layers $m_{bot} + m_{top} = 3.1 \times 10^{-4}$ emu. From this, the single magnetic moments can be calculated to be $m_{bot} = 2.5 \times 10^{-4}$ emu and $m_{top} = 0.6 \times 10^{-4}$ emu. The ratio m_{top}/m_{bot} is then 0.24 and should correspond to the ratio of the layer thicknesses. However, using the values of the HRXRD simulation, the ratio of the thicknesses is 0.47, and the ratio of the nominal thicknesses (30 nm and 15 nm) is 0.50. This analysis shows that the events in the hysteresis curve do not correspond to the switching or rotation of either the total thick or thin NiMnSb layer and that coupling of some sort must be involved or multi domain switching is present (as it has been shown in the previous section, where minor loops suggest multi domain behavior).

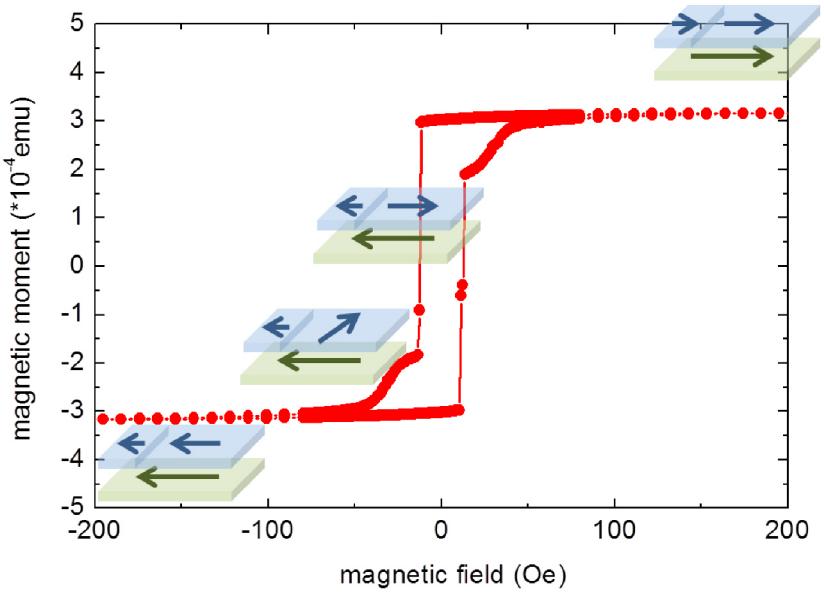

Figure 5.16: Cartoon picture of sample H684, where the top layer is split up into domains and a small fraction is coupled to the bottom layer.

A similar analysis can also be done for antiferromagnetically coupled samples, e.g. sample H746 (see also Fig. 5.9) with nominal thicknesses of 15 nm and 30 nm and ratio of 0.50. The total magnetic moment in saturation (using 45 nm as total thickness of NiMnSb in this sample) is 3.9 μ_{Bohr}. Furthermore it is: $m_{bot} + m_{top} = 3.4 \times 10^{-4}$ emu (magnetic moment at saturation at 300 Oe) and $m_{bot} - m_{top} = 1.3 \times 10^{-4}$ emu (magnetic moment in the range of 60 Oe to -30 Oe), see Fig. 5.15. Thus, the resulting magnetic moments of the two layers are $m_{bot} = 2.4 \times 10^{-4}$ emu and $m_{top} = 1.1 \times 10^{-4}$ emu. Their ratio of $m_{top}/m_{bot} = 0.46$ is close to the ratio expected from nominal layer thicknesses.
This shows that in samples such as H684, no obvious coupling can be seen from the hysteresis curve and only the quantitative analysis suggests that there must be some form of coupling involved or the individual layers are split up into domains. Fig. 5.16 shows the hysteresis curve of sample H684 with cartoon pictures of the two magnetizations and the split up of the top NiMnSb layer into domains. A small fraction of the top layer could e.g. be coupled ferromagnetically to the bottom layer (making the magnetic step height of the switching event larger), which then results in the difference between the nominal thickness ratio and the ratio of effective magnetic thicknesses.

In samples such as H746, this evaluation of the effective magnetic thicknesses shows that the individual events in the hysteresis curve actually stem from switching or rotation of the total magnetic moment of the individual layers. This analysis comes with estimated errors of about 5 % from the reading of the magnetic moment, which is here rounded to one decimal place. Additionally, the difference of Mn concentration in the two layers results in different saturation magnetizations of the two individual layers and thus the magnetic moment readings should be scaled accordingly. However this is not possible since the actual saturation magnetization of the individual layers cannot be determined separately. Compared to the error of the readings, this error should be negligible and cannot explain the difference between the ratio of nominal thicknesses (in case of H684: 0.47) and the ratio of effective magnetic thicknesses (0.24).

5.5 Summary

The epitaxial growth process for NiMnSb-ZnTe-NiMnSb heterostructures has been presented. For the ultrathin ZnTe barrier layer, a special MBE technique - atomic layer epitaxy (ALE) - is used and optimized. The two NiMnSb layers in such heterostructures have been grown with different Mn concentration to explore different magnetic configurations. HRXRD measurements and their simulation suggest that the nominal layer stack with two spatially separated NiMnSb layer is present. Hysteresis curves measured by SQUID have been used to determine the magnetic behavior, where different coupling mechanisms of the two NiMnSb layers have been observed for different samples. The growth process is not reproducible yet in a way that the resulting layer stacks exhibit reproducible magnetic behavior - especially the magnetic anisotropy of the top NiMnSb layer on ZnTe remains to be understood and controlled. Nonetheless, separate switching of two mutual orthogonal magnetic anisotropies has been observed which are positive preliminary results towards application in spin torque devices.

Chapter 6

Conclusion and Outlook

In this thesis, an in-depth study on the Half-Heusler alloy NiMnSb is presented, where structural and magnetic properties of MBE grown single layers as well as NiMnSb-ZnTe-NiMnSb heterostructures are investigated.
A method to control both the strength and orientation of the uniaxial magnetic anisotropy in NiMnSb has been found: With a change of Mn concentration, the uniaxial easy axis can be rotated by 90° from the [110] to the [1$\bar{1}$0] crystal direction. The strength of the anisotropy can be tuned up to the $1 \times 10^5\,\mathrm{J\,m^{-3}}$ range which is comparable to the anisotropy in Fe. Most importantly is that the magnetic damping is still very low in the lower 1×10^{-3} range, even for far-off-stoichiometric samples. The fundamental origin of this behavior remains to be identified - the results suggest that several different anisotropy terms - magnetocrystalline, strain-induced and interface anisotropy - are combined.
From a technological point of view, this controllable magnetic anisotropy in addition to its very small Gilbert damping even for off-stoichiometric samples and high spin polarization make NiMnSb an even more attractive and interesting material for application in spin torque devices. It has been shown in other material systems that STOs based on two layers with mutually orthogonal magnetizations improve output power due to the increased spin transfer torque, thus the control of the magnetic anisotropy is highly valuable. As a direct application of this new control, double layers of NiMnSb with a thin ZnTe barrier layer are grown and characterized magnetically as well as structurally. It is found that these double layers can exhibit different magnetic coupling, both ferromagnetic and antiferromagnetic coupling as well as other forms are observed.
In regard of application of such double layers as a basis for STOs, there are several factors

that have impact on the functionality: First of all, the two magnetizations should exhibit a significant difference in coercive field - thus, one magnetization can act as a fixed layer whereas the second magnetization precesses as the free layer. Sample H746 is an example for such a system: the large plateau of stable magnetic moment where the top layer has rotated completely and the bottom layer has not switched yet means that the two magnetizations are in a stable configuration for a large range of external magnetic fields. Another important parameter is the threshold current that corresponds to the current density required to start a spin torque induced oscillation. This current density is lower for materials with small damping factors (as it is the case here) since this damping counteracts the current induced spin torque. It has been shown that the damping does not suffer from changing the composition of the layer, even within the explored range of maximum and minimum Mn concentration.

Further investigation on the magnetic anisotropy and the influence of a Pt cap layer should be done. Such a study could contain a thickness dependent series of samples, with stoichiometric composition and a nominally non-rotated anisotropy.

One other main task that remains is to grow reproducibly double NiMnSb layers with nominal equal coupling and equal magnetic configuration. Here, especially the anisotropy of the top NiMnSb layer has to be controlled better. The next focus should be on the insulating properties of the ZnTe barrier layers - here, the thickness as the most straight forward parameter can be explored. But also growth parameters like temperatures and time constants might help. Besides that, actual devices for transport measurements have to be built, in order to test electric properties of the MTJs, with the long term goal of the fabrication of spin torque oscillators.

Appendix

Resistivities

Here, a list of resistivities for the individual layers involved in the here presented hetereostructures is given. These values allow for an estimation of device resistance as a reference for transport measurements and for device design.

layer	resistivity ($\Omega\,$cm)
InP:S	1×10^{-3} - 5×10^{-4}
InP:Fe	5×10^{7}
(In,Ga)As	$0.5 - 0.6$ [69]
NiMnSb	2×10^{-5}

Table 1: resistivity of the individual layers

The values for the substrate layers, InP:S and InP:Fe are given specifications of the manufacturer AXT. The drawback of the Fe-doped substrate is a slightly worse crystal quality compared to S-doped InP, nonetheless it is a very useful substrate especially for transport devices. The resistivity for (In,Ga)As is calculated by a report on mobility of undoped (In,Ga)As on InP - see reference [69]. It should be noted that the value for the (In,Ga)As buffers here might be smaller due to not perfectly optimized growth in relation to transport properties.

List of own publications

- F. Gerhard, C. Schumacher, C. Gould, L. W. Molenkamp *Control of the magnetic in-plane anisotropy in off-stoichiometric NiMnSb*, Journal of Applied Physics 115, 094505 (2014) (2014)

- M. Samiepour, F. Gerhard, T. Borzenko, C. Gould, and L.W. Molenkamp *Sophisticated process for a spin torque device fabricated from a pillar containing two different ferromagnetic materials separated by a non-magnetic layer.* Microelectronic Engineering, 119(0):20-23, 2014

- P. Dürrenfeld, F. Gerhard, M. Ranjbar, C. Gould, L. W. Molenkamp, J. Åkerman *Spin Hall Effect-controlled magnetization dynamics in NiMnSb* Journal of Applied Physics 117, 17E103 (2015)

- P. Dürrenfeld, S. M. Mohseni, F. Gerhard, M. Ranjbar, F. Qejvanaj, S. R. Sani, S. Chung, C. Gould, L.W. Molenkamp, and J. Åkerman, *Low-Current, Narrow-Linewidth Microwave Signal Generation in Single-Layer-NiMnSb Based Nano-Contact Spin Torque Oscillators*, in preparation for APL

- F. Gerhard, T. Naydenova, C. Schumacher, C. Gould, L. W. Molenkamp
  Growth and characterization of epitaxial NiMnSb-ZnTe-NiMnSb heterostructures, in preparation for Journal of Crystal Growth

Bibliography

[1] Deutsche Physikalische Gesellschaft (1899-1945). *Verhandlungen der deutschen physikalischen Gesellschaft*. Number Bd. 5. Friedr. Vieweg & Sohn, 1903.

[2] R. A. de Groot, F. M. Mueller, P. G. van Engen, and K. H. J. Buschow. New Class of Materials: Half-Metallic Ferromagnets. *Phys. Rev. Lett.*, 50:2024–2027, Jun 1983.

[3] K. E. H. M. Hanssen, P. E. Mijnarends, L. P. L. M. Rabou, and K. H. J. Buschow. Positron-annihilation study of the half-metallic ferromagnet NiMnSb: Experiment. *Phys. Rev. B*, 42:1533–1540, Jul 1990.

[4] C. Hordequin, D. Ristoiu, L. Ranno, and J. Pierre. On the cross-over from half-metal to normal ferromagnet in NiMnSb. *The European Physical Journal B - Condensed Matter and Complex Systems*, 16(2):287–293, 2000.

[5] W. Zhu, B. Sinkovic, E. Vescovo, C. Tanaka, and J. S. Moodera. Spin-resolved density of states at the surface of NiMnSb. *Phys. Rev. B*, 64:060403, Jul 2001.

[6] S. K. Clowes, Y. Miyoshi, Y. Bugoslavsky, W. R. Branford, C. Grigorescu, S. A. Manea, O. Monnereau, and L. F. Cohen. Spin polarization of the transport current at the free surface of bulk NiMnSb. *Phys. Rev. B*, 69:214425, Jun 2004.

[7] Lance Ritchie, Gang Xiao, Y. Ji, T. Y. Chen, C. L. Chien, Ming Zhang, Jinglan Chen, Zhuhong Liu, Guangheng Wu, and X. X. Zhang. Magnetic, structural, and transport properties of the Heusler alloys Co_2MnSi and NiMnSb. *Phys. Rev. B*, 68:104430, Sep 2003.

[8] R. J. Soulen, J. M. Byers, M. S. Osofsky, B. Nadgorny, T. Ambrose, S. F. Cheng, P. R. Broussard, C. T. Tanaka, J. Nowak, J. S. Moodera, A. Barry, and J. M. D.

Coey. Measuring the Spin Polarization of a Metal with a Superconducting Point Contact. *Science*, 282(5386):85–88, 1998.

[9] Mohammad Haidar and Matthieu Bailleul. Thickness dependence of degree of spin polarization of electrical current in permalloy thin films. *Phys. Rev. B*, 88:054417, Aug 2013.

[10] S.J Jenkins and D.A King. Minority metallic surface states of a half-metallic ferrimagnet. *Surface Science*, 494(3):L793 – L798, 2001.

[11] J.A. Caballero, Y.D. Park, A. Cabbibo, and J.R. Childress. Sputter-deposition of NiMnSb magnetic thin films from a composite target onto Si substrates. *Journal of Electronic Materials*, 26(11):1274–1278, 1997.

[12] D Ristoiu, J.P Nozires, and L Ranno. Epitaxial NiMnSb thin films prepared by facing targets sputtering . *Journal of Magnetism and Magnetic Materials*, 219(1):97 – 103, 2000.

[13] P. Turban, S. Andrieu, B. Kierren, E. Snoeck, C. Teodorescu, and A. Traverse. Growth and characterization of single crystalline NiMnSb thin films and epitaxial NiMnSb/MgO/NiMnSb(001) trilayers. *Phys. Rev. B*, 65:134417, Mar 2002.

[14] Turban P., Andrieu S., Snoeck E., Kierren B., and Teodorescu C. NiMnSb/MgO/NiMnSb heterostructures grown by MBE. *Journal of Magnetism and Magnetic Materials*, 240(1):427–429, 2002.

[15] Willem Van Roy and Marek Wjcik. Epitaxial Growth of NiMnSb on GaAs by Molecular Beam Epitaxy. In I. Galanakis and P.H. Dederichs, editors, *Half-metallic Alloys*, volume 676 of *Lecture Notes in Physics*, pages 153–185. Springer Berlin Heidelberg, 2005.

[16] P. J. Brown, A. P. Gandy, R. Kainuma, T. Kanomata, T. Miyamoto, M. Nagasako, K. U. Neumann, A. Sheikh, and K. R. A. Ziebeck. Atomic order and magnetization distribution in the half metallic and nearly half metallic C1b compounds NiMnSb and PdMnSb. *Journal of Physics-condensed Matter*, 22, 2010.

[17] Delia Ristoiu, J. P. Nozires, C. N. Borca, B. Borca, and P. A. Dowben. Manganese surface segregation in NiMnSb. *Applied Physics Letters*, 76(17):2349–2351, 2000.

[18] M.J. Otto, H. Feil, R.A.M. Van Woerden, J. Wijngaard, P.J. Van Der Valk, C.F. Van Bruggen, and C. Haas. Electronic structure and magnetic, electrical and optical properties of ferromagnetic Heusler alloys. *Journal of Magnetism and Magnetic Materials*, 70(13):33 – 38, 1987.

[19] Markus Donath, Georgi Rangelov, Jrgen Braun, and Wolfgang Grentz. Magnetization, Spin Polarization, and Electronic Structure of NiMnSb Surfaces. In Markus Donath and Wolfgang Nolting, editors, *Local-Moment Ferromagnets*, volume 678 of *Lecture Notes in Physics*, pages 261–273. Springer Berlin Heidelberg, 2005.

[20] D. Houssameddine, U. Ebels, B. Delaët, B. Rodmacq, I. Firastrau, F. Ponthenier, M. Brunet, C. Thirion, J.-P. Michel, L. Prejbeanu-Buda, M.-C. Cyrille, O. Redon, and B. Dieny. Spin-torque oscillator using a perpendicular polarizer and a planar free layer. *Nature Materials*, 6:447–453, June 2007.

[21] T. Devolder, A. Meftah, K. Ito, J. A. Katine, P. Crozat, and C. Chappert. Spin transfer oscillators emitting microwave in zero applied magnetic field. *Journal of Applied Physics*, 101(6):063916, March 2007.

[22] S. M. Mohseni, S. R. Sani, J. Persson, T. N. Anh Nguyen, S. Chung, Ye. Pogoryelov, and Johan Åkerman. High frequency operation of a spin-torque oscillator at low field. *physica status solidi (RRL) Rapid Research Letters*, 5(12):432–434, 2011.

[23] Zhongming Zeng, Pedram Khalili Amiri, Ilya N. Krivorotov, Hui Zhao, Giovanni Finocchio, Jian-Ping Wang, Jordan A. Katine, Yiming Huai, Juergen Langer, Kosmas Galatsis, Kang L. Wang, and HongWen Jiang. High-Power Coherent Microwave Emission from Magnetic Tunnel Junction Nano-oscillators with Perpendicular Anisotropy. *ACS Nano*, 6(7):6115–6121, 2012.

[24] A. Riegler. *Ferromagnetic resonance study of the Half-Heusler alloy NiMnSb: The benefit of using NiMnSb as a ferromagnetic layer in pseudo spin-valve based spin-torque oscillators*. PhD thesis, Universität Würzburg, 2011.

[25] Christian Kumpf, Andreas Stahl, Isabella Gierz, Claus Schumacher, Suddhasatta Mahapatra, Florian Lochner, Karl Brunner, Georg Schmidt, Laurens W. Molenkamp, and Eberhard Umbach. Structure and relaxation effects in thin semiconducting films and quantum dots. *physica status solidi (c)*, 4(9):3150–3160, 2007.

[26] W. Braun. *Applied RHEED: Reflection High-energy Electron Diffraction During Crystal Growth*. Applied RHEED: reflection high-energy electron diffraction during crystal growth. Springer, 1999.

[27] P. Bach. *Growth and Characterization ofNiMnSb-based Heterostructures*. PhD thesis, Universität Würzburg, 2006.

[28] F. Lochner. *Epitaxial growth and characterization of NiMnSb llayer for novel spintronic devices*. PhD thesis, Universität Würzburg, 2011.

[29] K. Fujiwara, K. Kanamoto, Y.N. Ohta, Y. Tokuda, and T. Nakayama. Classification and origins of GaAs oval defects grown by molecular beam epitaxy. *Journal of Crystal Growth*, 80(1):104 – 112, 1987.

[30] M. Samiepour. *Fabrication and characterization of CPP-GMR and spin-transfer torque induced magnetic switching*. PhD thesis, Universität Würzburg, 2014.

[31] M. Samiepour, F. Gerhard, T. Borzenko, C. Gould, and L.W. Molenkamp. Sophisticated process for a spin-torque device fabricated from a pillar containing two different ferromagnetic materials separated by a non-magnetic layer. *Microelectronic Engineering*, 119(0):20 – 23, 2014.

[32] Heiko Ress. *Neue Messmethoden in der hochauflösenden Röntgendiffraktometrie*. PhD thesis, University of Wuerzburg, 1998.

[33] A. Zolotaryov, A. Bader, C. Schumacher, P. Bach, L. W. Molenkamp, F. Wu, A. Stahl, C. Kumpf, E. Umbach, and R. L. Johnson. Investigation of stress relaxation in Heusler-alloy thin films: NiMnSb. Technical report, HASYLAB, 2002.

[34] Linus Pauling. The Nature of the Interatomic Forces in Metals. *Phys. Rev.*, 54:899–904, Dec 1938.

[35] J. C. Slater. The Ferromagnetism of Nickel. *Phys. Rev.*, 49:537–545, Apr 1936.

[36] Tanja Graf, Claudia Felser, and Stuart S.P. Parkin. Simple rules for the understanding of Heusler compounds. *Progress in Solid State Chemistry*, 39(1):1 – 50, 2011.

[37] I. Galanakis, P. H. Dederichs, and N. Papanikolaou. Origin and properties of the gap in the half-ferromagnetic Heusler alloys. *Phys. Rev. B*, 66:134428, Oct 2002.

[38] B. Alling, S. Shallcross, and I. A. Abrikosov. Role of stoichiometric and nonstoichiometric defects on the magnetic properties of the half-metallic ferromagnet NiMnSb. *Phys. Rev. B*, 73:064418, Feb 2006.

[39] M. Ekholm, P. Larsson, B. Alling, U. Helmersson, and I. A. Abrikosov. Ab initio calculations and synthesis of the off-stoichiometric half-Heusler phase Ni[1 - x]Mn[1 + x]Sb. *Journal of Applied Physics*, 108(9):093712, 2010.

[40] C.D. Wagner, W.M. Riggs, L.E. Davis, and J.F. Moulder. *Handbook of X-Ray Photoelectron Spectroscopy*. Perkin-Elmer Corporation, Physical Electronics Division, 1978.

[41] M. P. Seah and W. A. Dench. Quantitative electron spectroscopy of surfaces: A standard data base for electron inelastic mean free paths in solids. *Surface and Interface Analysis*, 1(1):2–11, 1979.

[42] A. Koveshnikov, G. Woltersdorf, J. Q. Liu, B. Kardasz, O. Mosendz, B. Heinrich, K. L. Kavanagh, P. Bach, A. S. Bader, C. Schumacher, C. Rüster, C. Gould, G. Schmidt, L. W. Molenkamp, and C. Kumpf. Structural and magnetic properties of NiMnSb/InGaAs/InP(001). *Journal of Applied Physics*, 97(7):073906, 2005.

[43] Bretislav Heinrich and J. Anthony C. Bland, editors. *Ultrathin Magnetic Structures II*. Springer Berlin Heidelberg, 1994.

[44] Charles Kittel. On the Theory of Ferromagnetic Resonance Absorption. *Phys. Rev.*, 73:155–161, Jan 1948.

[45] Kittel, C. Ferromagnetic resonance. *J. Phys. Radium*, 12(3):291–302, 1951.

[46] F. Gerhard, C. Schumacher, C. Gould, and L. W. Molenkamp. Control of the magnetic in-plane anisotropy in off-stoichiometric nimnsb. *Journal of Applied Physics*, 115(9):094505–094505–4, 2014.

[47] C. D. Graham. Magnetocrystalline Anisotropy Constants of Iron at Room Temperature and Below. *Phys. Rev.*, 112:1117–1120, Nov 1958.

[48] F.J.A. den Broeder, W. Hoving, and P.J.H. Bloemen. Magnetic anisotropy of multilayers . *Journal of Magnetism and Magnetic Materials*, 93(0):562 – 570, 1991.

[49] Bretislav Heinrich and J. Anthony C. Bland, editors. *Ultrathin Magnetic Structures I.* Springer Berlin Heidelberg, 1994.

[50] A. Aharoni. *Introduction to the Theory of Ferromagnetism.* Oxford University Press, 2000.

[51] Bernhard Botters, Fabian Giesen, Jan Podbielski, Peter Bach, Georg Schmidt, Laurens W. Molenkamp, and Dirk Grundler. Stress dependence of ferromagnetic resonance and magnetic anisotropy in a thin NiMnSb film on InP(001). *Applied Physics Letters*, 89(24):242505–242505–3, 2006.

[52] J.W. Matthews and A.E. Blakeslee. Defects in epitaxial multilayers: I. Misfit dislocations . *Journal of Crystal Growth*, 27(0):118 – 125, 1974.

[53] O. Thomas, Q. Shen, P. Schieffer, N. Tournerie, and B. Lépine. Interplay between Anisotropic Strain Relaxation and Uniaxial Interface Magnetic Anisotropy in Epitaxial Fe Films on (001) GaAs. *Phys. Rev. Lett.*, 90:017205, Jan 2003.

[54] Y. B. Xu, D. J. Freeland, M. Tselepi, and J. A. C. Bland. Anisotropic lattice relaxation and uniaxial magnetic anisotropy in Fe/InAs(100)-4x2. *Phys. Rev. B*, B62:1167, 2000.

[55] D.C. Ralph and M.D. Stiles. Spin transfer torques . *Journal of Magnetism and Magnetic Materials*, 320(7):1190 – 1216, 2008.

[56] Xingtao Jia, Ying Li, Ke Xia, and Gerrit E. W. Bauer. Angular momentum transfer torques in spin valves with perpendicular magnetization. *Phys. Rev. B*, 84:134403, Oct 2011.

[57] G. Binasch, P. Grünberg, F. Saurenbach, and W. Zinn. Enhanced magnetoresistance in layered magnetic structures with antiferromagnetic interlayer exchange. *Phys. Rev. B*, 39:4828–4830, Mar 1989.

[58] M. N. Baibich, J. M. Broto, A. Fert, F. Nguyen Van Dau, F. Petroff, P. Etienne, G. Creuzet, A. Friederich, and J. Chazelas. Giant Magnetoresistance of (001)Fe/(001)Cr Magnetic Superlattices. *Phys. Rev. Lett.*, 61:2472–2475, Nov 1988.

[59] M. Julliere. Tunneling between ferromagnetic films. *Physics Letters A*, 54(3):225 – 226, 1975.

[60] W. H. Butler, X.-G. Zhang, T. C. Schulthess, and J. M. MacLaren. Spin-dependent tunneling conductance of Fe|MgO|Fe sandwiches. *Phys. Rev. B*, 63:054416, Jan 2001.

[61] Stuart S. P. Parkin, Christian Kaiser, Alex Panchula, Philip M. Rice, Brian Hughes, Mahesh Samant, and See-Hun Yang. Giant tunnelling magnetoresistance at room temperature with MgO (100) tunnel barriers. *nature materials*, 3:862–867, 2004.

[62] J. Liu, E. Girgis, P. Bach, C. Rüster, C. Gould, G. Schmidt, and L. W. Molenkamp. Tunneling magnetoresistance in devices based on epitaxial NiMnSb with uniaxial anisotropy. *Journal of Applied Physics*, 99(3):036110–036110–3, 2006.

[63] Th. Proffen and R. B. Neder. *DISCUS*, a program for diffuse scattering and defect structure simulations – update. *Journal of Applied Crystallography*, 32(4):838–839, Aug 1999.

[64] Bretislav Heinrich and J. Anthony C. Bland, editors. *Ultrathin Magnetic Structures III*. Springer Berlin Heidelberg, 1994.

[65] M. A. Ruderman and C. Kittel. Indirect Exchange Coupling of Nuclear Magnetic Moments by Conduction Electrons. *Phys. Rev.*, 96:99–102, Oct 1954.

[66] Tadao Kasuya. A Theory of Metallic Ferro- and Antiferromagnetism on Zener's Model. *Progress of Theoretical Physics*, 16(1):45–57, 1956.

[67] Kei Yosida. Magnetic Properties of Cu-Mn Alloys. *Phys. Rev.*, 106:893–898, Jun 1957.

[68] P. Bruno and C. Chappert. Interlayer Exchange Coupling: RKKY Theory and Beyond. In RobinF.C. Farrow, Bernard Dieny, Markus Donath, Albert Fert, and B.D. Hermsmeier, editors, *Magnetism and Structure in Systems of Reduced Dimension*, volume 309 of *NATO ASI Series*, pages 389–399. Springer US, 1993.

[69] K. Somogyi and J. Pfeifer. Electron mobility measured in undoped InGaAs epitaxial layer grown on n-InP substrate. *Applied Physics Letters*, 61(18):2220–2221, Nov 1992.

Danksagung

Als erstes gilt mein Dank Professor Dr. Laurens W. Molenkamp, der es mir ermöglicht hat, diese Dissertation am Lehrstuhl EP3 durchzuführen, sowie für die Hilfe und Diskussionen im Heusler Projekt.

Außerdem möchte ich mich auch besonders bei PD. Dr. Charles Gould für die tagtägliche Betreuung des Projekts und für die immer hilfreichen Ratschläge und Diskussionen bedanken.

Many thanks go to Professor Dr. Johan Åkerman and his groups at NanOsc AB, KTH Stockholm and the University of Gothenburg for a great and fruitful cooperation.

Vielen Dank an Claus Schumacher für ein offenes Ohr für alle fachlichen und nicht fachlichen Anliegen sowie für die immer ergebnisreichen Diskussionen und Besprechungen, die einem immer genau zeigen, wo es noch hakt.

Danke auch an alle anderen Mitglieder der MBE Kaffeerunde - Christopher Ames, Lars Ebel, Alexander Frey, Maximilian Kessel, Philipp Leubner, Rebekka Pfeuffer, Christoph Pohl, Raimund Schlereth, Steffen Schreyeck, Mirko Trabel und Martin Winnerlein inklusive Diplomanden, Masteranden und Bachelors - für die gute Zusammenarbeit, Austausch und Unterstützung. Vielen Dank auch an Prof. Dr. Grzegorz Karczweski für die hilfreichen Diskussionen!

Ein herzliches Dankeschön geht auch an Petra Wolf-Müller, Jana Hinterberger und Carmen Bundschuh für das Vorbereiten der Proben, Martin Zipf und Volkmar Hock für das am Laufen halten der MBE und das zur Seite stehen bei kleinen und größeren technischen Katastrophen, Kammeröffnungen und sonstigen Problemen, sowie für die Hilfe bei den XPS Messungen.

Danke an die anderen Mitglieder der Heuslergruppe - dabei vor allem vielen Dank an Martin Baussenwein für viele ergebnisreiche Diskussionen und Anregungen sowie eine gute Schreibtischnachbarschaft und nicht zuletzt herzlichen Dank an Tatjana Borzenko für die Unterstützung bei der Lithographie in unserem Projekt. Danke auch an Tsvetelina Nay-

denova für die Hilfe bei den SQUID Messungen!

An Tsveti und Rebekka - Danke für eure Freundschaft, den Beistand und die zahlreichen Spaziergänge um die Uni, bei denen man wieder einen klaren Kopf bekommen konnte!

An meine ehemalige Quantentransport-Gruppe: Danke für die erheiternden Tischgespräche in der Mensa, die andauernde Hilfsbereitschaft im Labor und gute Büronachbarschaft.

Danke auch an alle anderen EP3ler für die Unterstützung und gute Zusammenarbeit im Labor und an Angelika Berger bei verwaltungstechnischen Dingen, und an Roland Ebert und Cornelius Ziga für die Versorgung mit flüssigem Helium.

Dankeschön an meine Freunde, die mit Physik so gar nichts am Hut haben, trotzdem über die Jahre nicht die Geduld mit mir verloren und mich auch mal auf andere Gedanken gebracht haben.

Vor allem möchte mich auch bei meiner Familie bedanken, die mich während des Studiums und der Promotion unterstützt hat! Danke auch an Familie Brüne!

Christoph - Danke, dass Du da bist!